*Astronomy Letters, Vol. 28, No. 3, 2002, pp. 139–142. Translated from Pis'ma v Astronomicheskiĭ Zhurnal, Vol. 28, No. 3, 2002, pp. 163–166.*


# Parameters of the Early Universe and Primordial Black Holes

**S. O. Alexeyev, M. V. Sazhin, and O. S. Khovanskaya***

*Sternberg Astronomical Institute, Universitetskii pr. 13, Moscow, 119899 Russia*

Received October 17, 2001

**Abstract**—We consider the possibility of low-mass primordial black holes being formed in terms of the inflationary theory of the early Universe. We found a condition on the reheating temperature under which the relic remnants of primordial black holes had been formed by now. These relic remnants may account for a part of the dark matter in our Universe. © *2002 MAIK "Nauka/Interperiodica"*.

Key words: *early Universe, primordial black holes*

## INTRODUCTION

At the early evolutionary stages of the Universe, primordial black holes (PBHs) of macroscopic size could be formed through large-scale fluctuations. Such objects were considered by Novikov *et al.* (1979), Dolgov *et al.* (2000), Rubin *et al.* (2000), and Barrau (2000). Because of the Hawking effect, a black hole (BH) is capable of emitting particles and evaporating. The smaller the BH mass, the more intense the emission:

$$-\frac{dM}{dt} \approx 4 \times 10^{-5} \left(\frac{m_{Pl}}{M}\right)^2 \frac{m_{Pl}}{t_{Pl}} f, \qquad (1)$$

where $f = 1.023h(1/2) + 0.420h(1) + 0.048h(2)$ is the function of the number of degrees of freedom of the particles with spins of 1/2, 1, and 2, respectively (Novikov and Frolov 1986).

It follows from formula (1) that the evaporation is most significant for low-mass PBHs. The question regarding the final evaporation stage of such objects arises. Alexeyev *et al.* (2000, 2001) showed that the BH mass cannot be smaller than some limiting mass determined by the coupling constant of the string theory.

According to the models with high-order curvature corrections in the effective action (Alexeyev *et al.* 2001), a PBH does not evaporate completely but only to some relic remnant. This relic remnant can exist at the present time $t_0$ in the Universe, provided that the PBH mass did not exceed the critical value of $M = M^* \approx 10^{15}$ g (Alexeyev and Khovanskaya 2000) at the reheating time $t = t_{\rm rh}$. For $M > M^*$, PBHs would continue to evaporate until $t = t_0$ and would have no time to evolve into their relic remnants.

Our main goal is to determine the conditions under which the relic remnants of PBHs have time to be formed by now.

Today, the inflation theory (Guth 1981) is a universally accepted theory for the early evolutionary stage of the Universe. According to this theory, the early Universe exponentially expands and then enters the reheating phase, when the matter temperature rises to $T = T_{\rm rh}$ (Kofman *et al.* 1994, 1997). The reheating temperature is determined by the energy of the scalar-field particles that provides inflation (Dolgov *et al.* 1988; Linde 2000). At present, only the range of possible reheating temperatures is known. Its upper limit is $m_{\rm up} \leq 3 \times 10^{16}$ GeV, as estimated by Melchiorri *et al.* (1999). At the same time, some authors (e.g., Libanov *et al.* 1998) believe that $m_{\rm up} \approx 1$ TeV.

## ESTIMATING THE REHEATING TEMPERATURE

Let us find the condition on the reheating temperature at which the evaporation of PBHs has finished by now, and the relic remnants of such objects have been formed. The temperature range must be determined by the critical PBH mass.

A BH is formed from an enhanced overdensity in the sizes of the comoving particle horizon. Therefore, the characteristic (most probable) BH mass at time $t$ is determined by the horizon sized, $l \sim t$ (Novikov *et al.* 1979).

Thus, the characteristic PBH mass is determined by the total mass within the particle horizon (Novikov *et al.* 1979):

$$M(t) = \frac{4}{3}\pi \left(a(t) \int_0^t \frac{d\tilde{t}}{a(\tilde{t})}\right)^3 \frac{3}{32\pi G t^2} \qquad (2)$$

*E-mail: khovansk@xray.sai.msu.ru

1063-7737/02/2803-0139$22.00 

$$= \gamma^{3/2}\frac{t}{t_{Pl}}m_{Pl},$$

where $a(t)$ is the scale factor calculated for the radiation-dominated Universe according to the law $a(t) \sim t^{1/2}$, and $\gamma^{3/2}$ denotes the following expression:

$$\gamma^{3/2} = \frac{t_{Pl}}{m_{Pl}}\frac{c^3}{G}.$$

According to Novikov *et al.* (1979), the BH mass at time $t = t_{\rm rh}$ is

$$M(t_{\rm rh}) = \gamma^{3/2}\frac{t_{\rm rh}}{t_{Pl}}m_{Pl}. \quad (3)$$

There are several reheating models (Kofman *et al.* 1997) that differ in duration. For a fast transition, the temperature can be used as a characteristic of the epoch.

We calculate the time $t_{\rm rh}$ from the condition of entropy constancy for two times ($t_{\rm rh}$ and $t_\gamma = t_0$), given that there were no significant phase transitions with a substantial jump in entropy in the Universe after reheating, as was pointed out by Dolgov *et al.* (1988) and Carr and Gilbert (1994).

The entropy $S$ is

$$S = N_f(t,T)T^3a^3,$$

where $N_f(t,T)$ is the number of degrees of freedom of the particles that exist at some time at the temperature of the Universe ($T$).

Let us write the equality between the entropies for the current and reheating times:

$$N_f|_{\rm rh}\, T_{\rm rh}^3 a(t_{\rm rh})^3 = N_f|_\gamma\, T_\gamma^3 a(t_\gamma)^3, \quad (4)$$

where $T_f|_\gamma$ is the current cosmic microwave background (CMB) temperature.

Taking into account the relationship between the scale factor and redshift, formula (4) can be rewritten as

$$N_f|_{\rm rh}\, T_{\rm rh}^3 = N_f|_\gamma\, T_\gamma^3(1+z_{\rm rh})^3.$$

The absence of significant phase transitions allows a relationship to be derived between the temperature of the particle horizon and the redshift. This makes it possible to calculate the redshift $z_{\rm rh}$ as a function of the current CMB temperature $T_\gamma$, the number of degrees of freedom at the reheating time, $N_f|_{\rm rh}$, and the number of degrees of freedom of the photons at present, $N_f|_\gamma$ ($N_f|_\gamma = 2$):

$$1 + z_{\rm rh} = \left(\frac{N_f|_{\rm rh}}{2}\right)^{1/3}\frac{T_{\rm rh}}{T_\gamma}. \quad (5)$$

To calculate the PBH mass at the reheating time $t = t_{\rm rh}$ using formula (3), we must derive a relation between time $t_{\rm rh}$ and redshift $z_{\rm rh}$. Reheating is known (Kofman *et al.* 1997) to take place at the radiation-dominated evolutionary stage of the Universe, which is characterized by the following density dependence of the pressure: $p = \epsilon/3$. Thus, the scale factor varies as $a(t) \sim t^{1/2}$. Hence,

$$\frac{a(t_0)}{a(t_{\rm rh})} = \left(\frac{t_0}{t_{\rm rh}}\right)^{1/2}, \quad (6)$$

and, consequently, the redshift at the reheating time is related to the initial time by

$$1 + z_{\rm rh} = \left(\frac{t_0}{t_{\rm rh}}\right)^{1/2}, \quad (7)$$

where $t_0 = (2/3)\, H_0^{-1}$ and $H_0$ is the Hubble constant at present.

According to formulas (5) and (7), we derive the following relation between $t_{\rm rh}$ and $T_{\rm rh}$:

$$t_{\rm rh} = \frac{2}{3}H_0^{-1}\left(\frac{2}{N_f|_{\rm rh}}\right)^{2/3}\left(\frac{T_\gamma}{T_{\rm rh}}\right)^2. \quad (8)$$

Using formulas (2) and (8), the temperature dependence of the PBH mass at the reheating time then takes the form

$$M(t_{\rm rh}) = \frac{2}{3}H_0^{-1}\gamma^{3/2}\frac{m_{Pl}}{t_{Pl}}\left(\frac{2}{N_f|_{\rm rh}}\right)^{2/3}\left(\frac{T_\gamma}{T_{\rm rh}}\right)^2. \quad (9)$$

We introduce the following designation to make the subsequent calculations more convenient:

$$T_0 = \frac{2}{3}\gamma^{3/4}\left(\frac{2}{N_f|_{\rm rh}}\right)^{1/3}\frac{1}{(t_{Pl}H_0)^{1/2}}T_\gamma.$$

It then follows from formula (9) that $T_{\rm rh} = \sqrt{m_{Pl}/M(t_{\rm rh})}T_0$.

Consider $M(t_{\rm rh}) = M^* \approx 10^{15}$ g. For $M > M^*$, as yet no relic remnants of PBHs have been formed by the present time $t = t_0$. The corresponding inequality for the reheating temperature is

$$T_{\rm rh} < \left(\frac{m_{Pl}}{M^*}\right)^{1/2}T_0. \quad (10)$$

Let us estimate $T_{\rm rh}$: $T_{\rm rh} < \sqrt{m_{Pl}/M^*}T_0 \approx \alpha \times 5.6 \times 10^7$ GeV, where

$$\alpha = \sqrt{2/3}\gamma^{3/4}\left(\frac{2}{N_f|_{\rm rh}}\right)^{1/3} \approx 3.3\left(\frac{2}{N_f|_{\rm rh}}\right)^{1/3}.$$

This implies that if the reheating temperature was lower than $\sim 10^8$ GeV, the relic remnants of PBHs have not yet formed by now and such BHs are still evaporating.

Our estimate of the reheating temperature at which PBHs can produce relic remnants at present is simple and correct in order of magnitude. However, when deriving it, we ignored details of the evolution of the Universe from $t = t_{\rm rh}$ to the current epoch.

## ALLOWANCE FOR THE DUST STAGE

Consider the transition from the radiation-dominated stage to the dust stage. As was mentioned above, in the radiation-dominated Universe, the scale factor depends on time as $a(t) \sim t^{1/2}$. In the dust Universe, the pressure is $p = 0$ and the scale factor depends on time as $a(t) \sim t^{2/3}$. The transition from one stage to the other takes place at the so-called decoupling time. Let us now estimate the reheating temperature more accurately by taking into account the parameters of the Universe at the decoupling time:

$$\frac{a(t_0)}{a(t_{\rm rh})} = \frac{a(t_{\rm d})}{a(t_{\rm rh})}\frac{a(t_0)}{a(t_{\rm d})}.$$

The redshift $z_{\rm rh}$ at $t = t_{\rm rh}$ is then

$$1 + z_{\rm rh} = \frac{a(t_0)}{a(t_{\rm rh})} = \frac{a(t_{\rm d})}{a(t_{\rm rh})}\frac{a(t_0)}{a(t_{\rm d})}.$$

By definition, the scale factor is related to the redshift by

$$\frac{a(t_0)}{a(t_{\rm d})} = 1 + z_{\rm d}.$$

Considering the radiation-dominated stage, we write a relation similar to formula (6):

$$\frac{a(t_{\rm d})}{a(t_{\rm rh})} = \left(\frac{t_{\rm d}}{t_{\rm rh}}\right)^{1/2}.$$

The latter three formulas reveal a relation between $t_{\rm rh}$, $t_{\rm d}$, $z_{\rm d}$, and $z_{\rm rh}$:

$$t_{\rm rh} = t_{\rm d}\left(\frac{1 + z_{\rm d}}{1 + z_{\rm rh}}\right)^2. \qquad (11)$$

Thus, the reheating time now also depends on the conditions in the Universe at the time of the transition from the radiation-dominated stage to the dust stage.

Similarly, to calculate the PBH mass given by formula (3), we must determine the redshift $z_{\rm d}$ at the decoupling time $t = t_{\rm d}$ and the time $t_{\rm d}$ itself. We infer these times from the following considerations.

The dust density for some fixed redshift $z$ is $\rho_m = 0.3(3H_0^2)/(8\pi G)$, $\rho_m(z) = (1+z)^3\rho_{m_0}$, and the radiation density is $\rho_\gamma = 10^{-4} \times (3H_0^2)/(8\pi G)$, $\rho_\gamma(z) = (1+z)^4\rho_{\gamma_0}$ (Dolgov *et al.* 1988). It thus follows that

$$\frac{\rho_\gamma(z)}{\rho_m(z)} = (1+z)\frac{\rho_{\gamma_0}}{\rho_{m_0}}.$$

At the decoupling time $t = t_{\rm d}$,

$$\frac{\rho_\gamma(z)}{\rho_m(z)} = 1, \frac{\rho_{\gamma_0}}{\rho_{m_0}} = \frac{\Omega_m}{\Omega_\gamma}, z = z_{\rm d}.$$

Therefore, the redshift at $t = t_{\rm d}$ is

$$z_{\rm d} = \frac{\Omega_m}{\Omega_\gamma} - 1 \approx 1.1 \times 10^4, \qquad (12)$$

where

$$\Omega_\gamma = \frac{4\sigma}{c}T^4\frac{8\pi G}{3H_0^2}.$$

Here, $\Omega_m \approx 0.2$ and $\sigma$ is the Boltzmann constant (Landau and Lifshitz 1980).

The corresponding time $t_{\rm d}$ inferred for the dust stage is

$$t_{\rm d} = \frac{t_0}{(1+z_{\rm d})^{3/2}} = \frac{2}{3}H_0^{-1}\frac{1}{(1+z_{\rm d})^{3/2}}. \qquad (13)$$

Thus, the reheating time determined from formula (11) now depends on the redshift at the decoupling time

$$t_{\rm rh} = \frac{2}{3}H_0^{-1}\frac{1}{(1+z_{\rm d})^{3/2}}\left(\frac{1+z_{\rm d}}{1+z_{\rm rh}}\right)^2.$$

Estimating $T_{\rm rh}$ relative to $M^*$, similar to our previous calculations [cf. formula (10)], we obtain

$$T_{\rm rh} < T_0\left(\frac{m_{Pl}}{M^*}\right)^{1/2}(1+z_{\rm d})^{1/4} \approx \alpha \times 5.7 \times 10^8,$$

where $T_0$ and $\alpha$ are equal to

$$T_0 = \frac{2}{3}\gamma^{3/4}\left(\frac{2}{N_f|_{\rm rh}}\right)^{1/3}\frac{1}{(t_{Pl}H_0)^{1/2}}T_\gamma$$

and

$$\alpha = \sqrt{2/3}\gamma^{3/4}\left(\frac{2}{N_f|_{\rm rh}}\right)^{1/3} \approx 3.3\left(\frac{2}{N_f|_{\rm rh}}\right)^{1/3},$$

respectively, and $z_{\rm d}$ is determined by condition (12).

The value of $N_f$ at the reheating time depends on the number of particles at given energies [e.g., $N_f \approx 115$ for $E \sim 100$ GeV (Rubakov 1987)].

When additional conditions at time $t = t_{\rm d}$ are taken into account, the lower limit for $T_{\rm rh}$ increases. Thus, the relic remnants of PBHs can exist at present at reheating temperatures higher than

$$T_{\rm rh} \sim 2\left(\frac{2}{N_f|_{\rm rh}}\right)^{1/3} \times 10^9 {\rm GeV}. \qquad (14)$$

## CONCLUSIONS

It follows form our study that if the reheating temperature exceeds $\approx 10^9$ GeV, then the relic remnants of PBHs can exist at present. These objects can become dark-matter candidates in the Universe.

## ACKNOWLEDGMENTS

This work was supported by the Program "Universities of Russia—Basic Research" (project no. 990777). We are also grateful to Prof. A.A. Starobinsky for helpful remarks.

## REFERENCES


1. S. O. Alexeyev, M. V. Sazhin, and M. V. Pomazanov, Int. J. Mod. Phys. D **10**, 225 (2001).
2. S. O. Alexeyev and O. S. Khovanskaya, Gravitation and Cosmology **6**, 14 (2000).
3. A. Barrau, Astropart. Phys. **12**, 269 (2000).
4. B. Carr and J. Gilbert, Phys. Rev. D **50**, 4853 (1994).
5. A. D. Dolgov, Ya. B. Zel'dovich, and M. V. Sazhin, *Cosmology of Early Universe* (Mosk. Gos. Univ., Moscow, 1988).
6. A. Dolgov, P. Naselsky, and I. Novikov, astro-ph/0009407 (2000).
7. A. Guth, Phys. Rev. D **23**, 347 (1981).
8. L. Kofman, A. Linde, and A. Starobinsky, Phys. Rev. Lett. **73**, 3195 (1994).
9. L. Kofman, A. Linde, and A. Starobinsky, Phys. Rev. D **56**, 3258 (1997).
10. L. D. Landau and E. M. Lifshitz, *Course of Theoretical Physics,* Vol. 5: *Statistical Physics* (Nauka, Moscow, 1988; Pergamon, Oxford, 1980).
11. M. Libanov, V. Rubakov, and P. Tinyakov, Phys. Lett. B **442**, 63 (1998).
12. A. Linde, Phys. Rep. **333**, 575 (2000).
13. A. Melchiorri, M. Sazhin, V. Shulga, and N. Vittorio, Astrophys. J. **518**, 562 (1999).
14. I. Novikov, A. Polnarev, A. Starobinsky, and Ya. Zeldovich, Astron. Astrophys. **80**, 104 (1979).
15. I. D. Novikov and V. P. Frolov, *Physics of Black Holes* (Nauka, Moscow, 1986; Kluwer, Dordrecht, 1989).
16. V. A. Rubakov, Mon. Not. R. Astron. Soc. **229**, 357 (1987).
17. S. Rubin, M. Khlopov, and A. Sakharov, Phys. Rev. D **62**, 083 505 (2000).


*Translated by A. Dambis*

*Astronomy Letters, Vol. 28, No. 3, 2002, pp. 143–149. Translated from Pis'ma v Astronomicheskiĭ Zhurnal, Vol. 28, No. 3, 2002, pp. 167–174.*


# Broadband Gravitational-Wave Pulses from Binary Neutron Stars in Eccentric Orbits

**A. V. Gusev[1], V. B. Ignatiev[2], A. G. Kuranov[1], K. A. Postnov[1,3,*], and M. E. Prokhorov[1]**

[1] *Sternberg Astronomical Institute, Universitetskii pr. 13, Moscow, 119899 Russia*
[2] *Moscow State University, Vorob'evy gory, Moscow, 119899 Russia*
[3] *Max-Planck-Institut für Astrophysik, Karl Schwarzschild Strasse 1, 86740 Garching bei München, Germany*

Received October 25, 2001

**Abstract**—The gravitational-wave radiation from binary stars in elliptical orbits peaks at times close to the periastron passage. For a stationary distribution of binary neutron stars in the Galaxy, there are several systems with large orbital eccentricities and periods in the range from several tens of minutes to several days from which gravitational-wave radiation at periastron will be observed as a broad pulse in the frequency range 1–100 mHz. The LISA space interferometer will be able to record pulsed signals from these systems at a signal-to-noise ratio $S/N > 5\sqrt{5}$ in the frequency range $\sim 10^{-3}$–$10^{-1}$ Hz. Algorithms for detecting such signals are discussed. © *2002 MAIK "Nauka/Interperiodica"*.

## INTRODUCTION

The first broadband laser interferometers (LIGO, VIRGO, GEO-600), whose sensitivity in the frequency range 10–1000 Hz will be high enough to observe astrophysical gravitational-wave (GW) sources, will soon be put into operation [see Braginskii (2000) and references therein]. It is generally recognized that close binaries composed of neutron-star (NS) and black-hole (BH) pairs are among the highest priority GW sources [see Grishchuk *et al.* (2001) for more details]. In the high-frequency range, for which ground-based GW inteferometers are designed,[1] the phase of spiral approach of two stars and their coalescence will be observed. The coalescence of NSs can in principle be accompanied by grandiose astrophysical phenomena in the electromagnetic spectral range with energy release of the order of a substantial fraction of the NS binding energy [e.g., by cosmic gamma-ray bursts (Blinnikov *et al.* 1984)].

For two identical solar-mass particles in a circular orbit with period $P$, the time of spiral approach in the quadrupole approximation is

$$t_0 \sim 10^5 (P/[1\ \mathrm{s}])^{8/3}\ [\mathrm{s}],$$

i.e., about 20 min for $P = 0.2$ s, which corresponds to the GW frequency of 10 Hz at the lower sensitivity limit of a ground-based interferometer. The signal is quasi-periodic in nature, with an increasing frequency and amplitude (chirp) as the stars approach each other. We can accurately determine the shape of the presumed signal and use the optimum filtering technique that is well-known in radiophysics (Tikhonov 1966) for its detection [see the review by Grishchuk *et al.* (2001) for more details].

A search for GWs at lower frequencies is possible with space antennas. The most important and advanced project in this area is the LISA space interferometer (Bender *et al.* 2000). The projected sensitivity of this interferometer lies in the range $10^{-4}$–$10^{-1}$ Hz. Mergers of binary supermassive BHs in galactic nuclei, individual close binaries in our Galaxy, and, possibly, the relic GW background that arose in the early Universe (Grishchuk *et al.* 2001) are presumed to be major astrophysical sources for this antenna. Galactic binaries with compact stars (white dwarfs, NSs, and BHs) mainly produce a stochastic background at frequencies below 1 mHz. The stochastic background and the possibility of detecting GW signals from individual binaries with compact objects by LISA over an observing period of one year have recently been considered in detail by Nelemans *et al.* (2001).

Here, we study the GW signals from binary NSs in highly eccentric orbits that are in the shape of broadband pulses with a repetition period from several tens of minutes to several hours in the frequency range $10^{-3}$–$10^{-1}$ Hz. These pulses emerge when the NSs approach each other at periastron. Their duration is

* E-mail: pk@sai.msu.ru

[1] Recall that the frequency sensitivity of ground-based interferometers is limited below by seismic noises.

determined by the time of passage near the periastron, where the most intense GW generation takes place. For a stationary Galactic merger rate of binary NSs equal to $10^{-4}$ events per year, the number of systems that are capable of emitting such pulses at frequencies 1–100 mHz with an amplitude that is a factor of $5\sqrt{5}$ higher than the LISA noise level proves to be $\sim$7.

## A STATIONARY DISTRIBUTION FUNCTION OF BINARY NSs IN THE GALAXY

Binary NSs (and BHs) are a natural result of the evolution of massive binary stars. In the case of NSs, a type II (in sufficiently wide systems) or type Ib/c (if the hydrogen envelope was lost during mass transfer) supernova explosion occurs in the system twice. The mass loss by one of the binary components in a circular orbit during a supernova explosion that occurs in a time much shorter than the orbital period (the approximation of instantaneous ejection) is known (Blaauw 1961) to make the new orbit noncircular with the eccentricity $e = \Delta M/M'$, where $\Delta M$ is the lost mass and $M'$ is the total binary mass after the explosion. If there are an additional asymmetry in the collapse, which is quantitatively characterized by the additional space velocity acquired by the young NS [as suggested by the observations of radio-pulsar space velocities (Lyne and Lorimer 1994; Arzoumanian *et al.* 2001)] and misalignment of the axes of some NSs with the orbital angular momentum, for example, in the binary pulsar PSR B1259–63 (Postnov and Prokhorov 1997) and PSR J2051–0827 (Doroshenko *et al.* 2001), then the orbital eccentricities of the forming binary NSs generally become even larger.

Apart from the amplitude characteristic of the GW signal, the expected frequency of occurrence of particular events is also of considerable importance. Presently, a good theoretical estimate for the merger rate of Galactic binary NSs is considered to be $10^{-4}$–$10^{-5}$ events per year [Lipunov *et al.* 1997; Portegies Zwart and Yungelson 1998; and other more recent papers; see Grishchuk *et al.* (2001) for more details]. The main theoretical uncertainty in the merger rate results from the unknown anisotropy in the collapse [see Grishchuk *et al.* (2001) for a detailed discussion]. Since only systems whose orbits decay because their orbital angular momentum and energy are carried away by GWs in a time shorter than the Galactic age $\sim 10^{10}$ years merge together, the formation rate of Galactic binary NSs and BHs is even higher. Therefore, we expect that at least about $N = 10^6$ such binaries can simultaneously exist in the Galaxy.

Assuming that the orbital evolution of a binary of compact stars is entirely determined by the energy losses through GW radiation (a good approximation for sufficiently rarefied stellar fields; in dense star clusters, the dynamical interaction of stars should be taken into account) and that the conditions for star formation in the Galaxy are stationary (a reasonable approximation for the past several billion years), we can calculate the distribution function of binary NSs in their orbital parameters (semimajor axis $a$ and eccentricity $e$), $dN(a, e)$, with the normalization $N = \int dN(a, e)da\,de$. This problem was solved for model initial orbital-parameter distributions by Buitrago *et al.* (1994). Ignatiev *et al.* (2001) derived the distribution function $dN(a, e)$ for the initial orbital parameters of binary NSs computed by the Monte Carlo method using the "scenario machine" code designed to compute the binary evolution (Lipunov *et al.* 1996). In the domain of parameters $a$ and $e$ where the coalescence occurs in a time shorter than the Galactic age, the distribution function becomes stationary. A portion of the stationary distribution function computed for the kick velocity during the collapse that follows a Maxwellian distribution with a mean of 200 km s$^{-1}$ is shown in Fig. 1. It was normalized to the binary NS merger rate of $10^{-4}$ per year for a Galactic mass of $10^{11} M_\odot$. The function increases sharply at low frequencies (large orbital periods).

## GW SIGNALS FROM BINARY NSs DURING PERIASTRON PASSAGE

A binary star with component masses $M_1$ and $M_2$ in a noncircular orbit emits GWs over a wide frequency range at harmonics of the Keplerian frequency $(2\pi\nu_K)^2 = G(M_1 + M_2)/a^3$ (Peters and Mathews 1963). Most of the energy is emitted during the passage near the periastron $a_p = a(1 - e)$. For large eccentricities, the GW burst duration is approximately equal to $\tau \sim a_p/v_p$ ($v_p$ is the velocity at periastron) and the radiation peaks at the harmonic with the number $n \sim (\tau\nu_K)^{-1} \sim (1 - e)^{-3/2}$, in accordance with Kepler's third law.

Let us determine more accurately the emission time of most of the energy when a NS moves near the periastron. We make use of the standard expression for GW radiation in an elliptical orbit averaged over the spatial orbital orientation (Peters and Mathews 1963; Landau and Lifshitz 1973):

$$-\frac{dE}{dt} = \frac{8G^4 M_1^2 M_2^2 (M_1 + M_2)}{15a^5 c^5 (1 - e^2)^5}(1 + e\cos\phi)^4 \quad (1)$$
$$\times [12(1 + e\cos\phi)^2 + e^2 \sin^2\phi],$$

where $G$ is the Newton gravitational constant, $c$ is the speed of light, and $\phi$ is the polar angle measured from the periastron. Next, we define the GW pulse duration $\tau$ during periastron passage as the time during which 90% of the energy released in one orbital period $P$ is emitted. Let us pass from the integration over time $t$ to the integration over polar angle $\phi$ by changing variables

$$d\phi = \frac{(1+e\cos\phi)^2}{(1-e^2)^{3/2}}\sqrt{\frac{G(M_1+M_2)}{a^3}}dt$$

(the change in orbital energy and angular momentum in one period is assumed to be small and to have no effect on the Keplerian orbital parameters; this assumption is valid for the frequencies under consideration). The dependence of polar angle $\phi_{90}$, which determines the corresponding segment of the orbit, is shown in Fig. 2a. A plot of $\tau/P$ against eccentricity is shown in Fig. 2b. Beginning from an eccentricity $\sim$0.5, this angle is $\sim 60^\circ$ for $\tau_{90}$ and changes little with increasing eccentricity (an intuitively understandable result: at large $e$, the focal parameter of the ellipse, $p$, and the distance at periastron, $a_p$, change equally $\sim(1-e)$, and the periastron parts of the orbit at different $e$ are similar to each other). It also follows from Fig. 2 that 90% of the energy is radiated in 1/3 of the orbital period even at an eccentricity of about 0.3. Below, we take $e = 0.3$ as a lower limit on the eccentricities of binary NSs that produce broadband GW pulses.

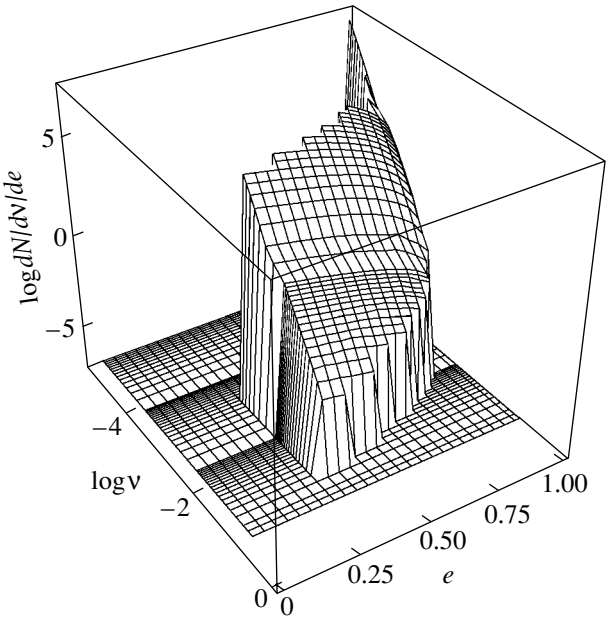


**Fig. 1.** The stationary distribution function of Galactic binary NSs, $\log dN/d\nu/de$, computed by Ignatiev *et al.* (2001) for a Maxwellian kick-velocity distribution of newborn NSs with a mean of 200 km s$^{-1}$. It is normalized to the rate of mergers through GW radiation $10^{-4}$ per year. A portion is shown for systems with $e > 0.3$ that merge together in a time >1 year (an upper limit in frequencies and eccentricities) and with a GW amplitude at periastron $h_{\max}$, Eq. (2), which gives a signal-to-noise ratio of $5\sqrt{5}$ for a single sequence of pulses (4).

Thus, during the periastron passage of a binary NS in an elliptical orbit, a signal will be emitted in a broad frequency band, $\Delta\nu_b \sim 1/\tau$. The pulses have the duration $\tau$, repetition period $P$, and an amplitude for which we take an estimate of the maximum dimensionless wave amplitude $h_{\max}$ at periastron. Averaging the squares of the field amplitudes (Peters and Mathews 1963; Moreno-Garrido *et al.* 1995) over the binary orientation relative to the observer yields

$$h_{\max} = \sqrt{h_+^2 + h_\times^2}\Big|_{\phi=0} = \sqrt{\frac{32}{5}}\frac{G^2 M_1 M_2}{c^4 a(1-e^2)} \quad (2)$$
$$\times \frac{1}{r}(1 + 3e + \frac{10}{3}e^2 + \frac{5}{3}e^3 + \frac{1}{3}e^4)^{1/2},$$

where $r$ is the distance to the system. In the limit $e \to 1$, this maximum amplitude is a factor of $\sqrt{28/3} \approx 3$ larger than the amplitude in a circular orbit with the radius equal to the ellipse parameter $p$ and a factor of $\sim$1.5 larger than the amplitude in a circular orbit with the radius equal to the distance at periastron. Note also that the mean amplitude $\sqrt{h_+^2 + h_\times^2}$ changes with increasing eccentricity by no more than a factor of 2 and 4.5 for $\tau_{90}$ and $\tau_{99}$, respectively, at the ends of the corresponding time intervals (Fig. 2b).

Numerical estimates require knowledge of the distance to the source. Since the center of mass during the formation of binary NSs can acquire a significant space velocity, any subsystem of Galactic binary NSs will be larger in size than any subsystem of ordinary stars. Quantitative calculations have been performed repeatedly (Bulik *et al.* 1999), and we make use of their results. For a NS kick velocity during collapse of 200 km s$^{-1}$, the mean distance from the binary NS to the Sun is 12.15 kpc. We assume all binary NSs to be at this mean distance.

## DETECTING BROADBAND GW SIGNALS

To calculate the expected detection rate of the GW pulses considered above requires refining the technique for their possible detection. First, let us choose the frequency range for pulse detection. The detection of GW signals in the LISA band at low frequencies, down to $\sim 10^{-3}$ Hz, is known (Grishchuk *et al.* 2001; Nelemans *et al.* 2001) to be complicated[2] by the

[2]But is not completely ruled out; see Hellings (2001).

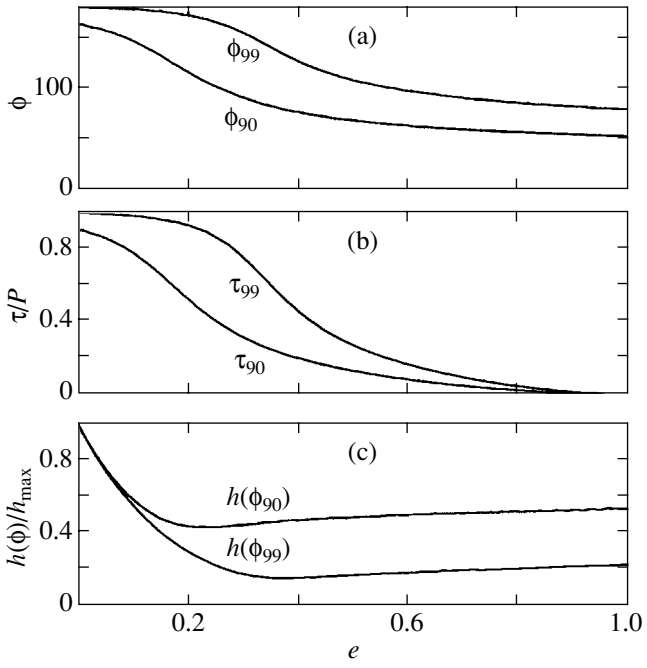


**Fig. 2.** (a) The polar angle $\phi$ of an elliptical orbit within which 99% ($|\phi| < \phi_{99}$) and 90% ($|\phi| < \phi_{90}$) of the GW energy is emitted during the periastron passage versus eccentricity $e$; (b) radiation duration $\tau_{99}$ and $\tau_{90}$, in units of the orbital period $P$, versus $e$; and (c) mean amplitude $h(\phi)/h_{\max}$ at the boundary points of the orbit $\phi_{90}$ and $\phi_{99}$ versus $e$.

stochastic background from unresolved binary white dwarfs [the stochastic GW background from binary NSs in elliptical orbits, even if the many harmonics at which radiation occurs are taken into account, is severalfold lower, because the number of binary NSs is much smaller than that of white dwarfs; see Ignatiev *et al.* (2001) for more details]. Therefore, we consider below only the frequency range $10^{-3}$–$10^{-1}$ Hz.

The binary NSs in elliptical orbits whose radiation at periastron falls within the above frequency range can have orbital periods $P$ from several tens of minutes (for nearly circular orbits) to several days (for significant eccentricities). This means that over an observing time of one year ($T \approx 3 \times 10^7$ s), the signal from a single system will be a periodic sequence of $k = T/P$ broadband pulses with random (from the beginning of the observations) initial phases. The source direction is not known *a priori* either. There are definitely more than one such system [see Nelemans *et al.* (2001) and below]. Thus, from the viewpoint of detection, the signal is a superposition of periodic sequences of broad pulses $s_i(t)$ with random phases and different repetition periods, $s(t) = s_1(t) + s_2(t) + \ldots + s_n(t)$. We emphasize that in the above frequency range, such a signal does not produce a continuous background at the detector frequency resolution $\Delta\nu = 3 \times 10^{-8}$ Hz (Ignatiev *et al.* 2001) for the projected LISA sensitivity $S_n$.

Consider an ideal case where there is only one sequence of such pulses. The signal-to-noise ratio for the observation of a single broad pulse with duration $\tau$ by a detector with sensitivity $S_n\,[\mathrm{Hz}]^{-1/2}$ is

$$(\mathrm{S/N})_1 = \frac{h_{\max}}{\sqrt{\Delta\nu_b S_n}}, \qquad (3)$$

where $\Delta\nu_b = 1/\tau$ is the pulse width in the frequency representation. For a periodic sequence of $k$ identical pulses, we have

$$(S/N)_k = (S/N)_1\sqrt{k} = \frac{h_{\max}}{\sqrt{\Delta\nu S_n}}\sqrt{\frac{\tau}{P}}, \qquad (4)$$

where $\Delta\nu = 1/T = 3 \times 10^{-8}$ Hz is the maximum frequency resolution of the detector over the time of continuous observations.

As an example, let us consider the Hulse–Taylor-type pulsar PSR B1913+16 with the orbital parameters (Taylor and Weisberg 1989) $a = 1.95 \times 10^{11}$ cm, $P = 27\,907$ s, and $e = 0.617$; the component masses closely match, $M_1 \approx M_2 = 1.4M_\odot$, and the distance to the system is $\simeq$5 kpc. Averaging over the orientation yields $h_{\max} \approx 10^{-22}$. For an eccentricity of 0.617, the duration $\tau_{90} \approx 0.15P = 4186$ s, $\Delta\nu_b \approx 0.23$ mHz, the frequency of the highest (fourth) harmonic is $\approx$0.18 mHz, and the signal-to-noise ratio over a year of continuous observations estimated from formula (4) is a mere 0.5 (disregarding the noise from

binary white dwarfs, which prevails in this frequency range). Clearly, such sources are of no interest.

For a pulsed signal from an unknown direction, it is usually required that $S/N > 5\sqrt{5}$, where the factor $\sqrt{5}$ takes into account the source's unknown coordinates (Thorne 1987). At such a high detection threshold, the integral of the stationary distribution function over the region with systems that give such an amplitude is $\sim 7$. Naturally, lowering the detection threshold increases this number (to 15 for $S/N = 5$). Choosing a different pulse duration (e.g., $\tau_{99}$ instead of $\tau_{90}$) could formally cause an increase in the number of detected systems through a narrowing of the band $\Delta\nu_b$ in Eq. (3). In this case, however, systems beginning with a larger eccentricity ($\sim 0.5$) should be taken in order that the pulse duration be less than 1/3 of the orbital period. The range of the distribution function will narrow, and the number of systems will actually decrease.

The distribution of binary NSs for the stationary distribution function under consideration in pulse duration and orbital period is shown in Fig. 3. We see that pulses with a duration of about 100 s have the highest probability of being detected among systems with orbital periods $\sim 1000$ s. In this case, the mean eccentricity is $\sim 0.5$, as follows from Fig. 2b.

Thus, in reality, there must simultaneously be signals from several systems with high amplitudes at maximum. In the case of many systems, we face a typical problem of estimating the parameters of a quasi-deterministic signal against a noise background. For Gaussian noises and for a specified number of sources, this problem can be solved exactly by using a well-developed signal detection technique in radiophysics (Tikhonov 1966). The basic principles in constructing optimum receivers to detect a quasi-deterministic signal against a Gaussian noise background are given in the Appendix.

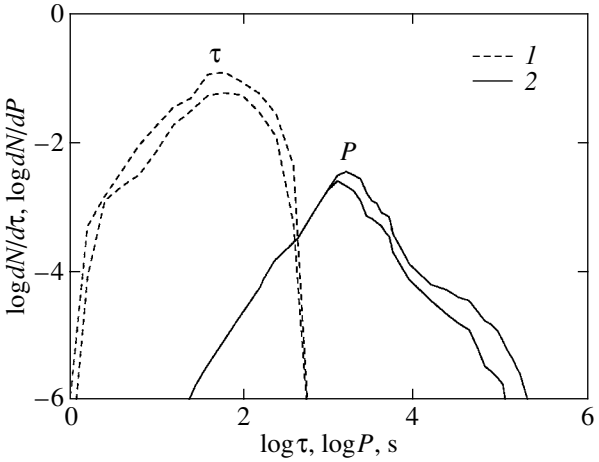


**Fig. 3.** The distribution of binary NSs whose signal at periastron exceeds the LISA background by a factor of $5\sqrt{5}$ and 5 (*1*) in pulse duration $\tau_{90}$ and (*2*) in orbital periods $P$. The stationary distribution function shown in Fig. 1 is used. The integral of the distributions is $\sim 7$ for $S/N = 5\sqrt{5}$ (lower curves) and $\sim 15$ for $S/N = 5$ (upper curves).

## DISCUSSION

(1) A *stationary* distribution of Galactic binary NSs in orbital parameters is one of our principal assumptions. This assumption is a good approximation, when the binary evolution time scale is much shorter than the time scale of a significant change in the parameters of the initial distribution function of the sources. We assume that the Galactic star formation may be considered stationary, at least in the past 5 Gyr [Nelemans *et al.* (2001) used a different assumption]. Since the evolution time of binary NSs in noncircular orbits in the frequency range $10^{-5}$–$10^{-1}$ Hz of interest is shorter than this time, the stationarity has time to be established. An increase in star-formation rate in the past will naturally cause an increase in the distribution function, particularly at low frequencies. However, the formation parameters of binary NSs, in particular, the additional kick velocity during collapse, have a more significant effect on the distribution function.

(2) The *normalization* of the distribution function to the merger rate of binary NSs, $10^{-4}$ per year, is a good estimate close to the universally accepted *upper* limit on such estimates [see Grishchuk *et al.* (2001) and references therein]. Changing this normalization will cause a corresponding change in the results obtained.

(3) We do not consider the more numerous class of potential NS + massive white dwarf (WD) sources. Systems in circular orbits are beyond the scope of our analysis, while NS + massive WD systems in elliptical orbits (Portegies Zwart and Yungelson 1999) in the frequency range under consideration are virtually indistinguishable from binary NSs. The formation of binaries with an old WD and a young NS, whose representatives can be the radio pulsars in eccentric orbits PSR B2303+46 and PSR J1141−6545, was analyzed in detail by Tauris and Sennels (2000). They found that the (model-dependent) formation rate of such systems in the Galaxy could appreciably exceed the birth rate of binary NSs (Brown *et al.* 2001). We also omit compact binaries with black holes, because they are few in number compared to binary NSs. The possible contribution from NS + WD, WD + NS, and BH + NS in noncircular orbits will increase the number of pulses under consideration.

## CONCLUSIONS

We have analyzed the pulsed signals from binary compact stars in noncircular orbits. We showed that in the special case of a stationary distribution of binary NSs in orbital parameters (semimajor axis and eccentricity) normalized to the Galactic merger rate of $10^{-4}$ per year in the frequency range $10^{-3}$–$10^{-1}$ Hz, one might expect the detection of $\sim$7 GW signal sources of this type at a signal-to-noise ratio of $5\sqrt{5}$ for the LISA space detector. Allowance for other possible compact binaries (NSs with white dwarfs or black holes) will cause the number of such sources to increase. The signal from each system is a sequence of broad pulses with equal amplitudes. The most probable pulse width is $\sim$100 s, and the pulse repetition period (the orbital period of a binary NS) is $\sim$1000 s. We discussed optimum algorithms for detecting such a quasi-deterministic signal against an additive noise background in terms of the detection theory.

## ACKNOWLEDGMENTS

We wish to thank L.R. Yungelson for a constructive discussion and helpful remarks. This study was supported in part by the Russian Foundation for Basic Research (project nos. 00-02-17164, 00-02-17884a, and 01-15-99310m).

## *APPENDIX*

Let

$$x(t) = S(t, \Theta_1, \ldots, \Theta_N) + n(t), \quad 0 \leqslant t \leqslant T$$

be the additive mixture of a useful quasi-deterministic signal $S(t)$,

$$S(t, \Theta_1, \ldots, \Theta_N) = \sum_{i=1}^{N} \Theta_i S_i(t), \quad 0 \leqslant t \leqslant N,$$

where $\Theta = (0, 1)$ are the detection parameters, and a Gaussian noise $n(t)$ with a known correlation function $K_n(\tau)$.

*A. The detection parameters are known.* The presence of a useful signal is hypothesized if the following condition is satisfied (Sosulin 1992):

$$Z(\mathbf{Y}, \Theta_1, \ldots, \Theta_N) = \sum_{i=1}^{N} \Theta_i Y_i - \frac{1}{2} \sum_{i=1}^{N} \sum_{k=1}^{N} \Theta_i \Theta_k \rho_{ik} > C_\alpha. \quad \text{(A1)}$$

Here,

$$\mathbf{Y} = (Y_1, \ldots, Y_N)$$

$$Y_i = \int_0^T x(t) u_i(t) dt, \quad \rho_{ik} = \int_0^T S_i(t) u_k(t) dt,$$

where the reference signal $u_i(t)$, $i = \overline{1, N}$, is the solution of a Fredholm integral equation of the first type:

$$\int_0^T K_n(t - \tau) u_k(\tau) d\tau = S_k(t), \quad 0 \leqslant t \leqslant T.$$

The threshold level $C_\alpha$ depends on the probability of false alarm $\alpha$ (the Neumann–Pearson criterion).

An analysis of expression (A1) shows that an optimum receiver for the known detection parameters is an $N$-channel linear system. The main element of an individual channel is a correlation receiver that forms the variable $Y_i$, $i = \overline{1, N}$ (in the filtering case, the correlation receiver is replaced with an optimum filter).

*B. The detection parameters $\Theta_i$ are unknown. The Bayesian detection algorithm.* We assume that the detection parameters $\Theta_i$ are independent, discrete random variables with a known distribution:

$$P\{\Theta_i = 1\} = p_i, \quad P\{\Theta_i = 0\} = 1 - p_i, \quad i = \overline{1, N}.$$

It may be shown that for a parametric *a priori* uncertainty, the presence of a quasi-deterministic signal $S(t, \Theta_1, \ldots, \Theta_N)$ is hypothesized if

$$Z(\mathbf{Y}, \hat{\Theta}_{1B}, \ldots, \hat{\Theta}_{NB}) > C_\alpha, \quad \text{(A2)}$$

where $\hat{\Theta}_{iB}$ is the Bayesian estimate of the unknown parameter in the quadratic payoff function:

$$\hat{\Theta}_{iB} = = \underbrace{\int \ldots \int}_{N} \Theta_i \exp\{Z(\mathbf{Y}, \Theta_1, \ldots, \Theta_N)\} \times W_{pr}(\Theta_1, \ldots, \Theta_N) d\Theta_1 \ldots d\Theta_N, \quad \text{(A3)}$$

$$W_{pr}(\Theta_1, \ldots, \Theta_N) = \prod_{i=1}^{N} [(1 - p_i)\delta(\Theta_1) + p_i \delta(\Theta_i - 1)]$$

is the *a priori* joint probability density of the random variables $\Theta_1, \ldots, \Theta_N$.

*C. The detection parameters are unknown. A non-Bayesian detection algorithm.* For a nonparametric *a priori* uncertainty, the detection parameters $\Theta_i$ are considered as nonrandom. When a receiver is synthesized, the unknown parameters $\Theta_i$ are replaced with the maximum likelihood estimates $\hat{\Theta}_i$, which leads to the following deciding rule:

$$Z(\mathbf{Y}, \hat{\Theta}_1, \ldots, \hat{\Theta}_N) > C_\alpha. \quad \text{(A4)}$$

The maximum likelihood estimates $\hat{\Theta}_i$ are chosen in such a way that

$$Z(\mathbf{Y}, \hat{\Theta}_1, \ldots, \hat{\Theta}_N) \quad \text{(A5)}$$

$$> \max_{\Theta_1,\ldots,\Theta_N} Z(\mathbf{Y},\Theta_1,\ldots,\Theta_N).$$

An analysis of expressions (A2)–(A5) shows the following:

(1) When a quasi-deterministic signal $S(t,\Theta_1,\ldots,\Theta_N)$ is detected, the receiver includes an additional element, an estimator of the unknown detection parameters $\Theta_1,\ldots,\Theta_N$.

(2) The detection algorithms (A2) and (A4) are nonlinear: $\hat{\Theta}_i = \hat{\Theta}_i(\mathbf{Y})$, $\hat{\Theta}_i = \Theta_i(\mathbf{Y}) \neq \hat{\Theta}_{iB}$.

(3) For a non-Bayesian detector algorithm, the estimator of the unknown detector parameters is a multichannel linear system [see (A5)], whose resulting signal arrives at a comparator.

(4) The detection of a quasi-deterministic signal $S(t,\Theta_1,\ldots,\Theta_N)$ using algorithms (A2) and (A4) may be considered as the simultaneous detection and measurement of parameters $\Theta_i$ for the useful signal.

(5) Since the Bayesian estimator is essentially nonlinear in structure, such systems are not in wide use.

The threshold level $C_\alpha$ in expressions (A2) and (A4) is given by the following equations:

$$\left.\begin{aligned} &P\{Z(\mathbf{Y},\hat{\Theta}_{1B},\ldots,\hat{\Theta}_{NB}) \\ &> C_\alpha|_{\Theta_1=\Theta_2=\ldots=\Theta_1=0}\} = \alpha, \\ &P\{Z(\mathbf{Y},\hat{\Theta}_1,\ldots,\hat{\Theta}_N) \\ &> C_\alpha|_{\Theta_1=\Theta_2=\ldots=\Theta_1=0}\} = \alpha, \end{aligned}\right\} \quad \text{(A6)}$$

where $\hat{\Theta}_{iB}$ and $\hat{\Theta}_i$ in expression (A6) are the pseudoestimators of the unknown detector parameters in the absence of a useful signal.

Since algorithms (A2) and (A4) are nonlinear, the distribution functions (A6) can be computed only empirically by computer simulations of Gaussian noises with a specified correlation function (with a specified spectral density).

## REFERENCES


1. Z. Arzoumanian, D. F. Chernoff, and J. M. Cordes, Astrophys. J. (2001) (in press); astro-ph/0106159.
2. P. L. Bender, K. Danzmann, *et al.*, LISA: Laser Interferometer Space Antenna. A Cornerstone Mission for the Observation of Gravitational Waves—System and Technology Study Report, ESA-SCI(2000)11 (2000); Available at ftp://ftp.rzg.mpg.de/pub/grav/lisa/sts-1.04.pdf.
3. A. Blaauw, Bull. Astron. Inst. Netherlands **15**, 265 (1961).
4. S. I. Blinnikov, I. D. Novikov, T. V. Perevodchikova, and A. G. Polnarev, Pis'ma Astron. Zh. **10**, 422 (1984) [Sov. Astron. Lett. **10**, 177 (1984)].
5. V. B. Braginskii, Usp. Fiz. Nauk **170**, 743 (2000).
6. G. E. Brown, C. H. Lee, Portegies S. F. Zwart, and H. A. Bethe, Astrophys. J. **547**, 345 (2001).
7. J. Buitrago, C. Moreno-Garrido, and E. Mediavilla, Mon. Not. R. Astron. Soc. **268**, 841 (1994).
8. T. Bulik, K. Belczynski, and W. Zbijewski, Mon. Not. R. Astron. Soc. **309**, 629B (1999).
9. O. Doroshenko, O. Loehmer, M. Kramer, *et al.*, Astron. Astrophys. (2001), in press; astro-ph/0110023.
10. L. P. Grishchuk, V. M. Lipunov, K. A. Postnov, *et al.*, Usp. Fiz. Nauk **171**, 3 (2001).
11. R. W. Hellings, gr-qc/0110052.
12. V. B. Ignatiev, A. G. Kuranov, K. A. Postnov, and M. E. Prokhorov, Mon. Not. R. Astron. Soc. **327**, 531 (2001).
13. L. D. Landau and E. M. Lifshitz, *The Classical Theory of Fields* (Nauka, Moscow, 1973; Pergamon, Oxford, 1975).
14. V. M. Lipunov, K. A. Postnov, and M. E. Prokhorov, Astrophys. Space Phys. Rev. **9**, 1 (1996).
15. V. M. Lipunov, K. A. Postnov, and M. E. Prokhorov, Mon. Not. R. Astron. Soc. **288**, 245 (1997).
16. A. G. Lyne and D. R. Lorimer, Nature **369**, 127 (1994).
17. C. Moreno-Garrido, E. Mediavilla, and J. Buitrago, Mon. Not. R. Astron. Soc. **274**, 115 (1995).
18. G. Nelemans, L. R. Yungelson, and S. F. Portegies Zwart, Astron. Astrophys. **375**, 890 (2001); astro-ph/0105221.
19. P. S. Peters and J. Mathews, Phys. Rev. **131**, 435 (1963).
20. S. F. Portegies Zwart and L. R. Yungelson, Astron. Astrophys. **332**, 173 (1998).
21. S. F. Portegies Zwart and L. R. Yungelson, Mon. Not. R. Astron. Soc. **309**, 26 (1999).
22. K. A. Postnov and M. E. Prokhorov, Pis'ma Astron. Zh. **23**, 503 (1997) [Astron. Lett. **23**, 439 (1997)].
23. Yu. G. Sosulin, *Theoretical Foundations of Radar and Radio Navigation* (Radio i Svyaz', Moscow, 1992).
24. T. M. Tauris and T. Sennels, Astron. Astrophys. **355**, 236 (2000).
25. J. H. Taylor and J. M. Weisberg, Astrophys. J. **345**, 434 (1989).
26. K. S. Thorne, in *Three Hundred Years of Gravitation,* Ed. by S. W. Hawking and W. Israel (Cambridge Univ. Press, Cambridge, 1987), p. 330.
27. V. I. Tikhonov, *Statistical Radiophysics* (Sovetskoe Radio, Moscow, 1966).


*Translated by V. Astakhov*

*Astronomy Letters, Vol. 28, No. 3, 2002, pp. 150–162. Translated from Pis'ma v Astronomicheskiĭ Zhurnal, Vol. 28, No. 3, 2002, pp. 175–188.*


# The Formation of X-ray Radiation in a Boundary Layer during Disk Accretion onto a Neutron Star

**S. A. Grebenev[1, 2, *] and R. A. Sunyaev[2, 1]**

[1] *Space Research Institute, Russian Academy of Sciences, Profsoyuznaya ul. 84/32, Moscow, 117997 Russia*

[2] *Max-Planck-Institut für Astrophysik, Karl Schwarzschild Strasse 1, 86740 Garching bei München, Germany*

Received December 25, 2000; in final form, October 29, 2001

**Abstract**—We present computed radiation spectra for the boundary layer (BL) of the accretion disk that is formed near the surface of a neutron star. Both free-free processes and Comptonization were taken into account. Our computations are based on the hydrodynamic solution obtained by Popham and Sunyaev (2001) for the BL structure. The computed spectra are highly diluted compared to the Planck spectra of the same surface temperature. They are complex in shape; in particular, an intense Wien emission component is formed in their high-energy region at high accretion rates. In general, the computed spectra are harder than those observed in actual X-ray sources. This is the result of a very high temperature found by Popham and Sunyaev (2001) for the BL. We show that such temperatures could result from an oversimplified treatment of radiative transfer in their paper, which completely ignored the frequency dependence of the matter opacity and radiation intensity. Our computations indicate that at moderate accretion rates, a proper treatment of radiative transfer with allowance for Comptonization leads to appreciably lower plasma temperatures and to softer radiation spectra. © *2002 MAIK "Nauka/Interperiodica"*.

Key words: *accretion, boundary layer, Comptonization, neutron stars, X-ray sources*

## 1. INTRODUCTION

During disk accretion onto a weakly magnetized neutron star (NS), a substantial fraction of the energy of infalling material radiates away in a narrow layer at the boundary between the inner edge of the accretion disk and the stellar surface. In this boundary layer (BL), the angular velocity of the material decreases from the Keplerian angular velocity $\Omega_K = (GM_*/R_*^3)^{1/2} = (0.5R_g/R_*)^{1/2}c/R_*$ (typical of the disk), where $R_g = 2GM_*/c^2$ is the gravitational radius of the NS, to a considerably lower rotation velocity $\Omega_*$ of the star itself. If the stellar radius $R_*$ exceeds the radius of the marginally stable orbit ($3R_g$), then the BL luminosity in the Newtonian approximation is $L_b = 0.5\dot{M}R_*^2(\Omega_K - \Omega_*)^2$ (Shakura and Sunyaev 1988; Kluzniak 1988); i.e., it accounts for almost half of the total accretion luminosity $L_a = 0.5\dot{M}c^2(R_g/R_*)$. At $R_* < 3R_g$, the BL luminosity can appreciably exceed the disk luminosity. For a nonrotating star with the Schwarzschild metric, $L_b = (8/9)^{1/2} - (1 - R_g/R_*)^{1/2}$ and $L_d = 1 - (8/9)^{1/2}$ (Sunyaev and Shakura 1986). Thus, $L_b/L_d \simeq 6.4$ for the most compact ($R_* \simeq 1.5R_g$) NS. computations for a rotating star (Sibgatullin and Sunyaev 1998, 2000) suggest that, depending on the sense of rotation, the BL can contribute to the total accretion luminosity from 10% (when the NS and the disk corotate) to 90% (in the less likely case of their counterrotation). Most bright X-ray sources in low-mass X-ray binaries of the Galactic bulge are weakly magnetized NSs. This explains the unremitting interest in the BL structure and the incessant attempts to account for the results of X-ray observations by modeling the BL radiation spectra.

The BL at low accretion rates, $\dot{M} \lesssim 10^{-10}\ M_\odot\ \mathrm{yr}^{-1}$, has been the subject of many studies (e.g., Pringle 1977; Kluzniak 1988; Shakura and Sunyaev 1988; Paczynski 1991; Narayan and Popham 1993; Bisnovatyi-Kogan 1994). However, the first attempt to consider the problem of BL formation in the limit of large accretion rates has been made only recently (Inogamov and Sunyaev 1999). Here, the difficulty lies in the fact that at luminosities $L_b \gtrsim 0.01\ L_{\mathrm{edd}}$, where $L_{\mathrm{edd}} = 4\pi m_p GM_*c/\sigma_{\mathrm{T}} \simeq 1.38 \times 10^{38}\ (M_*/M_\odot)\ \mathrm{erg\ s}^{-1}$ is the critical Eddington luminosity, the radiation pressure in the BL begins to dominate over the gas pressure and any attempts to disregard the former, as was done by the above authors, are doomed to failure in advance. Covering a

*E-mail: sergei@hea.iki.rssi.ru

small fraction $\beta$ of the stellar surface, the BL provides a radiation flux $q_r = L_b/(4\pi\beta R_*^2)$ comparable to the local Eddington flux $q_{\rm edd} = L_{\rm edd}/4\pi R_*^2$ even at luminosity $L_b \sim \beta L_{\rm edd}$. In the solution of Shakura and Sunyaev (1988), the effective BL surface area is

$$S = 2\pi R_*\, 2H = 8\pi R_*^2 \left(\frac{R_*}{R_g}\right)^{1/2} \left(\frac{kT_e + kT_i}{m_p c^2}\right)^{1/2},$$

where $H$ is the BL half-thickness; and $T_i$ and $T_e$ are the ion and electron temperatures, respectively. For complete radiation thermalization, when $T_e \simeq T_i \simeq (q_r/\sigma)^{1/4} \simeq 2\times 10^7 (q_r/q_{\rm edd})^{1/4} m_*^{1/4} r_*^{-1/2}$ K, we have $\beta = S/(4\pi R_*^2) = 7.2 \times 10^{-3}(q_r/q_{\rm edd})^{1/8} m_*^{-3/8} r_*^{1/4}$. Here, $\sigma$ is the Stefan–Boltzmann constant, $m_* = M_*/M_\odot$, and $r_* = R_*/10$ km. Substituting more realistic temperatures, $T_e \simeq T_i \simeq 10^8$ K, cannot greatly change this result, $\beta \simeq 0.016 m_*^{-1/2} r_*^{1/2}$. The situation with the presence of a near-Eddington radiation flux is further complicated by the rotation of the material that flows into the BL at Keplerian angular velocity. As a result, the centrifugal forces in the BL prove to be comparable to the gravitational forces. Under these conditions, adding even a modest light-pressure force radically changes the entire accretion pattern.

In particular, Inogamov and Sunyaev (1999) found that at high accretion rates, the disk material has no time to appreciably decrease the angular velocity directly in the BL and begins to spirally spread over the stellar surfaces in different directions from the point of contact with the disk. The bulk of the energy is released in two bright rings located at the same large distance from the equatorial plane in which $\Omega$ falls sharply. This behavior is in stark contrast to the popular view of the BL as a natural extension of the accretion disk—a belt-shaped thickening, whose width can be determined from the hydrostatic equation and is related to appreciable energy release and, hence, a high temperature at the point of disk contact with the stellar surface.

Popham and Sunyaev (2001) attempted to save the standard pattern of accretion in the BL. They numerically modeled the deceleration of material near the NS surface in terms of conventional views of the BL but with allowance for the radiation contribution to the pressure and viscosity. These authors did not restrict their analysis to an essentially subsonic flow; i.e., they retained the terms in the hydrodynamic equations that were usually disregarded in previous studies. The emergence of radiation from the BL, in both the vertical and radial directions, was roughly taken into account.

Although two different approaches to the dynamics of the accretion flow were used in the above studies, they both predict the existence on the stellar surface of a layer of hot, rarefied, radiation-dominated plasma with an appreciable geometrical thickness and a large optical depth with an effective gravity $g_{\rm eff}$ in a spectrum formation region much lower than $g_* = GM_*/R_*^2$. In reality, $g_{\rm eff} = g_*(1 - q_r/q_{\rm edd}) - \Omega^2 R_*$; i.e., we are dealing with a layer of levitating plasma. A detailed analysis shows that advection takes place in both cases. In addition, mechanical forces transport the energy released in the BL closer to the star; i.e., the radiation flux originates in layers that are denser and deeper than the zone in which $\Omega$ and $\Omega^2$ decrease sharply (Popham and Sunyaev 2001). Because of the sign of $\partial\Omega/\partial R$, the situation in the BL is opposite to that in accretion disks, where mechanical forces remove the energy over the disk from its inner boundary outward (see Shakura and Sunyaev 1973).

Unfortunately, Inogamov and Sunyaev (1999) and Popham and Sunyaev (2001) used highly simplified approaches in analyzing radiative transfer, which did not allow them to compute the forming X-ray spectrum. The first attempt of this kind was made here. We performed detailed computations of the BL radiation spectra based on the distributions of density, temperature, and energy release computed by Popham and Sunyaev (2001) for accretion onto a NS of mass $M_* = 1.4\,M_\odot$ and radius $R_* = 10^6$ cm at three different accretion rates, $\dot{M} = 10^{-8}$, $10^{-9}$, and $10^{-10} M_\odot$ yr$^{-1}$, which correspond to BL luminosities $L_b \simeq 6\times 10^{37}$, $6\times 10^{36}$, and $6\times 10^{35}$ erg s$^{-1}$ for accretion onto a slowly rotating NS.

The subsequent presentation is organized as follows. The approaches, equations, and methods of their solution used here are detailed in Section 2. The BL radiation spectra computed for the above three accretion rates are presented in Section 3. In Section 4, we discuss the drawbacks of the approximation used by Popham and Sunyaev (2001) when analyzing radiative transfer and plasma cooling and show the importance of a consistent allowance for Comptonization and the actual frequency dependence of free-free processes. To this end, we determine the temperature distribution in the BL for the specified (derived by Popham and Sunyaev) distributions of density and energy release by solving the equation of energy balance. In conclusion, we discuss the necessity of a self-consistent solution of the dynamical and radiative transfer equations for a reliable determination of the physical parameters in the BL radiation formation region.

## 2. BASIC EQUATIONS

The radiation spectra in a hot and sufficiently rarefied plasma, which the material in the BL or in the spread layer on the NS surface is, are produced

by the combined effect of free-free processes (radiation and absorption) and Compton scattering. Both the lengthening of the photon paths via scattering (Zel'dovich and Shakura 1969; Illarionov and Sunyaev 1972a; Felten and Rees 1972; Sunyaev and Shakura 1974) and the change in photon frequency via Comptonization (Zeldovich and Sunyaev 1969; Illarionov and Sunyaev 1972b, 1974) prove to be important.

Scattering dominates in opacity: the Rosseland cross section for free-free absorption is smaller than the Thomson cross section by many orders of magnitude. The free-free processes are efficient only at sufficiently low frequencies, $\nu \ll kT_e/h$, because the free-free absorption cross section depends on frequency as $\nu^{-3}$. In this low-frequency spectral range, a Rayleigh–Jeans equilibrium is maintained, and an intense photon production takes place. Beginning with some frequency $\nu_1$, a photon has time to be scattered and to increase its frequency through the Doppler effect ($\Delta\nu/\nu \sim kT_e/m_ec^2$) before it will suffer free-free absorption. This is how the photon flux is formed upward along the frequency axis into the zone $h\nu \sim 3kT_e$, where the recoil effect comes into play. The recoil and Doppler effects combine to produce the Wien component in the plasma radiation spectrum. The behavior of Comptonization and its role in forming the spectrum and, in the long run, the production efficiency of hard photons at a given depth are largely determined by the outward photon diffusion.

In a plane-parallel case, the radiative transfer equation for the problem under consideration can be written as

$$\frac{1}{3}\frac{\partial}{\partial\tau_{\rm T}}\left(\frac{\alpha_{\rm T}}{\alpha_{\rm T}+\alpha_{\rm ff}}\frac{\partial U_\nu}{\partial\tau_{\rm T}}\right)=\frac{\alpha_{\rm ff}}{\alpha_{\rm T}}\left(U_\nu-B_\nu\right) \qquad (1)$$
$$-\frac{kT_e}{m_ec^2}x\frac{\partial}{\partial x}\left[x\frac{\partial U_\nu}{\partial x}-3U_\nu+xU_\nu\left(1+AU_\nu/x^3\right)\right],$$

where the term on the left and the first term on the right describe the spatial diffusion of photons and their free-free production and absorption, while the remaining term describes Comptonization in the nonrelativistic limit (Kompaneets 1956). The relativistic corrections to the Kompaneets operator, which we ignore here, are significant at $kT_e \gtrsim 10$ keV (see Itoh *et al.* 1998; Callinor and Lasenby 1998; Sazonov and Sunyaev 2000). We also ignore the photon production via the double Compton effect. Below, we use the following notation: $x = h\nu/kT_e$ and $A = 0.5c^2h^2/(kT_e)^3$. The quantity $U_\nu(\tau_{\rm T})$ in this equation is the angle-averaged radiation intensity at the Thomson scattering optical depth $\tau_{\rm T}$, $B_\nu(T_e)$ is the blackbody radiation intensity that corresponds to the temperature at this depth,

$$\alpha_{\rm ff} = 21.2\ N_eT_e^{-7/2}\,x^{-3}\left(1-e^{-x}\right)$$
$$\times g(x)\ {\rm K}^{7/2}{\rm cm}^5\ {\rm g}^{-1}$$

and $\alpha_{\rm T} \simeq 0.4$ cm$^2$ g$^{-1}$ are the opacities for bremsstrahlung absorption and Thomson scattering in the limit of purely hydrogen ($N_e = \rho/m_p$) plasma. The Gaunt factor $g(x)$ can be expressed in terms of the Macdonald function $K_0$

$$g(x)=\frac{\sqrt{3}}{\pi}e^{x/2}K_0\left(\frac{x}{2}\right)\simeq\begin{cases}0.55\,e^{x/2}\left[\ln(6.1/x)(1+x^2/16)-0.98\right], & \text{if } x<1.7\\ 0.55(x/2)^{-0.5}\left[1.25-(0.312-0.24/x)/x\right], & \text{if } x\geq 1.7.\end{cases}$$

The term on the right-hand side of Eq. (1) that is nonlinear in $U_\nu$ describes the induced photon scattering. This term regulates the approach of the radiation spectrum in an optically thick medium to the Planck spectrum. At $h\nu \gtrsim kT_e$, it may be disregarded, just as at $h\nu \ll kT_e$, where the formation of the Planck spectrum is determined solely by free-free processes. A solution of the problem was sought in several iterations: at the first iteration, we completely disregarded the nonlinear term in Eq. (1) and, at the subsequent iterations, we replaced it with the term $\sim U_\nu U_\nu^*$ by substituting the mean intensity $U_\nu^*$ obtained at the preceding iteration.

The boundary conditions in $\tau_{\rm T}$ for Eq. (1) were taken in the standard (for the diffusion approximation) form:

$$\left(\frac{\alpha_{\rm T}}{\alpha_{\rm T}+\alpha_{\rm ff}}\frac{\partial U_\nu}{\partial\tau_T}-\frac{3}{2}U_\nu\right)\Bigg|_{\tau_{\rm T}=0}=0 \qquad (2)$$

at the outer boundary for $\tau_{\rm T} = 0$ and

$$\left(\frac{1}{3}\frac{\partial U_\nu}{\partial\tau_T}-\frac{q_0}{4\pi}\frac{\partial B_\nu}{\partial T}\Big/\int_0^\infty\frac{\alpha_{\rm T}}{\alpha_{\rm T}+\alpha_{\rm ff}}\frac{\partial B_\nu}{\partial T}d\nu\right)\Bigg|_{\tau_{\rm T}=\tau_0}=0 \qquad (3)$$

at the inner boundary for $\tau_{\rm T} = \tau_0$. The latter condition suggests the existence of a radiation flux coming from the innermost layers, which is similar in spectral shape to the Planck flux and small in absolute value,

$$q_0 \simeq 4.5{\rm MeV}\times\frac{\dot M}{4\pi R_*^2 m_p}$$
$$\simeq 4.8\times10^{-3}\frac{\dot Mc^2}{4\pi R_*^2}\simeq 0.02\beta R_*/R_g q_r, \qquad (3')$$

where $q_r$ is the radiation flux due to accretion at the outer boundary, and $\beta$ is the ratio of the BL surface area to the area of the entire stellar surface. The effective temperature of the radiation coming from the BL depth is $kT_0 = 0.22$, 0.38, and 0.68 keV for accretion at the rates $\dot{M} = 10^{-10}$, $10^{-9}$, and $10^{-8}$ $M_\odot$ yr$^{-1}$, respectively. Such a flux must result from slow hydrogen burning at the BL base (with energy release of 4.5 MeV per nucleon of the accreted material). The above expression (3′) suggests that the accreted material subsequently spreads over the NS surface, and hydrogen burning takes place not only in the BL but also over the entire stellar surface. The soft photons supplied via this process can affect Comptonization in the hot and rarefied plasma of the outer BL.

The boundary conditions along the frequency axis were taken in the form

$$U_\nu|_{\nu=\nu_{\min}} = B_\nu(T_e), \quad (4)$$

$$\left(x\frac{\partial U_\nu}{x} - 3U_\nu + xU_\nu + AU_\nu^2/x^2\right)\Big|_{\nu=\nu_{\max}} = 0. \quad (5)$$

They imply that a local Planck (Rayleigh–Jeans) radiation spectrum is formed at energy $h\nu_{\min}$ throughout the entire (at all optical depths) BL, and that there is no photon flux along the frequency axis at energy $h\nu_{\max}$ because of Comptonization. To ensure that these conditions are properly followed, we took $h\nu_{\min} = 0.1$ eV $\ll kT_e$ and $h\nu_{\max} = 340$ keV $\gg kT_e$; i.e., we considered the problem in a wide energy range. The $\tau_{\rm T}$ breakdown was chosen to agree with $h\nu_{\min}$ so that the step in total absorption optical depth $\tau_{\rm tot} = \tau_{\rm T}(1 + \alpha_{\rm ff}/\alpha_{\rm T})$ in the outer BL did not exceed unity. For our computations, we used a quasi-logarithmic mesh with 240 points along the $\tau_{\rm T}$ axis (logarithmic at $\tau_{\rm T} \le 1$ and linear at large depths) and 200 points along the energy axis (logarithmic at $h\nu \lesssim kT_e$ and linear, with a 2.4 keV step, at high energies). This choice of the mesh provides stability of the solution, which is of considerable importance, because the coefficient of the lowest term $\sim U_\nu$ in the Kompaneets operator [see Eq. (1)] is alternating. The linearized (as described above) system of equations (1)–(5) for the specified $T_e(\tau_{\rm T})$ and $N_e(\tau_{\rm T})$ distributions can be solved by matrix sweep (the Fautrier method; see Mihalas 1978).

The need to solve a problem similar to system (1)–(5) arises when analyzing the radiation spectra of X-ray bursters if their burst luminosities approach the Eddington limit. Numerical computations for this problem were performed and described by Lapidus *et al.* (1986), London *et al.* (1986), Ebisuzaki and Nomoto (1986), Ebisuzaki (1987), and Zavlin and Shibanov (1991). These authors restricted their analyses to an exponentially falling density distribution (an exponential model atmosphere). Another important distinction between their computations and those presented here is the assumption of radiative equilibrium. As was mentioned in the Introduction, mechanical forces in the BL or in the spread layer tend to carry away the dissipating rotational kinetic energy deep into the layer. Nevertheless, most of the energy is released at a relatively small optical depth ($\tau_{\rm T} \lesssim 100$), and the radiation flux slowly rises from $q_0$ inside the BL to $q_r$ at its outer boundary. Below, when computing the BL radiation spectra, we had no need to directly use the law of energy release, because all the required information on the energy release was contained in the temperature and density distributions derived by Popham and Sunyaev (2001). At the same time, the law of energy release must be taken into account in a self-consistent analysis of radiative transfer and accretion hydrodynamics.

## 3. RADIATION SPECTRA

Our computations of the BL radiation spectra presented here are based on the distributions $kT_e(\tau_{\rm T})$ and $N_{\rm e}(\tau_{\rm T})$ shown in Figs. 6b–6d from Popham and Sunyaev (2001). These distributions correspond to the electron temperature and density in the equatorial (disk) plane. They can be directly used to determine the radiation field deep in the BL, where the radial component of the radiation flux dominates over its vertical component. However, in the outer regions, the BL density, thickness, and, as a result, vertical optical depth rapidly decrease, which gives rise to an intense vertical radiation flux. The photons escaping from the BL in this way form the source's X-ray spectrum.

All computations were performed by assuming the geometry of the problem to be one-dimensional. A plasma layer of scattering optical depth $\tau_1$ with a constant temperature and an exponentially declining density distribution was added to the outer BL edge to take into account the emergence of radiation in the vertical direction. Since Comptonization in the outer layers of a scattering medium always acts to equalize the temperature, the assumption of constant temperature is quite justifiable. We determined $kT_e$ and $\rho$ in the additional exponential atmosphere from the condition of continuity of their distributions when passing deep into the BL and the Thomson optical depth of the atmosphere $\tau_1$ from the vertical BL optical depth shown in Fig. 6a from Popham and Sunyaev (2001). We assumed that $\tau_1 = 60$, 3, and 1 for accretion at the rates $\dot{M} = 10^{-8}$, $10^{-9}$, and $10^{-10}$ $M_\odot$ yr$^{-1}$, respectively. The total Thomson scattering optical depth of the BL that was taken into account in our computations for these three cases was assumed to be $\tau_0 = 3220$, 83, and 11. The profiles of the distributions $kT_e(\tau_{\rm T})$ and $N_e(\tau_{\rm T})$ with allowance for the outer atmosphere are represented by the dotted lines

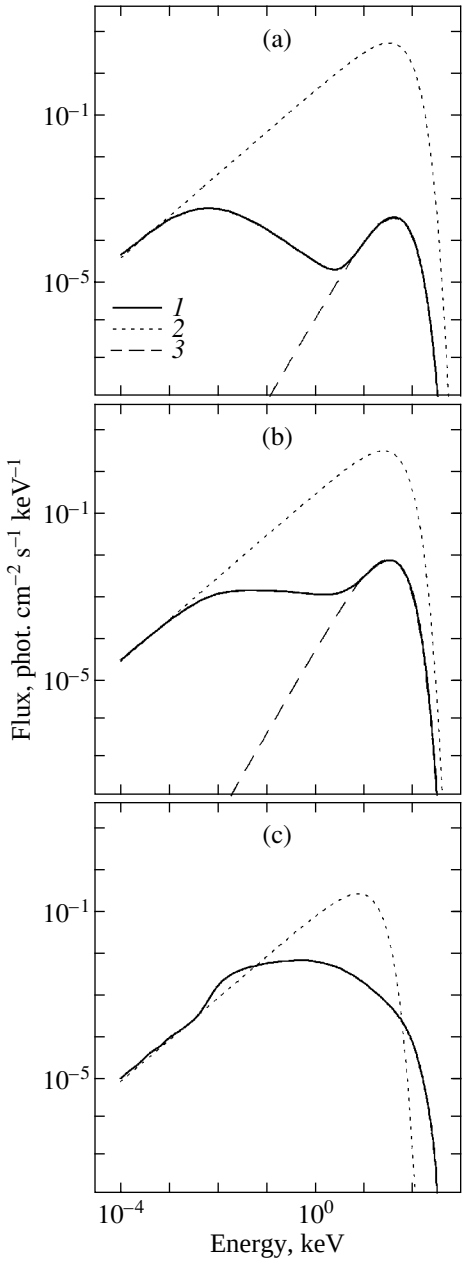


**Fig. 1.** The photon spectra (lines *1*) formed in the BL of a NS at accretion rates $\dot{M} = 10^{-8}$, $10^{-9}$, and $10^{-10}$ $M_\odot$ yr$^{-1}$ (panels a, b, and c, respectively). These accretion rates correspond to the BL luminosities $L_b = 6 \times 10^{37}$, $6 \times 10^{36}$, and $6 \times 10^{35}$ erg s$^{-1}$ for a slowly rotating NS. The gas temperature and density distributions inside the BL were taken from Popham and Sunyaev (2001). Lines *2* represent the blackbody spectra that correspond to the outer-BL temperature; lines *3* represent the Wien spectrum with the same temperature but normalized to the total emergent radiation flux from the BL.

in Fig. 5. This figure is discussed in detail in the next section.

Figure 1 shows the computed BL photon spectra (spectral flux density) $F_\nu = 2\pi U_\nu(0)/h\nu \times S/(4\pi d^2)$. Panels a, b, and c correspond to our computations for the accretion rates $\dot{M} = 10^{-8}$, $10^{-9}$, and $10^{-10}$ $M_\odot$ yr$^{-1}$. For the convenience of comparison, we assumed that the area of the radiating BL surface was everywhere equal, $S = 2\pi R_* 2H = 8\pi \times 10^{11}$ cm$^2$, where $H \sim 2 \times 10^5$ cm is the characteristic BL half-thickness. In reality, as follows from Table 2 in Popham and Sunyaev (2001), the radiating surface area strongly depends on the accretion rate; it increases by almost an order of magnitude when the accretion rate changes from $\dot{M} = 10^{-10}$ to $10^{-8}$ $M_\odot$ yr$^{-1}$. For convenience of recalculation, we assumed the binary system with the NS under study to be at the distance $d = 10$ kpc. The solid lines *1* represent the emergent radiation spectrum, and the dotted lines *2* represent the Planck spectrum that corresponds to the temperature of the outer BL. It is clearly seen from the figure (panels a and b are particularly revealing from this point of view) how profoundly Comptonization changes the spectral shape.

At low frequencies, the free-free processes definitely have time to form the Planck or, to be more precise, Rayleigh–Jeans radiation spectrum, $F_\nu \sim \nu$. Subsequently, beginning from some characteristic energy $h\nu_0 \sim 1$ eV, Compton scattering comes into play. On the one hand, because of the change in the photon trajectory, the photon mean free path in the plasma layer increases and, accordingly, the probability of their free-free absorption increases; on the other hand, because of the change in frequency (on average, by a value of the order of $kT_e/m_ec^2$ during each scattering), the photons begin to displace upward along the energy axis. These two processes appreciably reduce the observed radiation flux compared to its Planck level, resulting in a flattening of the spectrum or even in a dip at energies $h\nu_0 \lesssim h\nu \lesssim kT_e$. Having reached the energies $h\nu \sim 3kT_e$, the photons slow down their upward displacement along the energy axis because of the recoil effect. The subsequent scatterings only give rise to a distinct component with the Wien radiation spectrum, $F_\nu \sim \nu^2 \exp(-h\nu/kT_e)$. Lines *3* in Figs. 1a, 1b represent this Wien spectrum normalized to the factor $(T_{\rm eff}/T_e)^4$, where $T_{\rm eff} \simeq (q_r/\sigma)^{1/4}$ is the effective BL radiation temperature and $T_e$ is the electron temperature in the outer layers. It faithfully describes the hard part of the computed spectrum. To illustrate the formation of the radiation spectrum inside the BL, in Fig. 2 for $\dot{M} = 10^{-8}$ $M_\odot$ yr$^{-1}$, we show a sequence of the spectra $F_\nu(\tau_{\rm T}) = \pi U_\nu(\tau_{\rm T})/h\nu \times S/(4\pi d^2)$ taken at various optical depths, $\tau_{\rm T} = 0$, 5, 20, 60, 150, 170, 190, 250, 1000, and 3220. The figure shows how rapidly the deviations of the spectral shape from

the Planck law increase when passing from the inner plasma layers to the outer layers. At the same time, we see that the spectral shape follows the variations in plasma temperature with optical depth, in particular, in the Rayleigh–Jeans part of the spectrum, $kT_e = U_\nu c^2/2h\nu^2$.

The Comptonization described above was first considered by Zeldovich and Sunyaev (1969) and Sunyaev and Zeldovich (1970) (see also Illarionov and Sunyaev 1974) as applied to the formation of distortions in the cosmic-microwave-background (CMB) radiation spectrum in the early Universe. This problem has much in common with our problem. There are also a number of serious differences, with the most important of them being the finite BL volume and the existence of a BL boundary, as well as the nonuniform temperature, density, and energy release distributions inside the BL. In particular, the purely diffusion processes (scattering without any change in frequency) are much less important in the early Universe. The BL radiation spectrum computed for accretion at the rate $\dot{M} = 10^{-10}\ M_\odot\ \mathrm{yr}^{-1}$, which is shown in Fig. 1c (see also Fig. 4c), clearly illustrates how important these differences are. In this case, the BL has a comparatively small scattering optical depth, $\tau_0 = 11$. Therefore, the observed spectrum is a complex combination of the radiation spectra that originate from regions with different temperatures and densities and that were affected by Comptonization to different degrees. Note that the radiation-scattering and reflecting NS surface and atmosphere lie under the BL. Consequently, at such a small optical depth, the emergent radiation spectrum could be additionally distorted. Taking this possibility into account, we performed yet another model computation by assuming that there was a layer of plasma with a constant temperature (the same as that at the BL base) with an exponentially increasing density and Thomson scattering optical depth $\tau_2 = 90$ beneath the layer with $\tau_0 = 11$. The radiation spectrum computed for this model is shown in Fig. 3 in comparison with the radiation spectrum of the upper layer. We see that there are actually differences between the spectra but they are not very large.

Qualitatively, if not quantitatively, the radiation spectrum for accretion at the rate $\dot{M} = 10^{-10}\ M_\odot\ \mathrm{yr}^{-1}$ most closely matches the hard spectra observed for low-state X-ray bursters (Barret and Vedrenne 1994; Pavlinsky *et al.* 1995; Churazov *et al.* 1997; Barret *et al.* 2000). In general, however, an analysis of Fig. 1 indicates that the BL radiation spectra computed in terms of the model by Popham and Sunyaev (2001) differ radically from the X-ray spectra that are actually observed for weakly magnetized accreting NSs (White *et al.* 1988; Pavlinsky *et al.* 1994). This is particularly clearly seen in Fig. 4, where the computed spectra are shown only in the X-ray energy band in comparison with the measured spectra of several known X-ray sources. At high luminosities, the computed X-ray spectra have the Wien shape with characteristic temperatures $kT_r \sim 15$ keV (for $\dot{M} = 10^{-9}\ M_\odot\ \mathrm{yr}^{-1}$) and $kT_r \sim 20$ keV (for $\dot{M} = 10^{-8}\ M_\odot\ \mathrm{yr}^{-1}$), which reflect the high plasma temperatures in the outer BL obtained by Popham and Sunyaev (2001). The observed spectra are flatter and are best described by the radiation spectrum of optically thin plasma with a temperature $kT_{br} \sim 6$ keV; an attempt to fit them by the Planck or Wien laws yields radiation temperatures $kT_r \sim 2$–3 keV.

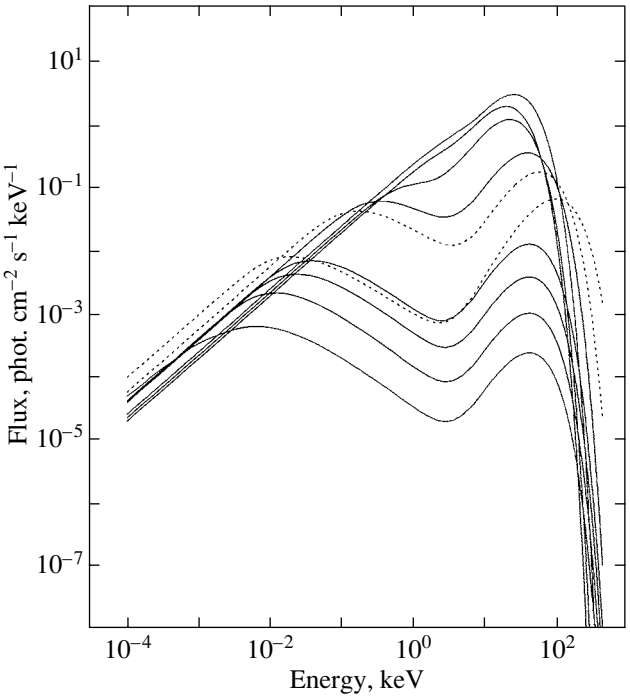


**Fig. 2.** The photon spectra at various optical depths (the spectra from bottom to top correspond to $\tau_\mathrm{T} = 0$, 5, 20, 60, 150, 170, 190, 250, 1000, and 3220) in the BL of a NS star for accretion at the rate $\dot{M} = 10^{-8}\ M_\odot\ \mathrm{yr}^{-1}$. We see how the spectrum evolves from the Planck spectrum at large optical depths to the observed spectrum ($\tau_\mathrm{T} = 0$), which is highly diluted via Comptonization, with an intense Wien component in the hard energy band. The dotted lines indicate the spectra formed in the layer of hot plasma at optical depths $\tau_\mathrm{T} = 150$–170.

## 4. TEMPERATURE DISTRIBUTION

The high BL temperatures that follow from the computations by Popham and Sunyaev (2001) can be attributed to their oversimplified treatment of radiative

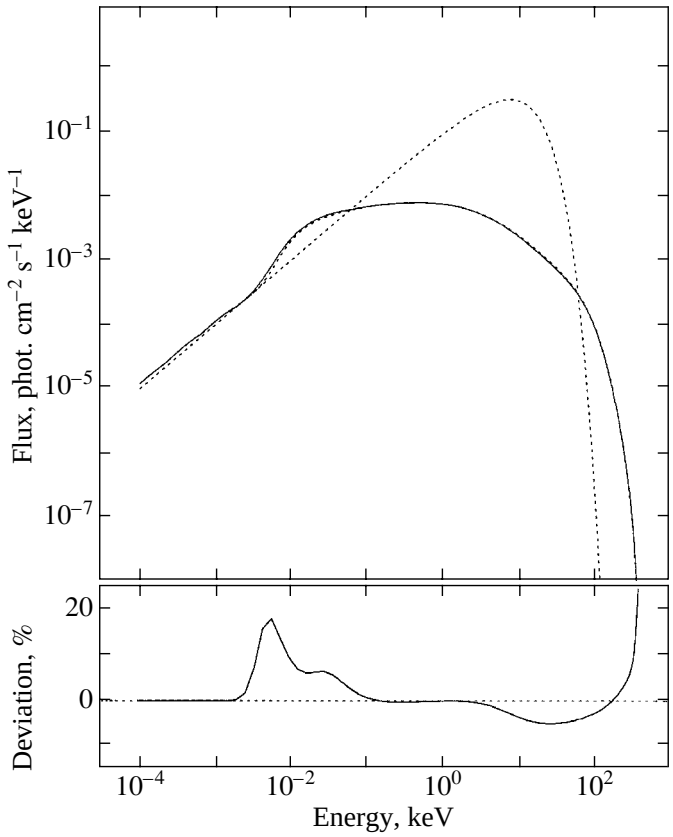


**Fig. 3.** The radiation spectrum for the BL of a NS for accretion at the rate $\dot{M} = 10^{-10}\ M_\odot\ \mathrm{yr}^{-1}$ computed with allowance for scattering and absorption in the upper NS atmospheric layers ($\tau_2 \sim 90$), the atmospheric temperature and density were assumed to be constant and equal to those at the BL base. The discrepancy between this spectrum and the BL radiation spectrum computed without direct allowance for the interaction with the atmosphere using the boundary condition specified by Eq. (3) is shown in the bottom panel. As in Fig. 1, the dotted line shows the blackbody spectrum corresponding to the temperature of the outer BL.

transfer and thermal balance in plasma. They completely disregarded the frequency dependence of the radiation intensity and used an average Kramer opacity for free-free absorption, $\alpha_{\mathrm{ff}} = 3.9\rho T^{-7/2}\ \mathrm{cm}^2\ \mathrm{g}^{-1}$ [see Popham and Narayan (1995) for more details]. In contrast to Popham and Narayan, an attempt was made to take into account Comptonization. It reduced to introducing an appropriate "amplification" correction $\sim(4kT_e - \langle h\nu\rangle)/m_ec^2$ for the mean radiation intensity in each scattering. The equation of radiative transfer itself was solved in the so-called four-steam approximation. This approach is totally at variance with the formation pattern of the BL radiation described in the preceding section, in which the free-free photons produced in the low-frequency spectral range via Comptonization increase their energy to $\sim 3kT_e$. As a result, the actual increase in the energy losses via Comptonization compared to the free-free losses reaches $w_{\mathrm{c}}/w_{\mathrm{ff}} = 0.75\ln^2(2.35kT_e/h\nu_0) \sim 100$ (Illarionov and Sunyaev 1974), which appreciably exceeds the correction used by Popham and Sunyaev (2001).

To find out how the simplified treatment of radiative transfer and Comptonization affects the results of our BL-structure computations, we attempted to determine the temperature distribution inside the BL that agreed with the distributions of plasma density $N_e(\tau_{\mathrm{T}})$ and viscous energy release $Q(\tau_{\mathrm{T}})$ [erg g$^{-1}$ s$^{-1}$] derived by Popham and Sunyaev (2001) and that simultaneously satisfied the solution of system (1)–(5). In the equation of energy balance

$$\rho Q = 2\frac{q_v}{H} - \frac{\partial q_r}{\partial R} + \rho v_r T\frac{\partial S}{\partial R}, \qquad (6)$$

we ignored the escape of radiation in the vertical direction (the first term on the right), except for the radially outermost layers where all of the radiation goes in the vertical direction (to take into account this vertical flux, we introduced an additional plasma layer of optical depth $\tau_1$; see Section 4). This simplification is apparently the reason why the radial radiation

flux emerging from the layer for $\dot{M} = 10^{-8}\ M_\odot\ \mathrm{yr}^{-1}$ proved to be slightly higher than its Eddington value. When solving Eq. (6), we also ignored the advection of thermal energy of the matter and the radiation locked in it, the third term on the right (in this equation, $T\partial S$ means the change both in electron and ion entropy components and in the radiation-related component). Advection is important only in the outer BL, where it acts as a cooling mechanism: part of the released energy is carried away through advection into deeper layers. Allowance for advection can apparently cause an even larger reduction of the temperature in the outer layers than that found (see below) in our computations for $\dot{M} = 10^{-9}$ and $10^{-10}\ M_\odot\ \mathrm{yr}^{-1}$ and can result in a partial compensation for the increase in temperature found for $\dot{M} = 10^{-8}\ M_\odot\ \mathrm{yr}^{-1}$. At a high accretion rate, advection is clearly of particular importance.

We determined the term in Eq. (6) related to the increase in radial flux $q_r$ from Eq. (1) after its frequency integration:

$$\frac{1}{4\pi}\frac{\partial q_r}{\partial \tau_\mathrm{T}} = \int \frac{\alpha_\mathrm{ff}}{\alpha_\mathrm{T}}\left[U_\nu - B_\nu(T_e)\right] dx \qquad (7)$$
$$- \frac{kT_e}{m_e c^2}\int \left(4 - x - A\frac{U_\nu}{x^2}\right) U_\nu dx.$$

On the right-hand side of Eq. (7) derived in this way, the first term describes the free-free energy losses by plasma and the second term describes the energy loss or gain through Compton heating and cooling (see Levich and Sunyaev 1971). We see from Eq. (7) that if the radiation spectrum differs greatly from the Planck spectrum, then the free-free losses become substantial and the use of average opacities to estimate the mean intensity is not valid. Note that although the designation $\partial/\partial R$ for the derivative with respect to the radius in the disk plane is retained in Eq. (6), the BL was actually assumed to be geometrically thin; i.e., we considered a plane-parallel problem. The spectra shown in Figs. 1–4 also refer to the radial flux $q = q_r$ alone.

We solved the system of nonlinear algebraic equations (6) and (7) for $kT_e(\tau_\mathrm{T})$ by the secant method. In the upper panels of Fig. 5, lines *1* indicate the temperature distributions $T_e(\tau_\mathrm{T})$ obtained by using this procedure for three BL models with different accretion rates, (Fig. 5a) $\dot{M} = 10^{-8}$, (Fig. 5b) $10^{-9}$, and (Fig. 5c) $10^{-10}\ M_\odot\ \mathrm{yr}^{-1}$. For the optically thick case, $\dot{M} = 10^{-8}\ M_\odot\ \mathrm{yr}^{-1}$, the temperature distribution was sought only in the outer layer at optical depth $\tau_\mathrm{T} \le 170$. In this case, the flux $q_0$ in the boundary condition (3) was corrected for the contribution of the radiation from deeper layers:

$$q_0' = q_0 + \int_{170}^{\infty} d\,\tau_\mathrm{T} Q/\alpha_\mathrm{T}.$$

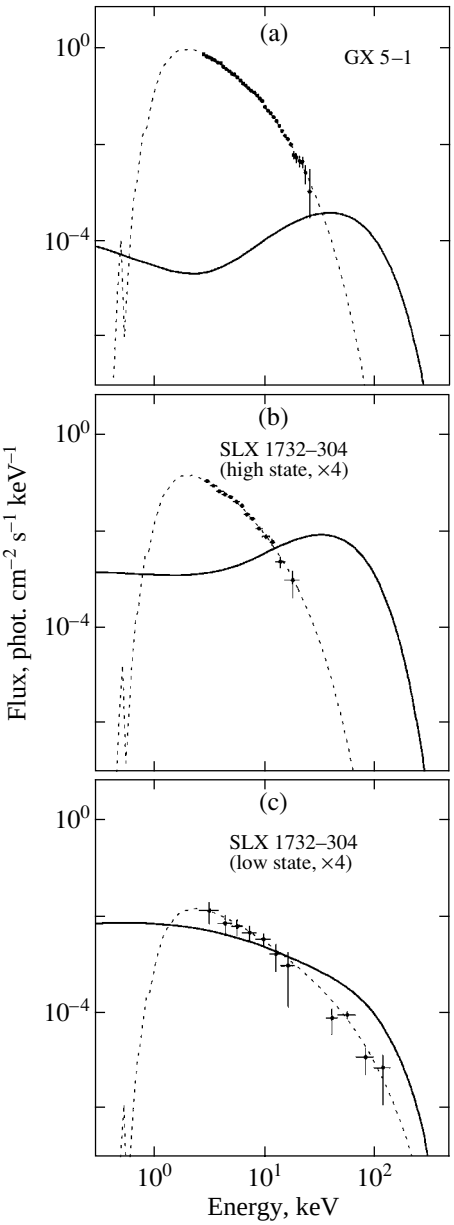


**Fig. 4.** The same spectra as in Fig. 1 shown only in X-ray and gamma-ray energy bands in comparison with the measured spectra of bright X-ray sources, GX 5–1 and SLX 1732–304 (as observed with the Granat observatory; see Grebenev *et al.* 1996; Pavlinsky *et al.* 1995). SLX 1732–304 was observed in high and low states. Given that SLX 1732–304 is in the globular cluster Terzan 1 at a distance $d \simeq 5$ kpc, we increased the normalization of its spectrum by a factor of 4. The dotted lines represent the best fit to the measured spectra by the free-free model of optically thin plasma ($kT_{br} = 7$, 6.1, and 33 keV for panels a, b, and c, respectively).

We restricted ourselves to this computation, because the radiation emerging from the BL originates at comparatively small optical depths that are definitely less than $\tau_\mathrm{T} = 170$, and because computing the temperature field in deeper layers would entail an overly

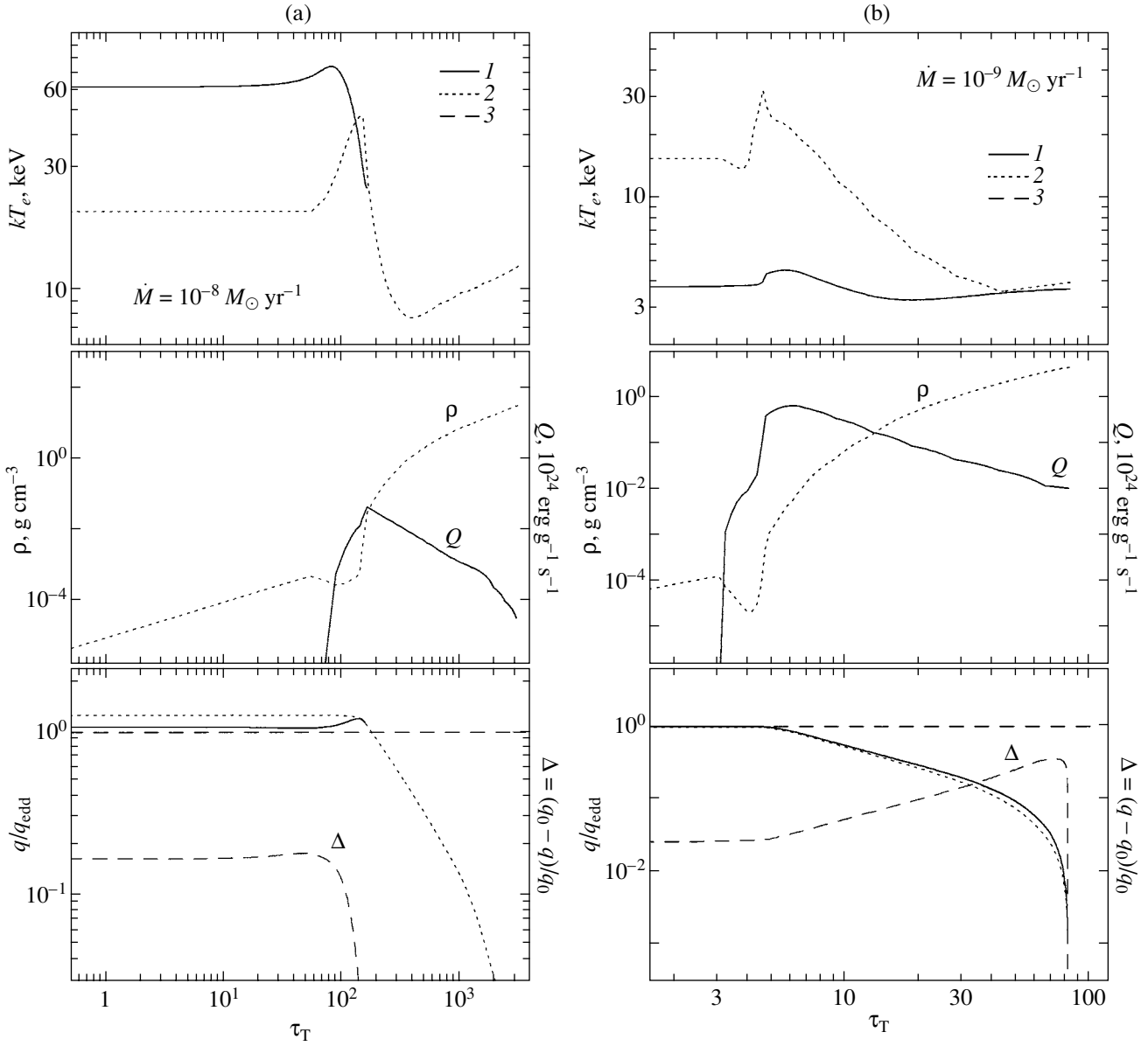


**Fig. 5.** The distributions of temperature $kT_e$, density $\rho$, and energy release $Q$ inside the BL, as well as the corresponding variation in radiation flux $q$ versus Thomson scattering optical depth $\tau_{\mathrm{T}}$ for accretion at the rates $\dot{M} = 10^{-8}$, $10^{-9}$, and $10^{-10}\ M_\odot\ \mathrm{yr}^{-1}$ (panels a, b, and c, respectively). Lines *2* in the upper panels represent the temperature distribution derived by Popham and Sunyaev (2001); line *1* represents the distribution computed here; and line *3* in the lower panels represents the discrepancy (residual) $\Delta = (q - q_*)/q_*$ between the computed flux $q$ and the flux $q_*$ that follows from the distribution of energy release $Q$ inside the BL.

large expenditure of computer time. Note that for this computation, the upper boundary of the energy grid was displaced to $h\nu_{\max} = 570$ keV.

Lines *2* in the upper panels of Fig. 5 indicate the original temperature distributions taken from Popham and Sunyaev (2001). In the other panels, density $\rho$, energy release $Q$, and radiation flux $q$ are plotted against $\tau_{\mathrm{T}}$. The quantity $\Delta = |q - q_*|/q_*$ characterizes the quality of our computation; it gives the deviation of the computed flux $q$ at various optical depths (line *1* in the bottom panels) from $q_*$ (line *2*) that follows from the law of energy release. The deviations nowhere exceed 15%. The fluxes $q$ and $q_*$ in this figure are dimensionless and normalized to the Eddington flux $q_{\mathrm{edd}} = 0.5 m_p c^3 R_g / R_*^2 \sigma_{\mathrm{T}} \simeq 1.54 \times 10^{25}$ erg cm$^{-2}$ s$^{-1}$ (for a star of mass $M_* = 1.4 M_\odot$). As was already noted above, at the maximum accretion rate $\dot{M} = 10^{-8}\ M_\odot\ \mathrm{yr}^{-1}$, the value of this quantity slightly exceeds unity, which apparently

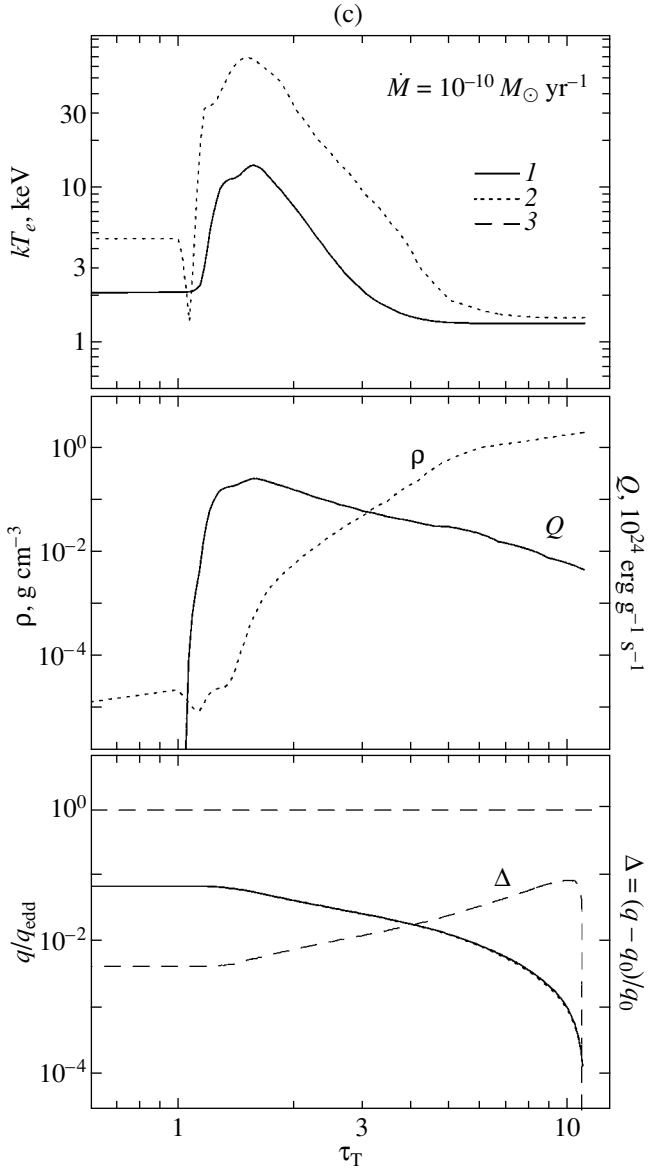


**Fig. 5.** (Contd.)

results from the escape of part of the radiation in the vertical direction being disregarded.

We see from the figure that the temperature distributions computed with allowance for the actual frequency dependence of the free-free emissivity and opacity differ greatly from those derived by Popham and Sunyaev (2001). In particular, for accretion at the rates $\dot{M} = 10^{-9}$ and $10^{-10}\ M_\odot\ \mathrm{yr}^{-1}$, the BL temperature is appreciably lower than the temperature in the Popham–Sunyaev solution and its distribution is much flatter and smoother. By contrast, for accretion at the rate $\dot{M} = 10^{-8}\ M_\odot\ \mathrm{yr}^{-1}$, the computed BL temperature is higher than that found by Popham and Sunyaev.

Recall that under typical conditions of radiation diffusion in an optically thick medium, when the local radiation spectra do not differ much from the Planck spectrum, there must be no abrupt changes and jumps in plasma temperature at all. In such a medium, the temperature decreases outward as $T \sim T_{\mathrm{eff}}[3/4(\tau + 2/3)]^{1/4}$ in the limit of a constant density and in the presence of radiative equilibrium (Mihalas 1978). Clearly, energy release can only slow down this decrease without causing any rise in temperature outward. A negative temperature gradient under these conditions would imply that the radiation flux goes in the opposite direction, into the layer. The temperature can rise only in the outer regions of the plasma layer, in the region of sharp decrease in density

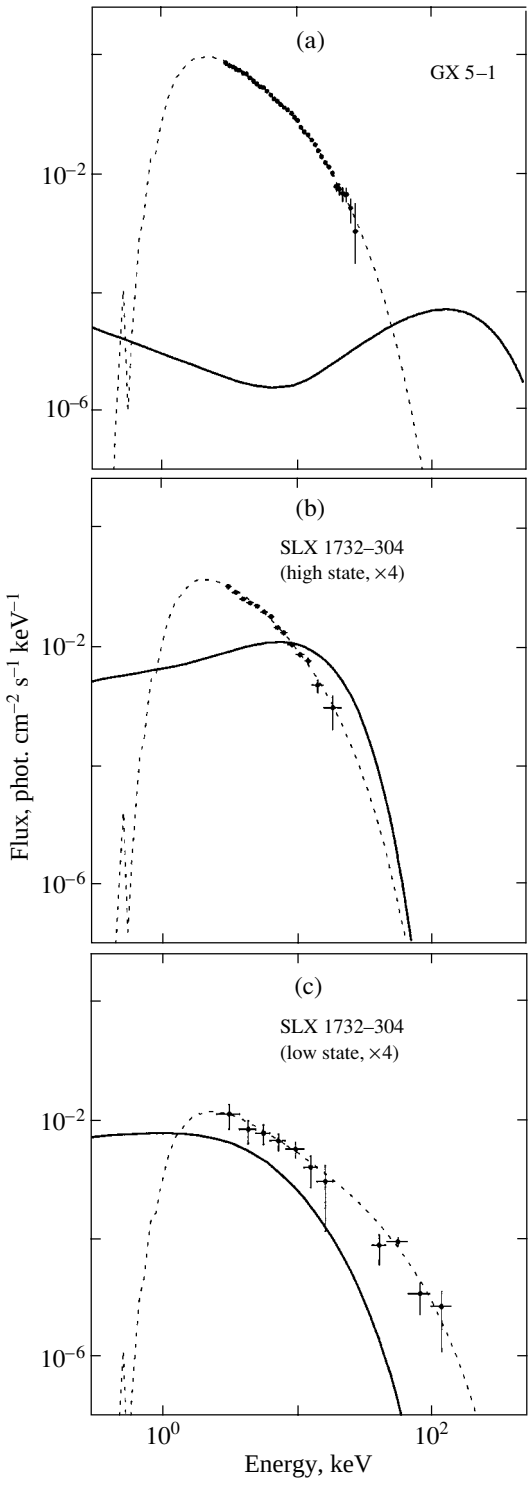


**Fig. 6.** The same spectra as in Fig. 4 computed with allowance for the temperature distribution inside the BL $kT_e$ derived here.

and at a comparatively small optical depth, where the spectrum significantly differs from the Planck spectrum, and where the Comptonization is efficient. Even earlier computations for X-ray bursts with near-Eddington luminosities (Lapidus *et al.* 1986; London *et al.* 1986; Ebisuzaki and Nomoto 1986; Ebisuzaki 1987; Zavlin and Shibanov 1991) showed that, in the outer atmospheric layers of bursters, the temperature tends to a constant level that exceeds the effective temperature. Any energy release inside this layer must cause a further rise in $kT_e$.

The efficiency with which low-frequency photons are pumped into the Wien tail through Comptonization is determined by the condition

$$y_{\rm C} \gtrsim \ln(3kT_e/h\nu_0) \qquad (8)$$

(Illarionov and Sunyaev 1974). Here, $y_{\rm C} = 4kT_e/m_ec^2\tau_{\rm T}^2$ is the Comptonization parameter (dimensionless time), and $h\nu_0$ is the characteristic frequency that was first introduced by Kompaneets (1956) beginning from which the rate of the Compton process (the upward photon displacement along the energy axis) becomes larger than the rate of free-free absorption. From the condition

$$\alpha_{\rm ff} = \frac{4kT_e}{m_ec^2}\alpha_{\rm T},$$

we derive

$$h\nu_0 \simeq 1.6\left(\frac{kT_e}{10\ {\rm keV}}\right)^{-9/4}\left(\frac{\rho}{10^{-4}\ {\rm g\,cm^{-3}}}\right)^{1/2} \times g(x)^{1/2}\ {\rm eV}.$$

Large deviations from the Planck spectrum are possible only for sufficiently rarefied ($\rho \lesssim 10^{-4}$ g cm$^{-3}$), hot ($kT_e \sim 10$ keV) plasma. In the BL, such conditions exist only in its outermost regions, in the zone of sharp decrease in density that takes place (see Fig. 5) at optical depths $\tau_2 \simeq 160$, 4.5, and 1.5 for accretion at the rates $\dot{M} = 10^{-8}$, $10^{-9}$, and $10^{-10}$ $M_\odot$ yr$^{-1}$, respectively. This Thomson optical depth should be used to estimate the Comptonization parameter $y_{\rm C}$. It follows from inequality (8) that the Comptonization is efficient if $\tau_{\rm T} \gtrsim 11(kT_e/10\ {\rm keV})^{-1/2}$. For simplicity, we omitted here the weak logarithmic dependence of the derived value on $kT_e$ and $\rho$. A comparison with $\tau_2$ accounts for the above computed temperature distribution in the BL. For $\dot{M} = 10^{-9}$ and $10^{-10}$ $M_\odot$ yr$^{-1}$, the Comptonization is only of moderate importance in forming the radiation spectrum, and the outer BL regions warm up only slightly. For accretion at the rate $\dot{M} = 10^{-8}$ $M_\odot$ yr$^{-1}$, the Comptonization is saturated; i.e., an intense Wien component with a temperature that is much higher than the effective temperature is formed in the radiation spectrum. This radiation heats up the electrons in the outer BL to the radiation temperature. Note that advection can play a role in displacing the hot plasma region toward larger optical depths.

## CONCLUSIONS

Our computations suggest that, for accretion onto a neutron star at the rates $\dot{M} = 10^{-8}$, $10^{-9}$, and $10^{-10}$ $M_\odot$ yr$^{-1}$, the temperature in the outer BL is 62, 3.8, and 2.1 keV, respectively. These values differ greatly from those obtained by Popham and Sunyaev (2001). The effective radiation temperature for these three cases is 2.10, 1.96, and 1.02 keV. For accretion at the rates $\dot{M} = 10^{-9}$ and $10^{-10}$ $M_\odot$ yr$^{-1}$, the emergent radiation spectrum becomes softer as the temperature decreases. Figure 6 shows the photon spectra computed for the same three accretion rates as the spectra in Fig. 4 but with allowance for a self-consistent temperature distribution in the BL. For convenience of comparison, we retained in this figure the experimental data points for X-ray sources shown in Fig. 4. We see that the newly obtained spectra for accretion at the rates $\dot{M} = 10^{-9}$ and $10^{-10}$ $M_\odot$ yr$^{-1}$ describe the observational data much better than do the initial spectra that are directly based on the BL-structure computations performed by Popham and Sunyaev (2001). The radiation spectrum for the maximum accretion rate $\dot{M} = 10^{-8}$ $M_\odot$ yr$^{-1}$ proves to be very hard, in stark contrast to the spectra of actually observed sources with comparable X-ray luminosities.

It should be emphasized that our computations of the temperature distribution are more likely a demonstration, showing the importance of allowing for actual radiative transfer in the BL including Comptonization. They are not self-consistent, because any change in temperature must inevitably affect the pressure and density profiles inside the BL, the accretion dynamics, and, as a result, the law of energy release. We assumed all these distributions to be fixed and completely disregarded advection. We will attempt to find a self-consistent solution of this complex problem in subsequent papers. On the other hand, the large discrepancy between the observed and computed X-ray spectra for accretion at the rate $\dot{M} = 10^{-8}$ $M_\odot$ yr$^{-1}$ may suggest much more serious drawbacks of the approach to analyzing the BL structure described by Popham and Sunyaev (2001). In particular, accretion onto a neutron star at such high rates can proceed according to the scenario proposed by Inogamov and Sunyaev (1999) without the formation of a classical boundary layer.

## ACKNOWLEDGMENTS

This study was supported by the Russian Foundation for Basic Research (project no. 99-02-18178), the Ministry of Industry and Science of Russia (grants of the Russian President nos. 00-15-99297 and 00-15-96649), and the Program "Astronomy: Nonstationary Astronomical Objects" of the Russian Academy of Sciences.

## REFERENCES

1. D. Barret and G. Vedrenne, Astrophys. J., Suppl. Ser. **92**, 505 (1994).
2. D. Barret, J. F. Olive, L. Oirin, *et al.*, Astrophys. J. **533**, 329 (2000).
3. G. S. Bisnovatyi-Kogan, Mon. Not. R. Astron. Soc. **269**, 557 (1994).
4. A. Callinor and A. Lasenby, Astrophys. J. **499**, 1 (1998).
5. E. Churazov, M. Gilfanov, R. Sunyaev, *et al.*, Adv. Space Res. **19** (1), 55 (1997).
6. T. Ebisuzaki, Publ. Astron. Soc. Jpn. **39**, 539 (1987).
7. T. Ebisuzaki and K. Nomoto, Astrophys. J. Lett. **305**, L67 (1986).
8. J. E. Felten and M. J. Rees, Astron. Astrophys. J. **17**, 226 (1972).
9. S. A. Grebenev, M. N. Pavlinsky, and R. A. Sunyaev, in *Proceedings of 2nd INTEGRAL Workshop "The Transparent Universe,"* Ed. by C. Winkler, T. J.-L. Courvoisier, and Ph. Durouchoux, ESA SP **382**, 183 (1996).
10. A. F. Illarionov and R. A. Sunyaev, Astrophys. Space Sci. **19**, 61 (1972a).
11. A. F. Illarionov and R. A. Sunyaev, Astron. Zh. **49**, 58 (1972b) [Sov. Astron. **16**, 45 (1972b)].
12. A. F. Illarionov and R. A. Sunyaev, Astron. Zh. **51**, 698 (1974) [Sov. Astron. **18**, 413 (1974)].
13. N. A. Inogamov and R. A. Sunyaev, Pis'ma Astron. Zh. **25**, 323 (1999) [Astron. Lett. **25**, 269 (1999)].
14. N. Itoh, Y. Kohyama, and S. Nozawa, Astrophys. J. **502**, 7 (1998).
15. W. Kluzhniak, PhD Thesis (Stanford University, 1988).
16. A. S. Kompaneets, Zh. Éksp. Teor. Fiz. **31**, 876 (1956) [Sov. Phys. JETP **4**, 730 (1957)].
17. I. I. Lapidus, R. A. Sunyaev, and L. G. Titarchuk, Pis'ma Astron. Zh. **12**, 918 (1986) [Sov. Astron. Lett. **12**, 383 (1986)].
18. E. V. Levich and R. A. Sunyaev, Astron. Zh. **48**, 461 (1971) [Sov. Astron. **15**, 363 (1971)].
19. R. A. London, R. E. Taam, and W. M. Howard, Astrophys. J. **306**, 170 (1986).
20. D. Mihalas, *Stellar Atmospheres* (Freeman, San Francisco, 1978; Mir, Moscow, 1982).
21. R. Narayan and R. Popham, Nature **362**, 820 (1993).
22. B. Paczynski, Astrophys. J. **370**, 597 (1991).
23. M. Pavlinsky, S. Grebenev, and R. Sunyaev, Astrophys. J. **425**, 110 (1994).
24. M. Pavlinsky, S. Grebenev, A. Finogenov, and R. Sunyaev, Adv. Space Res. **16** (3), 95 (1995).
25. R. Popham and R. Narayan, Astrophys. J. **442**, 337 (1995).
26. R. Popham and R. Sunyaev, Astrophys. J. **547**, 355 (2001).
27. J. E. Pringle, Mon. Not. R. Astron. Soc. **178**, 195 (1977).

28. S. Y. Sazonov and R. A. Sunyaev, Astrophys. J. **543**, 28 (2000).
29. N. I. Shakura and R. A. Sunyaev, Astron. Astrophys. **24**, 337 (1973).
30. N. I. Shakura and R. A. Sunyaev, Adv. Space Res. **8** (2), 135 (1988).
31. N. R. Sibgatullin and R. A. Sunyaev, Pis'ma Astron. Zh. **24**, 894 (1998) [Astron. Lett. **24**, 774 (1998)].
32. N. R. Sibgatullin and R. A. Sunyaev, Pis'ma Astron. Zh. **26**, 813 (2000) [Astron. Lett. **26**, 699 (2000)].
33. R. A. Sunyaev and Ya. B. Zeldovich, Astrophys. Space Sci. **7**, 20 (1970).
34. R. A. Sunyaev and N. I. Shakura, Astron. Zh. **51**, 102 (1974) [Sov. Astron. **18**, 60 (1974)].
35. R. A. Sunyaev and N. I. Shakura, Pis'ma Astron. Zh. **12**, 286 (1986) [Sov. Astron. Lett. **12**, 117 (1986)].
36. N. E. White, L. Stella, and A. N. Parmar, Astrophys. J. **324**, 363 (1988).
37. V. E. Zavlin and Yu. A. Shibanov, Astron. Zh. **68**, 999 (1991) [Sov. Astron. **35**, 499 (1991)].
38. Ya. B. Zel'dovich and N. I. Shakura, Astron. Zh. **46**, 225 (1969) [Sov. Astron. **13**, 175 (1969)].
39. Ya. B. Zeldovich and R. A. Sunyaev, Astrophys. Space Sci. **4**, 301 (1969).

*Translated by V. Astakhov*

*Astronomy Letters, Vol. 28, No. 3, 2002, pp. 163–168. Translated from Pis'ma v Astronomicheskiĭ Zhurnal, Vol. 28, No. 3, 2002, pp. 189–194.*


# Comparison of Stellar Orbits in Various Models of the Galaxy

**S. Ninković[1], V. V. Orlov[2,*], and A. V. Petrova[2]**

[1] *Belgrade Observatory, Belgrade, Yugoslavia*
[2] *Astronomical Institute, St. Petersburg State University, Bibliotechnaya pl. 2, Petrodvorets, 198904 Russia*

Received September 20, 2001

**Abstract**—We compare the properties of orbits in five different rotationally symmetric models of the regular Galactic force field. Our goal is to estimate the possible range of the discrepancies in stellar orbital elements attributable to the choice of the model for the Galactic potential. For disk objects, the discrepancies in eccentricities $e$ attributable to the choice of the model do not exceed 0.05. The relative distances $h$ from the symmetry plane can differ by more than a factor of 2. Since there are resonance regions, the types of orbits (box-shaped or tube-shaped) cannot be reliably identified. The situation is even worse for halo objects: the discrepancies in $h$ can exceed 100%, and identifying the type of orbits is also highly problematic.


Key words: *theoretical and observational cosmology; Galaxy (Milky Way)*

## INTRODUCTION

The study of the orbits of various objects in the regular Galactic field is of interest in solving many kinematical and dynamical problems of the Galaxy. Different authors use different expressions for the Galactic potential, which are usually derived from analytic fits to some observed relationships.

Two approaches can be used to construct models of the regular Galactic field. The first approach is based on the fitting of the observed star density distribution in the solar neighborhood and the subsequent solution of the Poisson equation to find an analytic or numerical representation of the Galactic potential. The second approach uses some form of the Galactic potential that depends on several parameters. The parameters are estimated from observational data, which usually include the Galactic rotation curve, the solar-motion parameters, and the dependence of the vertical force component on the distance to the Galactic plane in the solar neighborhood.

The Galactic-potential models generally consist of several components (nucleus, halo, disk, corona, etc.). Since the number of parameters is large (typically more than ten), the potentials of different models are difficult to compare directly. On the other hand, the orbital shapes and elements for the same objects can be compared in different Galactic models. Here, we perform such a comparison for five different models of the Galactic potential.

*E-mail: vor@astro.spbu.ru

Section 1 describes the models used and the technique of numerical experiments. Sections 2 and 3 present the results of our comparison for specific stars and for model objects, respectively. These results are discussed in Section 4.

## 1. MODELS AND TECHNIQUE

We consider orbits for the following five models of the Galactic potential:

(1) The model by Allen and Martos (1986) (below referred to as AM);

(2) The model by Carlberg and Innanen (1987) (CI);

(3) The model by Kutuzov and Osipkov (1989) (KO);

(4) The model by Miyamoto *et al.* (1980) (MSO);

(5) The model by Ninković (1992a) (N).

For all these models, we calculated the right-hand sides of the equations of motion in the meridional plane $(R, z)$, where $R$ is the distance from the Galactic rotation axis, and $|z|$ is the distance from the Galactic symmetry plane. All the models considered here have an axis and plane of symmetry.

The equations of motion in the meridional plane $(R, z)$ were numerically integrated up to $t = 1 \times 10^{10}$ yr. The calculations were checked by the conservation of the energy integral. The relative errors of this integral did not exceed $10^{-8}$ at the end of the calculation. In our calculations, we used the following system of units:

Orbital parameters of stars

| Star name | Orbital elements | Model | | | | |
|---|---|---|---|---|---|---|
| | | AM | CI | KO | MSO | N |
| Sun | $R_m$, $R_0$ | 1.012 | 1.009 | 1.011 | 1.010 | 1.029 |
| | $e$ | 0.036 | 0.031 | 0.033 | 0.030 | 0.043 |
| | $h$ | 0.0094 | 0.0093 | 0.0020 | 0.0052 | 0.0126 |
| | Type of orbit | Box | Box | Box | Box | Box |
| Gliese 1 | $R_m$ | 0.724 | 0.731 | 0.727 | 0.742 | 0.720 |
| | $e$ | 0.491 | 0.464 | 0.477 | 0.431 | 0.489 |
| | $h$ | 0.0621 | 0.0756 | 0.0452 | 0.0350 | 0.0817 |
| | Type of orbit | Box | Box | Box | Box | Box |
| Gliese 445 | $R_m$ | 0.878 | 0.882 | 0.872 | 0.870 | 0.876 |
| | $e$ | 0.324 | 0.333 | 0.317 | 0.287 | 0.329 |
| | $h$ | 0.202 | 0.173 | 0.184 | 0.115 | 0.228 |
| | Type of orbit | Box | Tube | Box | Box | Box |

(1) unit of mass—$10^9 M_\odot$;

(2) unit of time—$10^8$ yr;

(3) unit of distance—1 kpc.

In this system of units, the gravitational constant is $G = 45.02$ and the unit of velocity is 9.778 km s$^{-1}$.

We considered all motions in the Galactocentric coordinate system. The initial velocities $(U, V, W)$ are directed toward the Galactic center, $(l = 0°, b = 0°)$; along the Galactic rotation, $(l = 90°, b = 0°)$; and toward the Galactic north pole $(b = 90°)$.

## 2. THE ORBITS OF SPECIFIC STARS

We chose the initial conditions for specific stars with allowance for the solar motion relative to the Galactic center. The Galactocentric velocity of the Sun consists of the local circular velocity, the residual motion of the local centroid with respect to the circular velocity, and the residual motion in the local centroid system. The local circular velocity is given for each of the models considered. The other two components are assumed to be constant and independent of the adopted model.

A number of studies have been published in recent years (Chen 1997; Metzger *et al.* 1998; Miyamoto and Zhu 1998; Dehnen and Binney 1998; Reid 1998; Feast 2000; Popovic 2000) in which the solar motion was determined relative to the local centroid. These authors concluded that the residual velocity of the solar motion is about 10 km s$^{-1}$ toward the Galactic center, in the range from 10 to 15 km s$^{-1}$ along the Galactic rotation, and 7 km s$^{-1}$ (the same value in the papers of different authors) toward the north Galactic Pole. The solar motion along the $z$ axis is determined more reliably than that in the Galactic plane. This may be because the Galactic potential is not stationary and rotationally symmetric (Metzger *et al.* 1998).

We took the following residual velocities of the solar motion relative to the local centroid: 10, 15, and 7 km s$^{-1}$. Note that the velocity along the Galactic rotation may be slightly overestimated [see Feast (2000) for a discussion]. The lag velocity of the local-centroid motion relative to the circular velocity is taken to be 13 km s$^{-1}$ (Ninković 1992b; Chen 1997).

Note that the variation in initial conditions due to the residual solar motion does not cause any significant changes in the orbital parameters of nearby stars (Ninkovic *et al.* 1999). Thus, it is of little importance in our study precisely which values are taken for the residual velocities of the solar motion and for the lag velocity of the local centroid relative to the circular motion. The final results are obtained for the components of the solar motion relative to the Galactic center.

We chose the following three stars as comparison objects: the Sun, Gliese 1, and Gliese 445. The Sun is a typical disk object, Gliese 1 represents the thick-disk population, and the subdwarf Gliese 445 belongs to the halo population.

The results of our calculations are presented in the table. The following notation is used: the mean

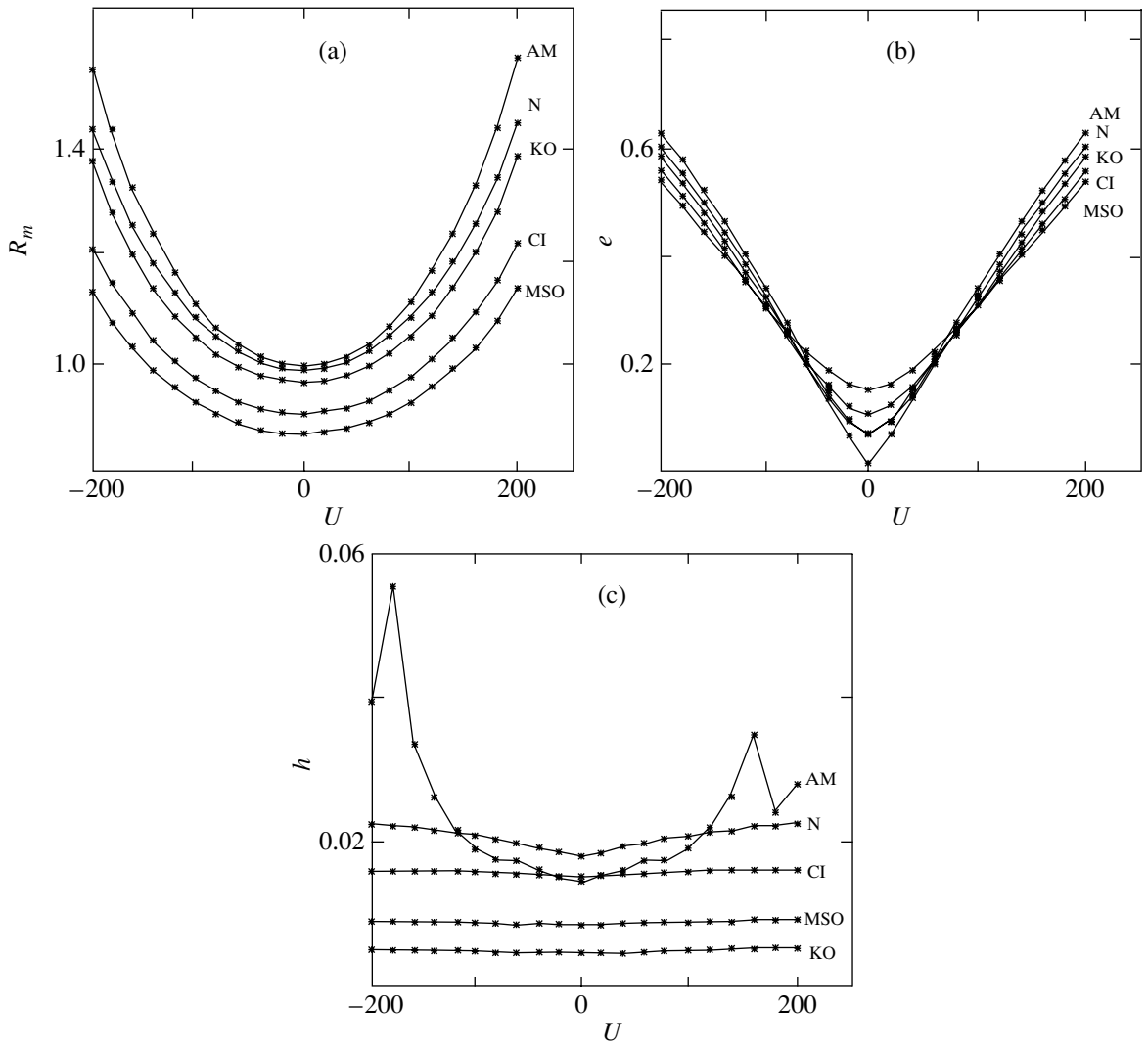


**Fig. 1.** (a) the mean relative distance from the Galactic rotation axis, (b) orbital eccentricity, and (c) maximum relative recession from the Galactic symmetry plane versus initial velocity $U$ for different models.

distance from the rotation axis, in units of $R_0$ (the distance from the Sun to the Galactic center),

$$R_m = \frac{R_a + R_p}{2R_0},$$

where $R_a$ and $R_p$ are the apogalactic and perigalactic distances, respectively; the orbital eccentricity

$$e = \frac{R_a - R_p}{R_a + R_p};$$

the maximum relative recession from the Galactic plane

$$h = \frac{|z|_{\max}}{R_m R_0},$$

where $|z|_{\max}$ is the maximum distance from the symmetry plane. We normalized our calculations to $R_0$, because it differs for different models (from 8 to 10 kpc), which results in large discrepancies between the mean distances from the Galactic rotation axis, if these are expressed in physical units.

The Sun and Gliese 1 have box-shaped orbits, while Gliese 445 has a box-shaped orbit in four models and a tube-shaped orbit in one model CI.

Note that $R_m$ and $e$ differ little from model to model. The difference between the values of $h$ is larger. This is attributable to the difference in the accelerations along the $z$ in different models, i.e., to different concetrations of the matter toward the Galactic plane.

Note also that a small change in the initial conditions, for example, by several km $s^{-1}$ in the velocities, causes a change in the type of orbit for Gliese 445 in the CI model, its tube-shaped orbit becomes a box-shaped one. The orbital shape is more sensitive to a change in the initial conditions and the choice of a model than are the orbital elements.

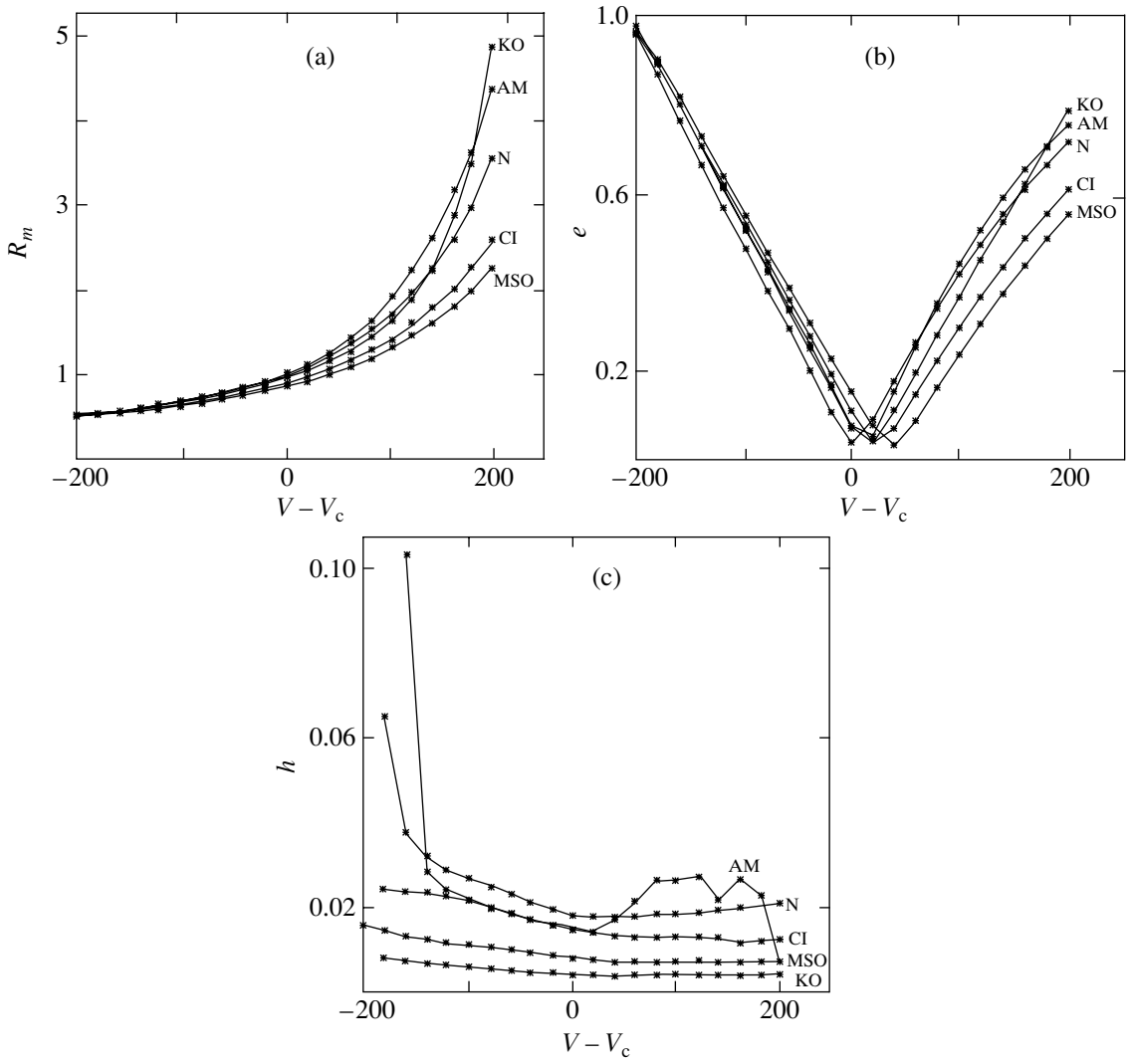


**Fig. 2.** Same as Fig. 1 but versus initial velocity $V$.

## 3. THE ORBITS OF MODEL OBJECTS

Let us consider several orbits of model objects in the five Galactic gravitational field potentials we chose. First, note that $R_0$ and the corresponding circular velocity $V_c$ slightly differ from model to model. To compare the orbits in the models under consideration, we chose the same initial coordinates $R_0 = 8.5$, $z_0 = 0$ kpc and initial velocities $(U, V, W)$ for all models.

All orbits with small $|U|$, $|W|$, and $|V - V_c|$ are box-shaped. If the initial conditions are near a resonance, then the orbit is tube-shaped.

Consider the change in the orbital shape and orbital elements when one of the velocity components varies, while the other two components are fixed. First, we fix the initial velocities $W = 10$ km s$^{-1}$ and $V = 210$ km s$^{-1}$ and vary the velocity $U$ in the range $-200$ to $+200$ km s$^{-1}$. Figures 1a–1c show plots of the orbital elements $R_m, e, h$ against $U$ for the five models we considered. Qualitatively, all models yield similar relations. The quantitative differences can be very large. The relative deviations of $h$ in the $z$ direction are small, because the initial velocity $W$ is small. All orbits are box-shaped and are strongly pressed to the Galactic plane. Note that the anomalistic period $P_a$ (the time interval between two successive passages through the orbital apocenter) increases with $|U|$. This is because the orbital eccentricity increases. At low eccentricities, $P_a \sim (1 + e)$. At higher $e$, the anomalistic period changes faster with orbital eccentricity.

Let us consider the variations in $V$ at fixed $U = 10$ km s$^{-1}$ and $W = 10$ km s$^{-1}$. The results are shown in Figs. 2a–2c. Qualitatively, the $V$ dependences of the orbital elements are similar for all models used. The quantitative differences in $R_m$ increase

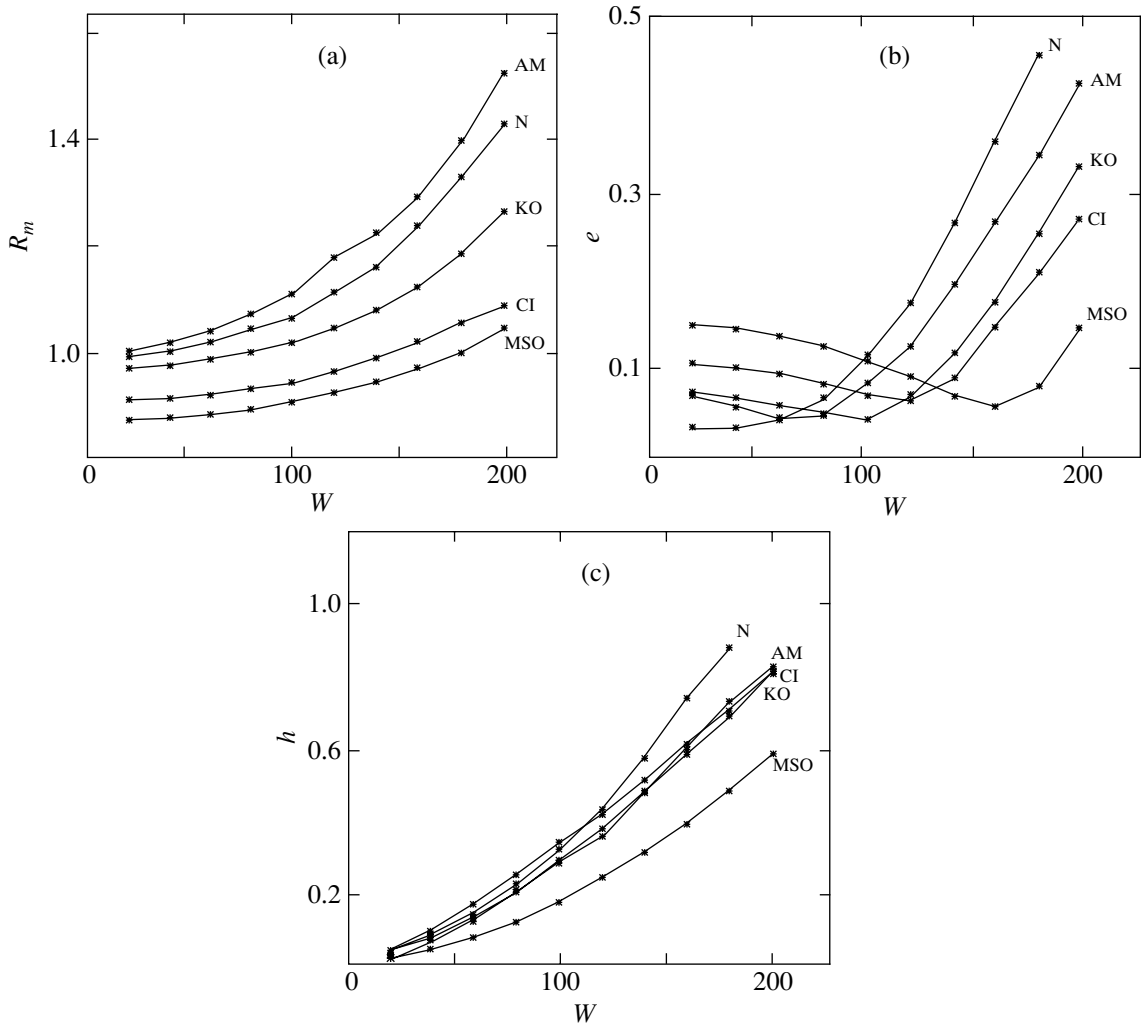


**Fig. 3.** Same as Fig. 1 but versus initial velocity $W$.

with $V$. The differences in the eccentricities also increase with $V$. The $h(V)$ dependences exhibit an abrupt rise at low velocities, $V - V_c < -100$ km s$^{-1}$. As $V$ decreases, the box sides also become increasingly curved. This may be because the particle fell within the central Galactic region where the gravitational potential varies greatly.

The variations in velocity $W$ were considered at fixed $U = 10$ km s$^{-1}$ and $V = 210$ km s$^{-1}$. The results are shown in Figs. 3a–3c. The discrepancies between the orbital elements for different models are large and increase with $W$. As $W$ increases, the boxes become curvilinear. Some box-shaped orbits can become tube-shaped or ergodic.

For some models, breaks are observed in the dependences of the orbital elements on the initial velocities. They may be attributable to the complex form of the potential, particularly for the AM model.

## 4. DISCUSSION

We have analyzed the orbits of specific stars and test particles in five different Galactic models. The orbital eccentricities for disk stars in different models were shown to agree. The differences between the eccentricities do not exceed 0.05. The maximum relative recessions from the Galactic plane can differ much more significantly (the discrepancies reach 100%), which is attributable to the difference between the forces acting orthogonally to the disk plane, i.e., to different disk surface densities in different galactic models.

For thick-disk and halo objects, the discrepancies between the orbital elements inferred in different models are much larger than those for thin-disk objects. In particular, the differences between the eccentricities can reach 0.5, while those between relative amplitudes of vertical oscillations can reach 100% or even higher. Since the types of orbits can also differ

in different models, the orbital elements and even the type of orbit are determined with a large uncertainty for individual thick-disk and halo objects.

## REFERENCES


1. C. Allen and M. A. Martos, Rev. Mex. Astron. Astrofis. **13**, 137 (1986).
2. O. Bienaymé, Astron. Astrophys. **341**, 86 (1998).
3. R. G. Carlberg and K. A. Innanen, Astron. J. **96**, 666 (1987).
4. B. Chen, Astron. J. **113**, 311 (1997).
5. W. Dehnen, Astron. J. **119**, 800 (2000).
6. W. Dehnen and J. J. Binney, Mon. Not. R. Astron. Soc. **298**, 387 (1998).
7. M. Feast, Mon. Not. R. Astron. Soc. **313**, 596 (2000).
8. S. A. Kutuzov and L. P. Osipkov, Astron. Zh. **66**, 965 (1989) [Sov. Astron. **33**, 498 (1989)].
9. M. R. Metzger, J. A. R. Caldwell, and P. L. Schechter, Astron. J. **115**, 635 (1998).
10. M. Miyamoto and Z. Zhu, Astron. J. **115**, 1483 (1998).
11. M. Miyamoto, C. Satoh, and M. Ohashi, Astron. Astrophys. **90**, 215 (1980).
12. S. Ninković, Astron. Nachr. **313**, 83 (1992a).
13. S. Ninković, Astrophys. Space Sci. **187**, 159 (1992b).
14. S. Ninkovic, N. Popovic, and V. Zivkov, Serb. Astron. J. **159**, 45 (1999).
15. N. Popovic, Magistarski rad (Universitet v Belgrade, 2000).
16. N. Reid, Astron. J. **115**, 204 (1998).


*Translated by A. Dambis*

*Astronomy Letters, Vol. 28, No. 3, 2002, pp. 169–173. Translated from Pis'ma v Astronomicheskiĭ Zhurnal, Vol. 28, No. 3, 2002, pp. 195–200.*


# New Magnetic Chemically Peculiar Stars

**V. G. El'kin, D. O. Kudryavtsev, and I. I. Romanyuk***

*Special Astrophysical Observatory, Russian Academy of Sciences, Nizhnii Arkhys, Karachai-Cherkessian Republic, 369167 Russia*

Received October 3, 2001

**Abstract**—Our observations with the 6-m telescope revealed six new magnetic chemically peculiar (CP) stars among objects with large depressions in the continuum: HDE 293764, BD+17°3622, HD 169887, HDE 231054, HDE 338226, and HDE 343872. The presence of a magnetic field is suspected in several other CP stars. The maximum longitudinal field component $B_e$ exceeds 1.5 kG for all six stars; in HDE 293764 and HDE 343872, it reaches 3.8 kG. For each object, we present our magnetic-field measurements and published data on previous studies. The method of searching for magnetic stars based on an analysis of spectrophotometry shows its efficiency. © *2002 MAIK "Nauka/Interperiodica".*

Key words: *stars—variable and peculiar*

## INTRODUCTION

The continua of magnetic chemically peculiar (CP) stars exhibit broad (200–300 Å) and shallow (with a depth of several percent) depressions. These and other anomalies in the energy distribution typical of CP stars were found by Glagolevskij (1966) and Kodaira (1969). Various criteria were developed to distinguish CP stars from normal stars based on intermediate-band photometric observations, in particular, near the best studied depression at λ5200 Å (Maitzen 1976; Straizys 1977). A long series of photoelectric observations carried out in the 1970s revealed a clear correlation between the surface magnetic field of a CP star and the so-called $z$ parameter of the Geneva photometric system, which is related to the depression at λ5200 Å. Cramer and Maeder (1980) proposed a list of 258 stars in which a surface magnetic field $B_s$ of more than 1 kG was predicted from the Geneva photometry.

In contrast to stellar magnetic-field measurements, the Geneva photometry can be performed with small telescopes. Therefore, the number of observations could be sharply increased if the above criterion were efficient. This would allow actual candidates for new magnetic stars to be effectively identified.

In the early 1980s, an extensive program of observations of CP stars with the largest $z$ parameters was carried out with a Zeeman analyzer attached to the 6-m Special Astrophysical Observatory telescope (Glagolevskij *et al.* 1982, 1985). We studied virtually all observable stars, considering that high-resolution Zeeman spectra could be obtained at that time only for stars brighter than $8–9^m$ even with the largest 6-m telescope. Circumstantial evidence suggested the existence of many actual candidates for magnetic stars among fainter objects, but it was impossible to carry out accurate Zeeman observations for them.

Magnetic fields were detected approximately in 30% of the candidate objects we observed, but the correlation between the field strength and the $z$ parameter proved to be weak. It should be borne in mind that only the longitudinal magnetic-field component B is measured during observations with a Zeeman analyzer; the surface magnetic field $B_s$ is then determined by modeling using various assumptions about the magnetic-field configuration of the star. In most cases, the field may be assumed to be dipole, which simplifies the situation. Glagolevskij *et al.* (1985) concluded that the Geneva photometry could be effectively used to search for new magnetic stars, whereas direct field measurements should not be substituted with indirect photometric determinations based on an empirical relation because of their poor agreement with the Zeeman observations.

Since Zeeman measurements (in contrast to photometry) can be carried out only with large telescopes whose observing time is in great deficit, a mere 211 magnetic stars were found in more than 50 years of observations (Romanyuk 2000), which accounts for ~3% of the total number of all known CP stars (Renson *et al.* 1991). Despite the progress in technology, the discovery rate of new magnetic stars (on average, four stars per year) remains the same.

*E-mail: roman@sao.ru

1063-7737/02/2803-0169$22.00 © 2002 MAIK "Nauka/Interperiodica"

**Table 1**

| Star HD/HDE | Alternative name | Coordinates (2000.0) | | $V$ magnitude | Spectral type |
|---|---|---|---|---|---|
| | | $\alpha$ | $\delta$ | | |
| HDE 293764 | BD−03°987 | $05^h\,03^m\,34\overset{s}{.}5$ | −02° 58′ 46″ | 9.6 | A2 SrCrEu |
| HD 169887 | BD+26°3260 | 18 25 44.2 | +26 39 25 | 9.0 | Ap Si |
| | BD+17°3622 | 18 32 51.5 | +17 18 12 | 8.8 | A2 SrEuCr |
| HDE 343872 | BD+24°3675 | 19 12 31.5 | +24 21 37 | 9.9 | Ap SrCrEu |
| HDE 231054 | BD+16°3801 | 19 16 58.4 | +16 15 11 | 10.0 | Ap SiSr |
| HDE 338226 | BD+24°3723 | 19 21 59.8 | +25 11 43 | 9.8 | A0 Si |

This number is not sufficient for the various statistical studies needed to understand the distribution of magnetic CP stars in the Galaxy and to search for relationships between the field configuration and direction for individual objects and the Galactic magnetic-field structure. It is particularly important to increase the number of magnetic-field measurements for CP stars that are members of open clusters with different ages.

Effective searches for new magnetic stars require revealing features in low-resolution spectra of CP stars that would suggest the presence of a magnetic field. Our approach is to analyze the $\lambda$5200 Å depression profile using the spectra taken with the UAGS spectrograph attached to the 1-m Special Astrophysical Observatory telescope. The techniques for a preliminary selection of candidates and for analysis of the depression profile will be described separately. We selected candidate stars to be observed with the Zeeman analyzer attached to the 6-m telescope using the data obtained with the 1-m telescope.

## OBSERVATIONS

The magnetic observations of our selected CP stars with strong depressions were carried out during 2000–2001 with Zeeman analyzers of the Main Stellar Spectrograph (MSS) attached to the 6-m telescope (Naidenov and Chuntonov 1976; Chountonov 1997). The light detector was a 1160 × 1040-pixel CCD array. The current state of the MSS and its new technical characteristics were described by Panchuk (2001). The technique for stellar magnetic-field observations was detailed by Romanyuk *et al.* (1998), and the data reduction procedures were described by Kudryavtsev (2000).

We selected 15 candidate stars for our observations with the 6-m telescope. Since these stars are all faint (typically $9–10^m$) objects for Zeeman spectroscopy even with the 6-m telescope equipped with modern sensitive light detectors, they require much observing time.

We obtained more than 50 Zeeman spectra of all the 15 selected stars during 2000–2001. Here, we present our measurements of the longitudinal magnetic-field component only for those of them for which at least three Zeeman spectra were available. All the 15 stars with large depressions are apparently magnetic, but we decided not to draw final conclusions about the presence of a magnetic field for those of them with only one or two measurements. They need further studies, and the results on them will be published later.

Table 1 presents information on the six CP stars for which we carried out at least three observations. The columns of Table 1 contain the following: HD or HDE numbers of the stars, their alternate names, equatorial coordinates $\alpha$ and $\delta$ for 2000, visual $V$ magnitudes, spectral types, and the types of chemical anomalies.

All observations were performed in the spectral range 4450–4620 Å. The spectral resolution (two CCD pixels) was 0.3 Å.

## RESULTS

A log of observations and the measured magnetic fields of the above six CP stars with large depressions are given in Table 2. The columns of Table 2 contain the following: midexposure Julian dates; exposure times, $t_{exp}$; mean signal-to-noise ratios in the continuum, S/N; the number of lines measured in the spectrogram, $[n]$; and longitudinal magnetic-field components with their rms errors, $B_e \pm \sigma$.

On each night, we observed standard stars: (1) nearby bright cool stars with numerous sharp lines to be used to measure the magnetic field with an accuracy of ∼20–30 G considered as zero-point standards to allow for and eliminate various instrumental drifts; (2) CP stars with well-studied magnetic fields (e.g., 53 Cam, $\alpha^2$ CVn, 52 Her, and others) to check that the analyzer was correctly set on the spectrograph slit and that its parameters during the

observations were stable. This technique for studying magnetic fields has been used on the 6-m telescope for many years (Romanyuk *et al.* 1998). All check measurements indicate that our instruments worked stably.

As follows from Table 2, all the stars turned out to be magnetic, with very strong global fields of more than 1 kG. The spectrum of each star exhibits many narrow and sharp lines with FWHMs no larger than 0.5–0.6 Å. This allowed us to measure from 40 to 60 lines in each spectrogram, which provided a high accuracy of the sought-for longitudinal magnetic-field component. The contribution of the magnetic field to the line-profile broadening must be significant, but it can be calculated only after obtaining the $B_e$ magnetic curve and performing model calculations. The projected rotational velocities $v \sin i$ were determined by comparing the observed profiles of the Fe II 4508 Å line (with a low Lande factor = 0.5) with a synthetic spectrum. The VALD database (Kupka *et al.* 1999) was used for line identification.

Below, we give brief comments on each of the measured stars.

**HD 293764 = BD−03°987 = HIP 23533.** The star was taken from the catalog of CP stars by Egret and Jaschek (1981). It is a member of the cluster Ori OB1 (De Geus *et al.* 1987). Since its Hipparcos parallax is very small, $\pi = 0''.89$, its distance cannot be accurately determined by the trigonometric method.

Three measurements of $B_e$ performed over a period of about two months gave virtually the same value, +3.5–4 kG. Because of the paucity of these data, as yet, we cannot determine whether the star has a fairly long (>1 yr) rotation period, or BD−03°987 has such a spatial orientation that it is always seen from its positive magnetic pole.

**HD 169887 = BD+26°3260 = Cou 815.** This star was also taken from the catalog of CP stars by Egret and Jaschek (1981). Silicon lines are enhanced in its spectrum. The three Zeeman spectrograms taken on three consecutive nights show the variability of $B_e$; the longitudinal field component changed its sign from negative to positive during the three days. One might expect the period of magnetic variability from these data to be of the order of a week.

The variability amplitude of the longitudinal field component may be large. A comparison of the observed and synthetic profiles for the Fe II 4508 Å line yields an estimate of $v \sin i \sim 25$ km s$^{-1}$.

The star is binary; its secondary component (fainter by $2^m$) is at a distance of $1''.2$ (Couteau 1973). There was good seeing during our observations ($\sim 1''$). The secondary component was visible, but it did not fall on the spectrograph slit and, thus, did not distort the spectrum of the primary component.

**Table 2**

| JD 2450000+ | $t_{exp}$, min | S/N | $[n]$ | $B_e \pm \sigma$, G |
|---|---|---|---|---|
| HDE 293764 = BD−03°987 | | | | |
| 1806.558 | 30 | 100 | 38 | 4040 ± 230 |
| 1807.529 | 30 | 100 | 48 | 3770 ± 310 |
| 1864.505 | 30 | 100 | 44 | 3590 ± 290 |
| HD 169887 = BD+26°3260 | | | | |
| 2128.492 | 40 | 80 | 39 | −2340 ± 290 |
| 2129.358 | 40 | 80 | 50 | 540 ± 230 |
| 2130.360 | 40 | 60 | 44 | 1210 ± 240 |
| BD+17°3622 | | | | |
| 1275.555 | 30 | 100 | 47 | 1600 ± 160 |
| 2069.512 | 60 | 100 | 45 | 1510 ± 240 |
| 2127.417 | 40 | 100 | 49 | 980 ± 130 |
| HDE 343872 = BD+24°3675 | | | | |
| 1768.504 | 25 | 50 | 48 | 3590 ± 300 |
| 1770.391 | 50 | 30 | 42 | 2160 ± 400 |
| 1798.267 | 40 | 80 | 42 | 660 ± 340 |
| 1799.286 | 60 | 150 | 49 | −760 ± 220 |
| 1800.432 | 40 | 40 | 35 | −600 ± 300 |
| 1802.347 | 80 | 110 | 60 | 3860 ± 250 |
| 1804.315 | 100 | 70 | 46 | 2730 ± 370 |
| 1806.185 | 40 | 60 | 52 | 1980 ± 350 |
| 1807.185 | 50 | 100 | 53 | 1510 ± 190 |
| 1893.122 | 20 | 40 | 37 | 2210 ± 350 |
| 1952.648 | 60 | 80 | 48 | 3300 ± 200 |
| 1953.622 | 30 | 60 | 46 | 2950 ± 210 |
| 2069.458 | 80 | 90 | 40 | 2850 ± 200 |
| 2127.283 | 50 | 50 | 45 | 2870 ± 230 |
| 2128.283 | 50 | 60 | 58 | 3810 ± 230 |
| 2130.435 | 50 | 60 | 49 | 2660 ± 210 |
| HDE 231054 = BD+16°3801 | | | | |
| 2127.502 | 50 | 45 | 41 | 960 ± 250 |
| 2128.417 | 50 | 60 | 45 | 1840 ± 250 |
| 2129.395 | 50 | 50 | 51 | 2530 ± 270 |
| 2130.395 | 50 | 60 | 43 | 380 ± 170 |
| HDE 338226 = BD+24°3723 | | | | |
| 2127.545 | 50 | 40 | 35 | 1040 ± 230 |
| 2128.458 | 50 | 60 | 41 | 440 ± 180 |
| 2129.433 | 50 | 60 | 37 | 1490 ± 170 |

**BD+17°3622**. The SrEuCr star BD+17°3622

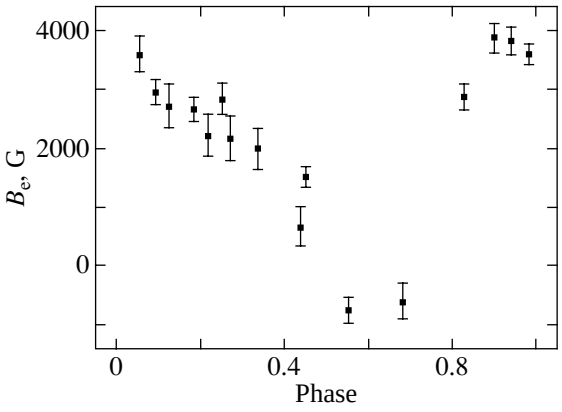


Variations in the longitudinal magnetic-field component $B_e$ of HDE 343872. The elements used are $JD = 2451768.0 + 8^d.8$.

was chosen from a list of objects whose spectra were obtained with an objective prism (Bidelman 1985). This is a poorly studied star, and we found no other information on it.

The three spectrograms taken over a long period (850 days) show a longitudinal field component of positive polarity. The star is apparently seen mostly from its positive magnetic pole, although the probability that there is a very long period is not ruled out either. We estimated $v \sin i$ to be no larger than 20 km s$^{-1}$.

**HDE 343872 = BD+24°3675.** This is an outstanding object of our program. BD+24°3675 = HDE 343872 was first classified as a Si peculiar star by Bidelman (1983) based on objective-prism spectra. Schneider (1986) included it in the list of CP2 stars to be observed in Strömgren's system to determine its photometric indices, $H_\beta$ and $\Delta a$. Schneider's studies revealed a variable depression at $\lambda$5200 Å in BD+24°3675 exhibited, which is the largest among all previously observed CP stars, with $\Delta a$ from 0.067 to 0.146. Because of the small number of observations, Schneider (1986) was able to estimate the variability period of $\Delta a$ only roughly: from 7 to 9 days.

Subsequently, Kroll (1992) carried out its spectroscopic observations. He found $T_{eff} = 10\,500$ K and $\log g = 3.1$, suggesting that BD+24°3675 is an evolved star. Its spectrum exhibits enhanced chromium and iron lines.

Thus, we had strong grounds for including the CP star BD+24°3675 with the largest depression ever observed, which also exhibited the largest periodic variations, in our program of observations with the 6-m telescope to search for and thoroughly study its magnetic field.

We obtained 16 Zeeman spectra of BD+24°3675 during 2000–2001. Even the first measurement showed the star to have a strong magnetic field. We see from the figure that $B_e$ varies between −700 and +3800 G with a period of ∼8.8 days. We found no split Zeeman components in the spectrum, suggesting an upper limit on the surface field $B_s <$ 20 kG. The radius of the star is $\sim 3R_\odot$, which allows its equatorial rotational velocity to be determined using the 8.8-day period and standard relations, $v_e = 18$ km s$^{-1}$. However, the narrowest lines in its spectrum are 0.4 Å wide, suggesting that $v \sin i \lesssim$ 20 km s$^{-1}$ (based on a comparison of the observed and synthetic spectra). Clearly, magnetic broadening is of great importance here. Let us estimate its importance at least roughly, because, as yet, no model of the stellar magnetic field has been constructed. From the maximum longitudinal field component $B_e$ of ∼4 kG, we may draw a definitive conclusion that the magnitude of the magnetic field averaged over the entire surface, $B_s$, will be >8–10 kG, almost irrespective of its configuration.

If the surface field $B_s$ of the star is 10–20 kG, magnetic broadening can contribute ∼50% of the total line width, depending on the Lande factor of the line. The contribution of magnetic broadening cannot be ignored when studying the chemical composition of the stellar atmosphere.

The results of our detailed study of the magnetic field, chemical composition, and other parameters of BD+24°3675 will appear in a separate paper.

**HDE 231054 = BD+16°3801.** The star was selected from the catalog by Egret and Jaschek (1981). It was first detected as a peculiar star by Bond (1970) based on objective-prism spectra. Silicon and strontium lines are enhanced in its spectrum.

Our measurements on four consecutive nights took place at the phase of a positive extremum of the star's longitudinal magnetic field. The field variability period is no less than three days. The lines with different Lande factors are clearly seen to have different widths. The value of $v \sin i$ determined from the Fe II 4508 Å line does not exceed 20 km s$^{-1}$.

**HDE 338226 = BD+24°3723.** The star is listed in the catalog of early-type CP stars (Egret and Jaschek 1981) as a silicon peculiar star. It was first found as a peculiar star by Bond (1970) from objective-prism observations.

Our Zeeman spectra obtained on three consecutive nights point to a field of positive polarity. The Fe II 4508 Å line profile indicates that $v \sin i$ is less than 20 km s$^{-1}$; the rotation period is apparently more than three days.

## CONCLUSIONS

Thus, the six most thoroughly measured candidates for magnetic stars we selected turned out to be bona fide magnetic stars with field strengths larger than 1.5 kG. The maximum longitudinal field component exceeds 2.3 kG and 3.8 kG in four and two of them, respectively.

Note that an analysis of the data from the catalog of magnetic stars (Romanyuk 2000) shows the number of CP stars with measured magnetic fields to decrease sharply in the range of strong magnetic fields: of the total number of 211 objects, the longitudinal magnetic-field component $B_e$ at maximum exceeds 1.5 kG only in 74 stars, 2.3 kG in 30 stars, and 3.8 kG in 11 stars. Thus, our data allow the number of known, comparatively rare magnetic stars with the strongest fields to be increased.

In addition to the above results, we obtained Zeeman spectra for nine more CP stars with large depressions, but only one or two observations for each of them. The data on them are still too scarce to draw final conclusions as to whether these stars are magnetic. Nevertheless, there is evidence for the presence of a field in all of them.

Thus, we may conclude that our technique is efficient enough to be used to search for magnetic stars among faint objects.

## ACKNOWLEDGMENTS

We are grateful to G.A. Chuntonov for help in preparing these observations and for the participation in them. We are also grateful to the referees for helpful remarks, which improved the paper. We wish to thank the Committee on the Subject of Large Telescopes of the Russian Academy of Sciences and the administration of the Special Astrophysical Observatory for support of the studies of stellar magnetic fields with the 6 m telescope. This work was supported in part by the Russian Foundation for Basic Research (project no. 00-02-16460). We used the VALD and SIMBAD databases.

## REFERENCES

1. W. P. Bidelman, Astron. J. **88**, 1182 (1983).
2. W. P. Bidelman, Astron. J. **90**, 341 (1985).
3. H. E. Bond, Publ. Astron. Soc. Pac. **82**, 321 (1970).
4. G. A. Chountonov, in *Stellar Magnetic Fields: Proceedings of the International Conference, 1996,* Ed. by Yu. V. Glagolevskij and I. I. Romanyuk (Moscow, 1997), p. 239.
5. P. Couteau, Astron. Astrophys., Suppl. Ser. **10**, 273 (1973).
6. N. Cramer and A. Maeder, Astron. Astrophys., Suppl. Ser. **41**, 111 (1980).
7. E. J. De Geus, J. Lub, and E. Van de Grift, Astron. Astrophys., Suppl. Ser. **69**, 505 (1987).
8. D. Egret and M. Jaschek, Comptes Rendus Symp. Liege, No. 23, 495 (1981).
9. Yu. V. Glagolevskij, Candidate's Dissertation (Inst. Astrofiziki, Alma-Ata, 1966).
10. Yu. V. Glagolevskij, V. D. Bychkov, I. Kh. Iliev, *et al.*, Pis'ma Astron. Zh. **8**, 26 (1982) [Sov. Astron. Lett. **8**, 12 (1982)].
11. Yu. V. Glagolevskij, V. D. Bychkov, I. I. Romanyuk, and N. M. Chunakova, Astrofiz. Issled. (Izv. SAO) **19**, 37 (1985).
12. K. Kodaira, Astrophys. J. **157**, 59 (1969).
13. R. Kroll, in *Proceedings of International Astronomical Union Colloquium no. 138 "Peculiar Versus Normal Phenomena in A-type and Related Stars,"* Ed. by M. M. Dworetsky, F. Castelly, and R. Farragiana, Astron. Soc. Pac. Conf. Ser. **44**, 75 (1992).
14. D. O. Kudryavtsev, in *Magnetic Fields of Chemically Peculiar and Related Stars: Proceedings of the International Meeting, 1999,* Ed. by Yu. V. Glagolevskij and I. I. Romanyuk (Moscow, 2000), p. 84.
15. F. Kupka, N. Piskunov, T. A. Ryabchikova, *et al.*, Astron. Astrophys., Suppl. Ser. **138**, 119 (1999).
16. H. M. Maitzen, Astron. Astrophys. **51**, 223 (1976).
17. I. D. Naidenov and G. A. Chuntonov, Soobshch. SAO **16**, 63 (1976).
18. V. E. Panchuk, Preprint No. 154, SAO (2001).
19. P. Renson, R. Farragiana, and F. Catalano, Astron. Astrophys., Suppl. Ser. **89**, 429 (1991).
20. I. I. Romanyuk, in *Magnetic Fields of Chemically Peculiar and Related Stars: Proceedings of the International Meeting, 1999,* Ed. by Yu. V. Glagolevskij and I. I. Romanyuk (Moscow, 2000), p. 18.
21. I. I. Romanyuk, V. G. Elkin, D. O. Kudryavtsev, *et al.*, Bull. Spec. Astrophys. Obs. **45**, 93 (1998).
22. H. Schneider, Astron. Astrophys. **161**, 203 (1986).
23. V. L. Straizys, *Multicolor Stellar Photometry* (Mokslas, Vilnius, 1977; Pachart Publ. House, Tucson, 1992).

*Translated by N. Samus'*

*Astronomy Letters, Vol. 28, No. 3, 2002, pp. 174–181. Translated from Pis'ma v Astronomicheskiĭ Zhurnal, Vol. 28, No. 3, 2002, pp. 201–209.*


# An Electronic Version of Volume I of the General Catalogue of Variable Stars with Improved Coordinates

**N. N. Samus'[1,2,*], V. P. Goranskii[2], O. V. Durlevich[2], A. V. Zharova[2], E. V. Kazarovets[1], E. N. Pastukhova[1], M. L. Hazen[3], and T. M. Tsvetkova[1]**

[1]*Institute of Astronomy, Russian Academy of Sciences, ul. Pyatnitskaya 48, Moscow, 109017 Russia*
[2]*Sternberg Astronomical Institute, Universitetskii pr. 13, Moscow, 119899 Russia*
[3]*Harvard Observatory, 60, Garden Str., Cambridge, MA, 02138 USA*

Received October 17, 2001

**Abstract**—We present a new electronic version of the first volume of the General Catalogue of Variable Stars (GCVS), fourth edition, which contains data on 10 558 variable stars in Andromeda–Crux (the constellations are ordered in the Catalog according to the Latin alphabet). This version incorporates the name lists of variable stars from no. 67 to no. 76 for the same constellations. The main distinctive feature of the new version is that it provides improved equatorial J2000.0 coordinates for 10 349 stars (including those for 4587 stars corrected for proper motions). These are based on identifications with positional catalogs using finding charts and on our new measurements. We searched for a number of stars on original plates from the plate collections of several observatories. The version also includes a file of remarks to the first GCVS volume and a preliminary version of the file of bibliographic references to the entire fourth edition of the GCVS. Apart from a complete update of the positional information, the new version incorporates all the other corrections that were found to be necessary after the first GCVS volume was published (1985).


Key words: *stars—variable and peculiar*

## INTRODUCTION

The fourth edition of the General Catalogue of Variable Stars (GCVS; Kholopov *et al.* 1985–1988) contains data on 28 435 Galactic variables in its volumes I–III (not counting the named variables that proved to be nonexistent: minor planets mistaken for stars, artifacts due to double plate exposures, etc.). Given the ten subsequent name lists of variable stars (from no. 67 to no. 76), the number of named Galactic variable stars in 2001 exceeded 37 300.

Traditionally, the GCVS presented the coordinates of variable stars to within 1 s in right ascension and 0.1 arcmin in declination. In general, this accuracy corresponded to the accuracy of positional information in the original publications on the discovery of each variable star; in comparatively rare cases, the originally more accurate coordinates in the GCVS were rounded off. An appreciable fraction of the GCVS stars have even rougher coordinates than the standard accuracy or, occasionally, simply erroneous coordinates. Such a low positional accuracy makes it impossible to identify faint variable stars from their coordinates in the absence of finding charts. The automatic pointing of ground-based and space-borne telescopes at these objects is not possible either. In recent years, numerous projects aimed, among other tasks, at the mass automatic discovery of variable stars in fairly extended areas (MACHO, OGLE, ASAS, and others) have been under way. The impossibility of quick automatic check of the lists of new discoveries for the presence of objects identical to the already known variables, because the GCVS coordinates are too rough, prevents these stars from being included in the GCVS system.

Thus, it seems of current interest to prepare a GCVS version with improved coordinates for all the cataloged stars, wherever possible. If a star's proper motion could be found in existing positional catalogs, then we decided to include it and to take it into account in our version.

Here, we present a new version of the catalog for Volume I of the GCVS. Subsequently, we are planning to publish new versions of the GCVS Volumes II and III, as well as of the catalog of suspected variable stars (the NSV catalog). We are currently actively working on these new versions.

*E-mail: samus@sai.msu.ru

1063-7737/02/2803-0174$22.00 

## METHODS FOR PREPARING THE CATALOG

With the appearance of new extensive positional catalogs, primarily the A1.0/A2.0 catalogs of the US Naval Observatory (USNO A1.0/A2.0; Monet *et al.* 1998) containing about 500 000 000 stars, the problem formulated above can now be effectively solved. For stars as faint as about $21^m$, these catalogs provide the coordinates determined from Schmidt-telescope survey plates that are accurate enough for our purposes, as well as their blue and red magnitudes.

The existence of Digitized Sky Survey (DSS) images for any region of the sky also opens up great possibilities. Owing to the variable-star database maintained by the GCVS team, we have the most complete information on published finding charts of variable stars at our disposal; unpublished charts for several thousand stars were provided by their discoverers and other researchers. Finally, we have the Sternberg Astronomical Institute (SAI) plate collection at our disposal, which allows the variable stars "lost" because of the lack of finding charts and inaccurate coordinates to be rediscovered in many regions of the sky. In our work, we also used the plate collections of other observatories. The world's richest Harvard Observatory plate stacks (USA) contain the numerous marks left by the discoverers directly on plates, which allows variable stars to be found (among some 13 000 variables discovered at the Harvard Observatory, about 3000 objects have no published finding charts). For several stars without charts, a clear variability can be revealed by a comparison of catalogs or DSS images. The possibility of judging the colors of stars offered by the USNO catalogs is very useful in identifying strongly colored objects (e.g., Mira-type variables). Unfortunately, the red and blue magnitudes for many fields refer to the plate epochs separated in time by a long interval, and the color indices of highly variable stars can be fictitious, reflecting primarily the variability between the two epochs rather than the color. Nevertheless, in several cases, the confidence in the identification being correct is reinforced precisely because the color indices of the corresponding stars in the USNO catalogs are unrealistically blue. Many red variable stars with no charts can be reliably identified, because their positions closely coincide with those of objects in the infrared IRAS Point Source Catalog (Neugebauer *et al.* 1988), particularly if a high probability of variability was noted for the IRAS object; in most cases, the accuracy of the IRAS coordinates makes the identification with positional catalogs quite reliable. However, the "associations" (positional coincidences, possible identifications) contained in the IRAS catalog are not always correct identifications, particularly in crowded star fields (in volume I of the GCVS, such cases are most common in Corona Australis).

Among the Harvard variable stars, there are many stars with the only finding chart published in the atlas by Tsesevich and Kazanasmas (1971). These valuable charts are generally based on Tsesevich's searches in the Harvard plate stacks in the 1950s. Unfortunately, mistakes are commonly found in the atlas (thus, among the many cases where two charts of the atlas show the same variable, there are occasions of different identifications suggested by the two charts, without any stipulation). Occasionally, the star marked in the chart is too far from the position published by its discoverer. In these cases, a check of the Harvard plates commonly allows a different, correct identification to be achieved. In addition, the hand-drawn charts of the atlas are difficult to use in crowded star fields. We tried to be cautious when using the charts by Tsesevich and Kazanasmas.

During the initial preparation of the GCVS version with improved coordinates, we made an attempt to automatically identify the GCVS with the Hubble Space Telescope Guide Star Catalog (GSC; Lasker *et al.* 1990), which revealed an unacceptably large number of incorrect or missed identifications. Therefore, we decided to check all identifications using finding charts. An independent solution of this problem at the SAI Department of Astrometry led to the compilation of a catalog by Gulyaev and Ashimbaeva (1997). Unfortunately, so far this catalog is accessible neither electronically nor in any other form. In addition, since the authors of the catalog compared the finding charts only with the GSC (a limiting magnitude no fainter than $15^m$), the catalog by Gulyaev and Ashimbaeva could not cover all GCVS stars with sufficient completeness and did not invoke deeper catalogs or measurements of actual sky images. By contrast, we additionally used identifications with the USNO A1.0/A2.0 catalogs (in favorable cases, their limiting magnitude reaches $23^m$) and measured coordinates for stars that were absent even in these catalogs.

To perform identifications using charts required tools for visualizing the astronomical catalogs. Our main tool was the SIMFOV code written by A.A. Volchkov (SAI). In its current form (A. Volchkov and O. Volchkov 2001), the code allows one to display the chart of a selected sky field on the required scale with objects from the catalogs in the specified list and then to view it, zooming in and out, and to retrieve the information contained in the corresponding catalog that refers to any image. This code also enables an automatic identification of user lists with catalogs by coordinates with (or without) allowance for the match between magnitudes. Viewing images, retrieving information, and comparing lists are possible for the coordinates that refer to any equinoxes.

It has become possible to use the SIMFOV code for visualizing the USNO catalogs only recently, because it required much computer disk space. Previously, we used the special software for viewing the USNO A1.0/A2.0 catalogs directly from CD-ROMs that were kindly provided by J. Manek (Czech Republic).

The variable components of visual double and multiple systems required particular attention in preparing the catalog. In general, the components of sufficiently wide pairs are presented separately in positional catalogs and, thus, caused no difficulty. However, closer double and multiple stars in positional catalogs are often unresolved. In such cases, we used several approaches. For several variable components of double and multiple systems, we could measure the coordinates on Digitized Sky Survey images. In other cases, we applied a correction to the position of the double star's primary component based on the angular separation between the components and on the position angle at a certain epoch. Wherever possible, we also used data on the proper motions of each component or on the orbital motion in the system to reduce the coordinates to the epoch and equinox 2000.0.

## RESULTS

The electronic version of Volume I is accessible at

ftp.sai.msu.su/pub/groups/cluster/gcvs/gcvs/vol1/

or at

www.sai.msu.su/groups/cluster/gcvs/ gcvs/vol1/.

In its main table (vol1.dat), the new electronic version of volume I of the GCVS contains information on 10 558 objects (not counting the stars that were erroneously named for the second time or proved to be nonexistent) in Andromeda–Crux, which are mostly variable stars of our Galaxy discovered and named before 2001; i.e., it covers the variable stars that were included in the fourth edition of the GCVS and name lists nos. 67–76 (for the same constellations). For 10 349 variable stars, our version provides new equatorial J2000.0 coordinates (vol1_pos.dat), for 4587 stars with allowance for their proper motions; so far we have failed to determine accurate coordinates for 209 variable stars, because there are no finding charts and because the information for star identification is insufficient. The main table is supplemented with a list of remarks to volume I (rem.txt) published electronically for the first time and with a preliminary electronic version of bibliographic references (ref.txt) for volumes I–III of the 4th GCVS edition. A detailed description of the files can be found in the readme.txt file of the electronic version.

### *The File* vol1.dat

The structure of the main table (vol1.dat) corresponds to that of the combined table of the GCVS 4th edition and the name lists (Kholopov *et al.* 1998; see also www.sai.msu.su/groups/cluster/gcvs/gcvs/iii/iii.dat). The differences between these tables are as follows:

(1) Instead of B1950.0 coordinates, we provide new improved equatorial J2000.0 coordinates (right ascensions to within $0^s.1$ and declinations to within $1''$). The coordinates that could not be improved were recalculated from old rough coordinates to the equinox J2000.0 with allowance for precession.

(2) The most recent name lists, up to no. 76, were included.

(3) We included all the corrections and changes that were found during our work on the GCVS in other columns of the main table, in references, and in remarks. Note that for stars that had no published finding charts but that we identified with the GSC or with the US Naval Observatory (USNO) A1.0/A2.0 catalogs, we now give a symbol of the corresponding catalog (GSC, USNO) as a reference to the finding chart.

The main table is presented in the form traditional for the GCVS, i.e., in the order of constellations and variable-star names adopted in the GCVS. The table includes the following information: equatorial J2000.0 coordinates (right ascensions to within $0^s.1$ and declinations to within $1''$), variability types, magnitudes at maximum and minimum light, photometric magnitude systems, periods of light variations, durations of brightness rise from minimum to maximum or eclipse durations, spectral types, and bibliography. For the stars from name lists nos. 67–76 published after the appearance of the GCVS 4th edition, we provide not all columns of the table but only coordinates, variability types, magnitudes, and bibliography; the missing data will be added to the 5th edition of the GCVS.

### *The File* vol1_pos.dat

The table vol1_pos.dat provides positional information based on our identifications with major astrometric catalogs, on published data, or on our new measurements (see below) for 10 349 stars of the new version of volume I (including stars of the new name lists in the same constellations). The order of stars in this table is the same as that in the main table. It consists of the following columns:

(1) Ordinal star numbers in a system traditional for the electronic GCVS versions;

(2) GCVS star names;

(3) Improved equatorial J2000.0 coordinates (right ascensions to within $0^s.01$ and declinations to within $0''.1$);

(4) A flag indicating that the coordinates are actually rougher than the new accuracy standard adopted in the catalog, because we failed to determine better coordinates and to find them in source catalogs or in publications. In comparatively numerous cases, such coordinates were obtained by transforming B1950.0 coordinates from the IRAS Point Source Catalog (see below). The flag is a column (:) in the position that follows the coordinates;

(5) Proper motions (in arcseconds per year for both coordinates) to within $0''.001$ per year;

(6) Epochs of the given coordinates. No epoch is provided when using the coordinates from the literature if the epoch was not specified in the publication and could not be established;

(7) A flag indicating that the variable star's identification with the source catalog is uncertain (a question mark in the corresponding position);

(8) A brief designation of the source of astrometric data. In several cases, the catalog designation is followed by the symbol "+pm"; it implies that the position for a certain epoch was taken from the catalog and reduced to the epoch 2000.0 using information on the star's proper motion from a different source.

Below, we give a list of the major catalogs and other data sources used, roughly in the order of our preference in identifying variable stars (see also the description of the catalogs provided for A.A. Volchkov's visualization code we used at www.simfov.ru).

Hip—The Hipparcos Catalogue (ESA 1997).

Tyc2—The Tycho Catalogue (Høg *et al.* 2000). In isolated instances where the star is absent in the second Tycho catalogue but is present in the first catalogue (ESA 1997), the source is indicated as Tyc1.

PPM—The Positions and Proper Motions (Röser *et al.* 1991–1993).

NPM—The Lick Northern Proper Motion Program (Klemola *et al.* 1987).

AC—The Four-Million Star Catalog (see Gulyaev and Nesterov 1992).

ACT—The ACT Reference Catalog (Urban *et al.* 1997).

GSC—The Guide Star Catalog (Lasker *et al.* 1990). The symbol "ns" accompanying a GSC reference implies that the entry is marked as a nonstellar object in the cited catalog.

A2.0—A Catalog of Astrometric Standards (Monet *et al.* 1998). There are rare cases where the star could be found only in the previous version of the catalog; they are marked as A1.0.

IRAS—The Infrared Astronomical Satellite Catalogue of Point Sources (Neugebauer *et al.* 1988). We used it only when it was impossible to identify a star with positional catalogs or to find a star at optical wavelengths and independently measure its coordinates.

For some 200 stars (1.8% of all the stars in the new version), we measured their coordinates using Digitized Sky Survey images, plates from various collections, or other images. In these cases, the source of coordinates is indicated as "GCVS authors." As a rule, we used A2.0 catalog stars as the reference stars in our measurements using the Digitized Sky Survey. The rectangular coordinates of stars were measured by an eye-pointing of the cursor at their photometric centers in commercially available image processing applications with a large magnification. The measurements were reduced by Turner's linear method. The accuracy of our measurements was typically about $0''.5$ both in right ascension and in declination. The coordinates taken from current astronomical periodicals are marked as "Literature."

We provide a portion (the first 20 stars) of the table vol1_pos.dat as a guide to its contents (Table 1).

The distribution of stars from the new GCVS version in the sources of their coordinates is shows in the figure; the sources IRAS, PPM, ACT, GCVS authors, and Literature were combined into a sector called "Others." The sector "Tyc2" also includes the rare cases of coordinates from the first version of the Tycho catalog (for the stars missing in the second version), and the sector "A2.0" includes the rare cases of coordinates from the first version of the corresponding US Naval Observatory catalog.

### *The Files* rem.txt *and* ref.txt

The list of remarks to volume I (rem.txt) includes information that supplements the main table for 2070 stars. In contrast to the printed bilingual version of the 4th GCVS edition (Kholopov *et al.* 1985–1988), all remarks in the file are given only in English and generally correspond to the English text of the remarks in the printed edition. The remarks contain, in particular, information on variable stars in double stars, on period variability, on secondary minima of eclipsing variables, and on proximity to star clusters and nebulae in the sky. For unique variable stars, the remarks give detailed descriptions of the variability pattern.

The preliminary version of bibliographic references (ref.txt) for volumes I–III of the 4th edition contains 10 200 references to the literature from the main table and remarks. All references in Cyrillic alphabet in the printed version were transliterated into the Latin alphabet in this file.

**Table 1.** A portion of the electronic table vol1_pos.dat

| GCVS | J2000.0 | p.m. (as/yr) | Epoch | Source |
|---|---|---|---|---|
| 010001 R And | 002401.95 +383437.3 | −0.016 −0.035 | 2000.0 | Hip |
| 010002 S And | 004243.1 +411605. : | | 1885.67 | Literature |
| 010003 T And | 002223.15 +265945.8 | −0.007 −0.003 | 2000.0 | Tyc2 |
| 010004 U And | 011529.74 +404307.7 | +0.014 −0.017 | 2000.0 | AC |
| 010005 V And | 005006.28 +353910.1 | −0.007 −0.007 | 2000.0 | NPM |
| 010006 W And | 021732.96 +441817.8 | −0.001 −0.003 | 2000.0 | Hip |
| 010007 X And | 001609.53 +470045.3 | −0.000 −0.000 | 2000.0 | NPM |
| 010008 Y And | 013936.90 +392034.7 | | 1982.802 | GSC |
| 010009 Z And | 233339.95 +484905.9 | −0.007 −0.006 | 2000.0 | Hip |
| 010010 RR And | 005123.32 +342236.8 | +0.011 +0.002 | 2000.0 | NPM |
| 010011 RS And | 235521.75 +483817.8 | +0.020 −0.012 | 2000.0 | Tyc2 |
| 010012 RT And | 231110.10 +530133.0 | −0.007 −0.021 | 2000.0 | Hip |
| 010013 RU And | 013836.30 +384013.5 | −0.004 +0.007 | 2000.0 | NPM |
| 010014 RV And | 021102.57 +485645.1 | +0.014 −0.002 | 2000.0 | Hip |
| 010015 RW And | 004718.92 +324108.8 | +0.011 +0.017 | 2000.0 | NPM |
| 010016 RX And | 010435.52 +411757.8 | +0.007 −0.025 | 2000.0 | NPM |
| 010017 RY And | 232037.51 +393713.9 | +0.002 −0.011 | 2000.0 | NPM |
| 010018 RZ And | 230930.04 +530239.8 | +0.004 +0.001 | 2000.0 | Hip |
| 010019 SS And | 231130.07 +525312.5 | −0.007 −0.004 | 2000.0 | Hip |
| 010020 ST And | 233845.14 +354621.2 | +0.002 −0.004 | 2000.0 | Hip |

## REMARKS ABOUT SOME STARS OF THE ELECTRONIC VERSION

Below, we give remarks pertaining to individual stars from volume I of the GCVS. We did not set the objective of listing in this paper all the complex cases we encountered during our work on the catalog. It seems to us that the examples collected in the remarks give an idea of the typical problems that the compilers of the catalog had to solve. The coordinates and identifications adopted for the stars described in the remarks are presented in Table 2.

**NP And**. The variable IV V122 discovered by Saha (1984) was erroneously labeled IV V108 in the discoverer's chart. The variable's coordinates presented in the same paper contradict the chart, pointing to a star of approximately the same brightness; its position relative to a brighter neighbor is symmetric with the variable. Our identification of NP And with GSC 2268.01354 corresponds to Saha's coordinates; a private communication from the author confirmed that the chart was erroneous.

**AX Aps and LV Aps**. The two stars are on the same chart with a small field of view published by the discoverer (Hoffmeister 1963). We failed to identify the chart with surrounding stars. A guess that the Mira variable LV Aps is identical to the infrared source IRAS 15 491−7353 enabled us to identify the chart with a star field 20′ south of the published position.

**CV Ara**. Two charts from the atlas of Tsesevich and Kazanasmas (1971) were used to identify the variable with two different stars of the USNO A1.0 catalog: the first and second of them better match the variable's brightness and color (for an RR Lyrae variable), respectively. The color of the first star in the USNO A2.0 catalog is much bluer than in A1.0 and does not contradict the possible identification. The first star (GSC 9052.00158) is closer to the discoverer's coordinates (Swope 1936); Lopez (1998) identified the variable with this star. We adopted the same identification, although the uncertainty remains.

**MX Ara**. In the GCVS, this star is assumed to be

**Table 2.** Examples of the coordinates and identifications for problem stars

| Star | $\alpha_{2000.0}$ | $\delta_{2000.0}$ | Epoch | $\mu_\alpha$ | $\mu_\delta$ | Source | Identifications |
|---|---|---|---|---|---|---|---|
| NP And | $00^h10^m39^s.84$ | $+34°06'55''.7$ | 1982.800 | – | – | GSC | GSC 2268.01354 |
| AX Aps | 15 55 09.19 | −74 02 23.4 | 1976.236 | – | – | A2.0 | |
| LV Aps | 15 55 01.76 | −74 02 28.8 | 1991.25 | – | – | Tyc2 | Tyc2 9272 1590 1; IRAS 15491−7353 |
| CV Ara | 17 13 17.13 | −61 12 28.4 | 1976.632 | – | – | GSC | GSC 9052.00158? |
| MX Ara | 17 22 09.78 | −59 40 21.4 | 1976.633 | – | – | A2.0 | |
| NZ Ara | 17 37 50.04 | −59 37 31.0 | 1975.450 | – | – | A2.0 | Uncertain identification |
| RR Cnc | 08 11 03.15 | +23 08 54.6 | 2000.0 | $-0''.008$ | $-0''.010$ | Tyc2 | Tyc2 1927 1971 1; GSC 1927.01961; IRAS 09080+2317 |
| V CMa | 06 43 40.70 | −31 46 56.5 | 2000.0 | +0.014 | −0.006 | Tyc2 | CoD−31°3607? Tyc2 7087 114 1; GSC 7087.00114; IRAS 06418−3143 |
| EV CMa | 07 19 34.07 | −19 48 08.3 | 1980.211 | – | – | A2.0 | |
| V535 Cen | 14 37 27.39 | −37 03 01.8 | 2000.0 | −0.022 | −0.027 | AC | GSC 7308.01701 |
| AV Cha | 12 37 09.08 | −77 18 17.7 | 1976.250 | – | – | A2.0 | IRAS 12338−7701 |
| SU Col | 05 07 47.05 | −33 51 54.5 | 2000.0 | +0.004 | −0.011 | Hip | HIP 23868; CoD−34°2083; GSC 7050.00299 |
| V359 CrA | 18 16 03.27 | −38 39 05.5 | 2000.0 | −0.011 | −0.006 | Tyc2 | V530 CrA; Tyc2 7900 2773 1; GSC 7900.02773 |

identical both to the variable HV 7632 (Shapley and Boyd 1937) and to the variable S 6161 (Hoffmeister 1963). At close coordinates, these stars had the same variability type, and Hoffmeister's chart did not contradict the description given by Shapley and Boyd (the northern preceding star of the pair varies). We adopted Hoffmeister's identification. It should be noted, however, that Tsesevich and Kazanasmas (1971) suggested another star, which is not in conflict with the description either.

**NZ Ara**. The chart of Tsesevich and Kazanasmas (1971) shows severe distortions. Our identification takes into account the coordinates, brightness, and the chart but is uncertain.

**RR Cnc**. The star is confidently identified with GSC 1927.01961. However, in the Tycho (ESA 1997) and Tycho-2 (Høg *et al.* 2000) catalogs, contrary to the declared preservation of the designations for GSC stars in the latter, the star number is Tyc 1927 1971 1.

**V CMa**. There is no finding chart. The first and second editions of the well-known reference book "Geschichte und Literatur..." (GuL; Müller and Hartwig 1918; Prager 1934) give conflicting and erroneous (in both cases) descriptions of the star's duplicity, which completely confuse the identification. The star was found on Harvard Observatory plates using the discoverer's (A. Cannon) notebooks, and its variability was confirmed.

**EV CMa**. The discoverer's chart (Van Hoof 1961) cannot be identified with the sky at the specified position. There is a blot at the place of the cited paper where the right ascension is given, suggesting a misprint. The star was found 9 min of time (approximately two degrees of arc) to the east from the previously adopted coordinates.

**WY Car**. An example of a problem case where the coordinates cannot yet be improved. (We did not include WY Car in the table.) The first edition of GuL reports that the star is missing from the CPD catalog, whereas the second edition of GuL identifies it with CoD−57°3577. This CoD star is almost certain to be identical to CPD−57°3969 and HD 303467, an F0-type star. This identification of the faint long-period (semiregular or Mira-type) variable WY Car is acceptable neither in brightness nor in spectral type and color. The possible candidates in a wide field have not yet been confirmed.

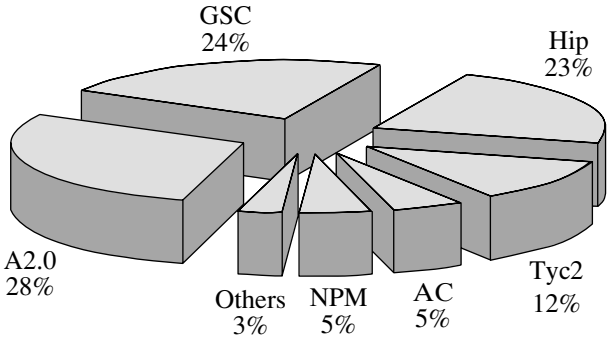


The sector diagram showing the distribution of stars from the new GCVS version in the sources of accurate coordinates.

**V535 Cen**. The choice between the two conflicting charts from the atlas of Tsesevich and Kazanasmas (1971) required a check in the Harvard Observatory plate stacks.

**AV Cha**. The chart from Hoffmeister (1963) allows the star to be identified with NSV 05771 (HV 8452 = 188.1933; Luyten 1933). Hoffmeister also noticed that the variable he discovered was close to Luyten's star but did not identify them because of the large error in his coordinates of AV Cha ($\sim 3'$ in declination).

**SU Col**. The GCVS gave an erroneous type for this variable, CWA, with a period of $21\overset{d}{.}55$, according to Avery and Sievers (1968). Actually, the star is an RR Lyrae variable with a period of $0\overset{d}{.}487$ (Gessner 1985). The chart in the cited paper by Avery and Sievers is also erroneous. However, the identification causes no difficulty, because accurate coordinates and the light curve can be found in the Hipparcos catalogue (ESA 1997).

**GT Com**. Schmeer (1999) found that this flare star could actually be the minor planet (679) Pax. We confirmed the object's motion among stars on the Maria Mitchell Observatory (USA) plates that were used by D. Hofleit to discover the variable object (Nygard 1973). The object was excluded from the GCVS as a nonexistent star; we did not include it in the table.

**V359 CrA and V530 CrA**. The coordinates of these stars published by their discoverers (Swope 1943; Kooreman 1966) differed by 1 min of time in right ascension and by 0.7 min of arc in declination. However, the chart for V359 CrA (Tsesevich and Kazanasmas 1971) pointed to the same star as Kooreman's chart for V530 CrA, with Kooreman's coordinates being approximately correct. Our confidence in the identification of the two variables stems from the fact that the epoch of minimum published by Swope for the first eclipsing variable does not contradict Kooreman's elements for the second one. The stars were declared identical in the new GCVS version.

## ACKNOWLEDGMENTS

We are grateful to A.A. Volchkov and J. Manek for providing us with the necessary software. We wish to thank S.V. Antipin for assistance, L.N. Berdnikov for providing unpublished finding charts for several southern Cepheids, C. Lopez (Argentina), N.T. Ashimbaeva, and G.V. Romanova for making their results available to us prior to their publication. We also wish to thank the researchers, primarily G. Williams (USA), who helped us to identify the "lost" variable stars using plates of other observatories. This study was supported in part by the Russian Foundation for Basic Research (project no. 99-02-16333), the Program of Support for Leading Scientific Schools of Russia (project no. 00-15-96627), the Federal Program "Astronomy," and the American Association of Variable Star Observers. We used the Digitized Sky Survey images provided by the Hubble Space Telescope Science Institute under support from grant NAG W-2166 of the USA Government.

## REFERENCES

1. R. Avery and J. Sievers, Veröff. Sternw. Bamberg. **7** (76), (1968).
2. H. Gessner, Inf. Bull. Var. Stars, No. 2795 (1985).
3. A. P. Gulyaev and N. T. Ashimbaeva, Astron. Zh. **74**, 249 (1997) [Astron. Rep. **41**, 215 (1997)].
4. C. Hoffmeister, Veröff. Sternwarte Sonneberg **6**, 1 (1963).
5. E. Høg, C. Fabricius, V. V. Makarov, *et al.*, *The Tycho-2 Catalogue,* CD-ROM (Copenhagen, 2000).
6. P. N. Kholopov, N. N. Samus', M. S. Frolov, V. P. Goranskiĭ, N. A. Gorynya, E. A. Karitskaya, E. V. Kazarovets, N. N. Kireeva, N. P. Kukarkina, N. E. Kurochkin, G. I. Medvedeva, N. B. Perova, A. S. Rastorguev, and S. Yu. Shugarov, *General Catalogue of Variable Stars* (Nauka, Moscow, 1985–1988), Vols. I–III.
7. P. N. Kholopov, N. N. Samus, N. M. Artiukhina, O. V. Durlevich, M. S. Frolov, V. P. Goranskij, N. A. Gorynya, E. A. Karitskaya, E. V. Kazarovets, N. N. Kireeva, N. P. Kukarkina, N. E. Kurochkin, N. A. Lipunova, G. I. Medvedeva, E. N. Pastukhova, N. B. Perova, A. S. Rastorguev, S. Yu. Shugarov, and T. M. Tsvetkova, Centre de Données Astronomiques de Strasbourg, II/214A (1998).
8. A. R. Klemola, R. B. Hanson, and B. F. Jones, Centre de Données Astronomiques de Strasbourg, I/199 (1987).
9. C. J. Kooreman, Ann. Sterrew. Leiden. **22**, 159 (1966).
10. B. M. Lasker, C. R. Sturch, B. J. McLean, *et al.*, Astron. J. **99**, 2019 (1990).

11. C. Lopez, private communication (1998).
12. W. J. Luyten, Astron. Nachr. **249**, 395 (1933).
13. D. Monet, A. Bird, B. Canzian, *et al.*, USNO-A V2.0. A Catalog of Astrometric Standards (US Naval Observatory, Washington, 1998), 11 CD ROMs.
14. G. Müller and E. Hartwig, *Geschichte und Literatur...* (Poeschel & Trepte, Leipzig, 1918), vol. 1.
15. G. Neugebauer, R. J. van Duinen, H. J. Habing, *et al.*, IRAS Point Source Catalog (NASA, Washington, 1988).
16. S. Nygard, J. Am. Assoc. Var. Stars Obs. **2**, 60 (1973).
17. *On the Four-Million Star Catalog,* Ed. by A. P. Gulyaev and V. V. Nesterov (Mosk. Gos. Univ., Moscow, 1992).
18. R. Prager, *Geschichte und Literatur des Lichtwechsels der Veränderlichen Sterne, 2. Ausgabe* (F. Dümmler, Berlin, 1934), vol. 1.
19. S. Röser, U. Bastian, L. I. Yagudin, and V. V. Nesterov, *PPM Star Catalogue. Positions and Proper Motions* (Astronomisches Rechen-Institut, Heidelberg, 1991–1993).
20. A. Saha, Astrophys. J. **283**, 580 (1984).
21. P. Schmeer, private communication (1999).
22. H. Shapley and C. D. Boyd, Ann. Harvard Obs. **105**, 243 (1937).
23. H. H. Swope, Ann. Harvard Obs. **90**, 207 (1936).
24. H. H. Swope, Ann. Harvard Obs. **109**, 41 (1943).
25. *The Hipparcos and Tycho Catalogues* (European Space Agency, 1997), ESA SP-1200.
26. V. P. Tsesevich and M. S. Kazanasmas, *Atlas of Finding Charts for Variable Stars* (Nauka, Moscow, 1971).
27. S. E. Urban, T. E. Corbin, and G. L. Wyckoff, *The ACT Reference Catalog* (US Naval Obs., Washington, 1997).
28. A. van Hoof, Publ. Louvain Obs., No. 126 (1961).
29. A. A. Volchkov and O. A. Volchkov, http://www.simfov.ru, 2001.

*Translated by N. Samus'*

*Astronomy Letters, Vol. 28, No. 3, 2002, pp. 182–186. Translated from Pis'ma v Astronomicheskiĭ Zhurnal, Vol. 28, No. 3, 2002, pp. 210–214.*


# Determining the Acceleration Height of the Electrons Responsible for Bremsstrahlung Gamma-Ray Bursts with Energies Above 10 MeV during the Solar Flares of April 2, 1982, and March 26, 1991

**Victoria G. Kurt[1] and V. V. Akimov[2,*]**

[1] *Institute of Nuclear Physics, Moscow State University, Vorob'evy gory, Moscow, 119899 Russia*
[2] *Space Research Institute, Russian Academy of Sciences, Profsoyuznaya ul. 84/32, Moscow, 117810 Russia*

Received October 22, 2001

**Abstract**—We determined the acceleration height of the electrons that produced short high-energy gamma-ray bursts with $E_\gamma > 10$ MeV during the development of the solar flares on March 26, 1991, and April 2, 1982. In both cases, the height was found to be $h_{\rm acc} < 4 \times 10^9$ cm. This result suggests that the low acceleration location is a typical and, possibly, necessary condition for electron acceleration up to tens and hundreds of MeV. We describe two different methods of height determination that are based on a multi-wave analysis of flares. © *2002 MAIK "Nauka/Interperiodica".*

Key words: *solar flares, particle acceleration, gamma-ray radiation, X-ray radiation, radio emission*

## INTRODUCTION

The height of electron acceleration in solar flares with high-energy gamma-ray radiation is one of the basic parameters required to construct models for electron acceleration to ultrarelativistic energies that are consistent with the experimental data obtained over the last decade. Our assertion (Kurt *et al.* 1996) that the gamma-ray radiation with energies 20–300 MeV during the flare of March 26, 1991, located near the solar-disk center (S28, W23) could be observed only if the particle acceleration took place in a region close to the chromosphere with a density $>10^{12}$ cm$^{-3}$, because the bremsstrahlung generated by ultrarelativistic electrons is highly beamed, served as the basis for this study. Is it accidental or can electrons be accelerated to high energies only in dense matter and in strong fields? How can we determine the height of electron acceleration accurately enough if we always see only the result of the interaction of accelerated electrons with matter or with the magnetic field of the solar atmosphere?

We determined this height both for the above flare of March 26, 1991, and for the flare of April 2, 1982, located far from the central meridian (W62, N09). During the flare of April 2, 1982, the gamma-ray radiation in the energy range 10–40 MeV had a bright impulsive phase $\sim$2 s in duration with a purely power-law energy spectrum without any admixture of line emission (Vestrand *et al.* 1999), while, during the flare of March 26, 1991, the gamma-ray burst in the energy range 20–300 MeV had a duration of $\sim$10 s. This burst also exhibited a power-law energy spectrum without any apparent admixture of photons from $\pi^0$-meson decay (Kurt *et al.* 1996; Akimov *et al.* 1993). The power-law energy spectrum recorded at the impulsive phase of these flares suggests that the gamma-ray radiation is the bremsstrahlung of high-energy electrons. We used the set of available experimental data to estimate the acceleration height during these two events by two different methods: (1) from the time of electron flight; and (2) by localizing the magnetic loop in which this acceleration took place.

## DETERMINING THE ACCELERATION HEIGHT FROM THE TIME OF ELECTRON FLIGHT

For the flare of April 2, 1982, we used a combination of the SMM gamma-ray ($\gamma$) and hard X-ray ($X$) measurements with the GRS and HXRBS instruments with data from the RSMN spectrometer (Nancey, France) in the meter radio band ($R$) in the frequency range 452–152 MHz. During the impulsive and main phases of the flare, chains of type-III radio bursts drifting downward in frequency were observed; most of them were detected beginning from the maximum available frequency of 452 MHz. In Newkirk's model of the solar atmosphere, the height of the radiation at this frequency is 150 000 km above

*E-mail: vakimov@space.ru

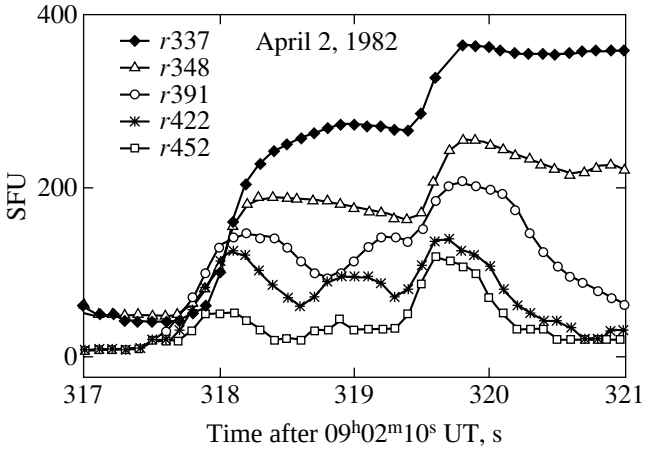


**Fig. 1.** Time dependence of the radio emission measured with the RSMN radio telescope in the frequency range 452–337 MHz.

the photosphere under the universally accepted assumption that it emerges at the second harmonic. Clearly, the electrons responsible for these type-III bursts were accelerated below this height.

To estimate the acceleration height more accurately, we used the following considerations. If the impulsively accelerated electrons move both upward and downward, then the upward flying electrons can generate a type-III burst, while the downward moving electrons, having reached the dense photospheric layers of matter, must generate an X-ray pulse. In this case, based on the dynamics of the type-III burst and on the generation time of the X-ray radiation, we can estimate the acceleration height above the photosphere.

If the emission height of the type-III burst depends linearly on time ($h_{\rm III} = h_0 + v_{\rm III} \times (t - t_0)$) and if the X-ray pulse is observed at time $t_X$, then we can determine the acceleration height as

$$h_{\rm acc} = (t_X - t_0 + h_0/v_{\rm III})/((1/k + 1)/v_{\rm III} + (1/k + 2)\cos\varphi/c), \quad (1)$$

where $c$ is the speed of light, $\varphi$ is the angle between the local vertical line and the line of sight (64° for this flare), $k = v_x/v$ is the ratio of the velocity of the X-ray-generating electrons to the true velocity of the electrons exciting plasma oscillations in the type-III source, $\{1/v = 1/v_{\rm III} + \cos\varphi/c\}$.

If the occurrence frequency of type-III bursts is high, then the X-ray burst cannot be uniquely identified with the corresponding type-III burst. Nevertheless, we managed to make such an identification for the two type-III bursts that emerged at the outset of the flare impulsive phase, precisely in the time interval when a short gamma-ray burst with energy 10–40 MeV was detected (319.5 s after $T_0 = 09^{\rm h}02^{\rm m}10^{\rm s}$ UT; in what follows, the time for this flare is measured from $T_0$).

Figure 1 shows the time dependence of meter-band radio emission for these type-III bursts. The X-ray bursts measured in the energy range 169–261 keV, together with the time dependence of the type-III burst generation height, are presented in Fig. 2.

The true velocities of the electrons generating the type-III bursts determined from the entire set of frequencies proved to be identical for both bursts, 123 000 km $s^{-1}$, i.e., $0.41c$. This is the maximum $v$ of all the values that we determined for 30 type-III bursts during this flare.

Figure 3 shows the distribution of all 30 bursts in true electron velocity. Most of the bursts have $v$ in the range 0.2–0.3 $c$, and only two of them fell within the last interval.

Since the electrons producing bremsstrahlung in the energy range 169–261 keV have velocities of $\sim 0.7\,c$, we took $k$ in formula (1) to be 1.7. It should be

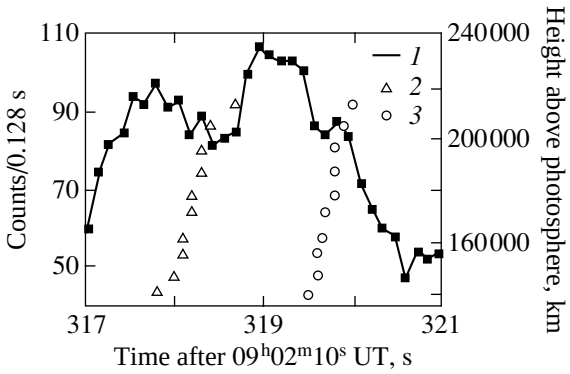


**Fig. 2.** Time dependence of the X-ray radiation in the energy range 169–261 keV measured with the HXRBS instrument onboard the SMM satellite (*1*) and the peak heights of two type-III bursts measured at different frequencies (*2* and *3*).

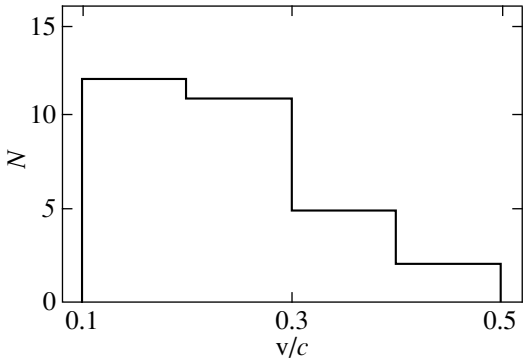


**Fig. 3.** The distribution of the type-III bursts measured during the development of the flare on April 2, 1982, in electron beam velocity.

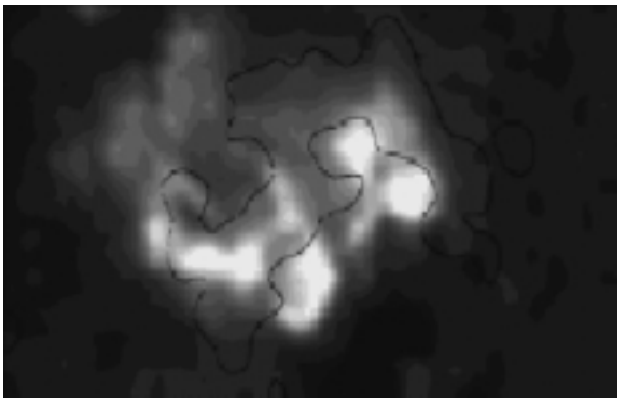

**Fig. 4.** The H$\alpha$ image for the flare of March 26, 1991, obtained with the Marshall Space Flight Center Telescope at $20^h29^m00^s$ UT.

noted that the estimate of $h_{acc}$ depends weakly on the adopted $k$, changing by less than 10% as $k$ changes from 1 to 2, and that the main uncertainties in the estimate of $h_{acc}$ result from errors in the type-III burst dynamics and in the position of the X-ray peak.

Taking all the possible uncertainties into account, we calculated the values

$$h_{acc} = (40–60) \times 10^3 \text{ km}$$

and

$$h_{acc} = (20–40) \times 10^3 \text{ km}$$

for the first and second acceleration pulses, respectively.

An important point is that during the second acceleration episode associated with a high-energy gamma-ray burst, the acceleration height was so small.

## DETERMINING THE ELECTRON ACCELERATION HEIGHT BY LOCALIZING THE MAGNETIC LOOP IN WHICH THIS ACCELERATION TAKES PLACE

The density in the region of electron acceleration to ultrarelativistic energies during the flare of March 26, 1991, was estimated to be $>10^{12}$ cm$^{-3}$ (Kurt *et al.* 1996). We assumed that such a low location of the acceleration region could result in local heating of the photosphere and in local brightening of the H$\alpha$ emission.

The H$\alpha$ intensity curves were obtained as follows. The MSFC (Marshall Space Flight Center) telescope image of the active region at the H$\alpha$ line center was recorded on video tape. Having compared the H$\alpha$ emission configuration with the magnetogram of the active region obtained with a magnetograph aligned with the optical telescope, we chose the 14 zones that mostly corresponded to crowdings of magnetic field lines on the photospheric surface. For each of the zones, we derived the time dependence of brightness with a time resolution of 0.27 s. This procedure of obtaining the intensity curves was described in detail by Kurt *et al.* (2000).

The optical image of the flare obtained immediately after the gamma-ray burst at $20^h29^m00^s$ UT, the map of the vertical magnetic-field component, and the arrangement of the zones of interest on this map are shown in Figs. 4 and 5.

To make the logic of our subsequent analysis clearer, we recall that the H$\alpha$ emission is secondary in its nature; it is produced in the cool dense matter of the solar atmosphere by heating when additional energy from upper layers is injected into it. We follow

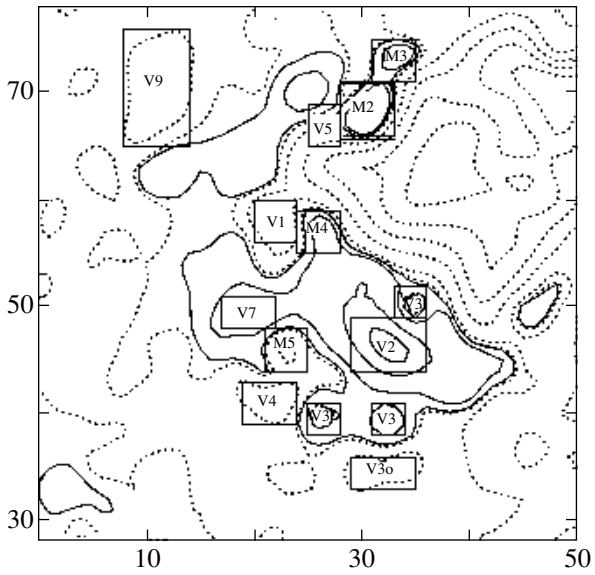


**Fig. 5.** The magnetic map obtained with the Marshall Space Flight Center magnetograph and the locations of 14 selected H$\alpha$ emission zones.

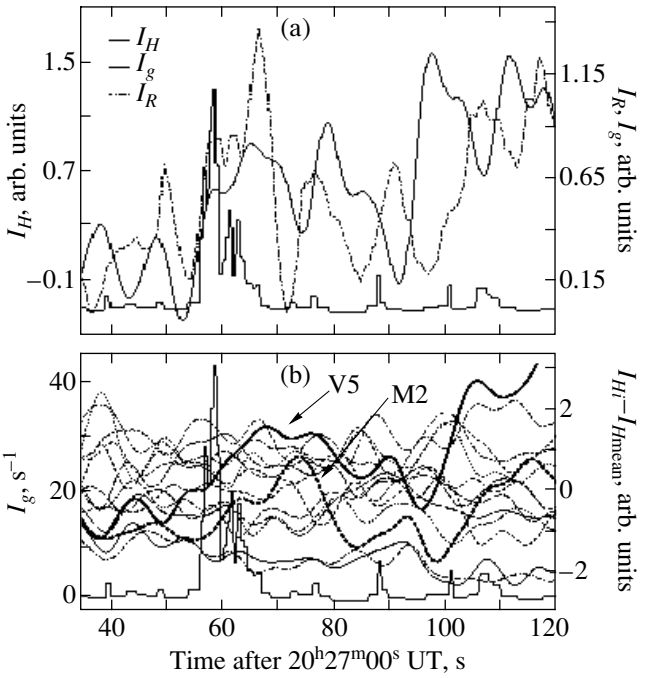


**Fig. 6.** (a) Time dependence of the gamma-ray burst with $E_\gamma > 20$ MeV and the injection functions for the microwave and H$\alpha$ emissions for the entire radiation region and the microwave radiation. (b) Time dependence of the gamma-ray burst with $E_\gamma > 20$ MeV and the injection functions for the H$\alpha$ emission for 14 zones.

the viewpoint of Kiplinger *et al.* (1990) and consider a short time scale of intensity variations as an indicator of the penetration of accelerated charged particles into small-area chromospheric regions at the feet of magnetic flux tubes and the total H$\alpha$ radiation intensity of each of the 14 regions as a measure of the energy injected into this region.

In our analysis, we compared the time dependences of the functions of energy injection into various types of flare emissions instead of comparing the intensity curves commonly used in most studies involving a comprehensive analysis of solar flare dynamics.

We found the injection functions by assuming that each type of emission had its own dissipation time $\tau_k$ and that the total energy $F_k(t)$ contained in the source of this emission was related to the injection function $I_k(t)$ by the following differential equation:

$$dF_k(t)/dt = I_k(t) - F_k(t)/\tau_k. \qquad (2)$$

As a measure of the energy $F_k(t)$ contained in the source of gamma-ray ($\gamma$), radio ($R$), and H$\alpha$ emissions, we used their measured intensities. The high-frequency fluctuations in H$\alpha$ emission were smoothed by calculating moving averages. Having numerically solved Eq. (2), for each type of emission, we found the maximum value of $\tau_k$ at which the injection function remains positive in the entire time interval analyzed. The values of $\tau_k$ obtained for the $R$ and H$\alpha$ emissions using this criterion are 12 and 60 s, respectively. Since the decay time scale of the gamma-ray intensity in the burst is shorter than 0.5 s (Akimov *et al.* 1993), we set $\tau_\gamma = 0$, implying the absence of any capture of the electrons generating gamma-ray radiation. In other words, the intensity of the gamma-ray radiation matches its injection function.

Next, we compared the time dependence of the gamma-ray radiation with those of the injection functions for other kinds of emissions.

The time dependence of the recorded gamma-ray flux with energies >20 MeV at the impulsive phase of the flare is indicated in Fig. 6 by the solid line.

The injection functions for the H$\alpha$ (averaged over all 14 zones) and $R$ emissions derived by the method described above are indicated in the upper panel of the figure by the dotted and dashed lines, respectively. The leading front of the main gamma-ray burst at 20$^h$27$^m$58$^s$ UT coincides with the leading fronts of the injections into the other two types of emission. Moreover, the double-peak gamma-ray pulse structure appears to be also reflected in the shape of these injection functions. This coincidence definitely suggests that the energy was injected into all three types of emission by the electrons accelerated in the same acts.

We investigated all 14 H$\alpha$ emission regions to find a pronounced injection of energy into them during

the gamma-ray pulse. The lower panel in Fig. 6 shows deviations of each injection function from the injection function averaged over all zones. Among all the zones, there were only two, V5 and M2, in which we see a pronounced injection during the gamma-ray pulse. The curves of the injection functions for these two zones are drawn by heavy lines. These two closely spaced zones are separated by less than $10^9$ cm and correspond to regions of strong magnetic fields with different polarities (see Fig. 5). In other words, the energy release took place in the low magnetic loop located near the foot of a dark filament. Thus, we may conclude that the acceleration of the electrons responsible for gamma-ray radiation with energies 20–300 MeV took place in this low loop or resulted from the interaction of this loop with another loop at a height of $\leq 10^9$ cm. If this is the case, then the plasma density at the top of this loop can exceed $10^{12}$ cm$^{-3}$.

## CONCLUSIONS

Using two different methods, we have found that the acceleration heights during the episodes of electron acceleration to energies 10–300 MeV do not exceed $4 \times 10^9$ cm. This suggests that a low location of the acceleration region is typical of electron acceleration to ultrarelativistic energies.

## ACKNOWLEDGMENTS

We wish to thank E.L. Chupp, B. Dennis, E. Rieger, P. Preka-Papadema, and A. Hillaris for providing detailed data on the gamma-ray, X-ray and radio emissions for the flare of April 2, 1981. We are also grateful to M.J. Hagyard and D.H. Hathaway for the joint work on flare of March 26, 1991.

## REFERENCES

1. V. V. Akimov, N. G. Leikov, V. G. Kurt, and I. M. Chertok, AIP Conf. Proc. **294**, 130 (1994).
2. A. L. Kiplinger *et al.*, in *Workshop #3 Max'91/SMM Solar Flares: Observations and Theory, Estes Park, Colorado, 1990,* Ed. by R. M. Winglee and L. Kiplinger, p. 210.
3. V. G. Kurt, V. V. Akimov, and N. G. Leikov, AIP Conf. Proc. **374**, 237 (1996).
4. V. G. Kurt, V. V. Akimov, M. J. Hagyard, and D. H. Hathaway, in *High Energy Solar Physics Workshop—Anticipating HESSI, College Park, Mariland, 2000,* Ed. by R. Ramaty and N. Mandzhavidze, Astron. Soc. Pac. Conf. Ser. **206**, 426 (2000).
5. W. T. Vestrand, G. H. Share, R. J. Murphy, *et al.*, Astrophys. J., Suppl. Ser. **120**, 409 (1999).

*Translated by G. Rudnitskii*

*Astronomy Letters, Vol. 28, No. 3, 2002, pp. 187–194. Translated from Pis'ma v Astronomicheskiĭ Zhurnal, Vol. 28, No. 3, 2002, pp. 215–223.*


# Interaction of Acoustic Oscillations with an Active Region on the Sun

**O. V. Ladenkov*, Sh. S. Kholikov, and Sh. A. Egamberdiev**

*Astronomical Institute, Academy of Sciences of Uzbekistan,*
*Astronomicheskaya ul. 33, Tashkent, 700052 Uzbekistan*

Received July 24, 2001; in final form, October 29, 2001

**Abstract**—Based on MDI data, we constructed acoustic maps of the high-degree solar oscillations as they interacted with the active region NOAA 7978 using the acoustic imaging technique. We analyze the reconstructed power maps for the incoming and outgoing oscillations, as well as the phase-shift maps and the envelope-shift maps of wave packets in the frequency range 3.0–5.0 mHz. We perform a cross-correlation analysis of the time series for the acoustic oscillations before and after their interaction with the active region and analyze direct observational data. Our results point to a difference between the phase and envelope shifts. Thus, for example, the phase and group velocities of the oscillations increase as they pass through a sunspot, with the increase in group velocity being more significant. We found a phase-shift difference between the inward and outward propagating oscillations, ~0.4–0.5 min. This difference is interpreted as the effect of subsurface flow from the active region. © *2002 MAIK "Nauka/Interperiodica".*

Key words: *Sun, acoustic oscillations, active regions*

## INTRODUCTION

The acoustic imaging technique was developed by Chang *et al.* (1997) and Braun *et al.* (1998) and is currently used to study the spatial distribution of acoustic signals on the Sun. This technique is a means of reconstructing the acoustic signal on the surface or in the interior of the Sun at any time based on observed acoustic signals. Acoustic waves are always present on the Sun, being stochastically generated by turbulent convection in the upper convection zone. Subsequently, after the emergence of an acoustic signal, the waves propagate deep into the Sun, gradually bend their trajectory because of the increase in the speed of sound with depth, and begin to return to the solar surface at some depth called the lower turning point. After a lapse of time and at certain distances from the point of wave generation, we can again observe the same acoustic signal, but it has already interacted with the solar interior matter along its propagation path and carries information on this interaction. The relationship between these time delays and the corresponding distances from the point of signal generation is called the time–distance relation. For the quiet Sun, this relation is relatively stable and is used in the acoustic imaging technique to reconstruct the acoustic signals at the point of their generation, or at the so-called target point. If the acoustic signals are reconstructed for the entire set of points, then we can obtain the reconstructed acoustic signals for a particular region. To accumulate information, the initial signal generation time is also sequentially shifted in time. Thus, we obtain the reconstructed time series of acoustic oscillations for the chosen points on the solar surface. Waves propagate differently in the quiet Sun and in active regions, because the physical parameters of the matter are different in them; this difference clearly shows up on acoustic images (see Fig. 3). Acoustic images can be constructed from several characteristics of the reconstructed oscillation time series. If the oscillation amplitudes are squared and summed, then we obtain the oscillation power. If the wave phase is used, then we obtain phase-shift ($\tau_{\rm ph}$) maps. The parameter $\tau_{\rm ph}$ is the time difference between points with corresponding phases in two oscillation series. In this way, we can also construct the envelope-shift ($\tau_{\rm env}$) maps of wave groups; $\tau_{\rm env}$ is the time shift of the wave-packet centers in two oscillation series from each other. In the acoustic imaging technique, the acoustic signal that emerged from some target point is reconstructed as completely as possible both by azimuthal averaging and by summing the signal being reconstructed in a wide spatial–temporal range, or in the so-called aperture. The aperture is the range for the time–distance relation used to reconstruct the acoustic signal. We can visualize the reconstructed acoustic signals in accordance with direct observational data from various parameters, both on the surface and at various depths where the local oscillation modes penetrate. The acoustic imaging

*E-mail: oleg@astrin.uzsci.net

technique is closely related to the method of time–distance analysis (Duvall *et al.* 1993). In the latter method, the signal is not reconstructed but only a cross-correlation analysis is performed between the various spatial–temporal elements of the observational data, which can be individual data elements and be grouped by azimuthal averaging. The result is a bivariate cross-correlation function, and the time–distance curve is constructed from the maximum of its values. The behavior of this curve tells us about the properties of the matter in the wave propagation regions and about the influence of local solar inhomogeneities on the passage of acoustic signals. Although the results are presented in different forms, the two methods yields similar $\tau_{\rm ph}$ and $\tau_{\rm env}$. However, for acoustic imaging, these quantities are averaged over the aperture or over some chosen range for the time–distance relation, while in time–distance analysis, these are determined for each time–distance step. The measured phase shifts $\tau_{\rm ph}$ and envelope shifts of wave packets $\tau_{\rm env}$ in active regions relative to those in quiet regions have previously been studied both by acoustic imaging (Chou *et al.* 2000) and by time–distance analysis (Braun 1997). However, the results of these two studies differ. Thus, for example, Braun (1997) obtained much smaller $\tau_{\rm env}$, while $\tau_{\rm ph}$ is only slightly smaller than that in Chou *et al.* (2000). Thus, one of our goals is to independently measure $\tau_{\rm ph}$ and $\tau_{\rm env}$ for a sunspot relative to their values in quiet regions on the Sun. The helioseismic methods are also widely used to investigate the subsurface flows and, in particular, the flows near active regions, where the inhomogeneity of the medium produced by strong magnetic fields changes abruptly the dynamics of motions characteristic of the quiet Sun. Time–distance analysis revealed that the travel time of the acoustic waves emerging from active regions decreases compared to that for quiet regions on the Sun and to the waves entering active regions (Duvall *et al.* 1996). This result was interpreted as a consequence of the existence of outflows from sunspots with a velocity of 2 km $s^{-1}$. However, it is believed that the absorption of p-modes by sunspots can also change the travel time of acoustic oscillations (Woodard 1997). To explore this issue, we reconstructed the time series for the acoustic oscillations entering and exiting of active regions. We assume that the matter moves radially with respect to the sunspot, and, consequently, the velocity introduced by this flow into the wave velocity will have opposite signs, along and against the wave propagation. Thus, this component can be separated out, which we did here. All our results were obtained for a set of frequencies in the range 3.0–5.0 mHz in order to determine how the interaction of acoustic oscillations with active regions depends on the frequency.

## OBSERVATIONS AND DATA ANALYSIS

We used data from the MDI/SoHO helioseismological instrument (Scherrer *et al.* 1995), which are minutely Dopplerograms of the entire solar disk in the Ni I 6768 Å line. For our analysis, we chose a $150 \times 125$-pixel area of the active region NOAA 7978, which roughly corresponds to $34 \times 28$ heliographic degrees, as the target region. A 1024-min-long series with a filling factor of 100% was used for acoustic imaging. Below, we present the acoustic imaging steps.

First, the data were remapped onto a latitude–longitude coordinate grid followed by their correction for solar rotation. At this step, we used the GRASP IRAF software package. After the operations were complete, the spatial resolution was $0\overset{\circ}{.}175$ in longitude and 0.0019 rad in colatitude.

The next step of our preliminary data reduction involved temporal filtering with a Gaussian window centered at the frequencies 3.0, 3.5, 4.0, 4.5, and 5.0 mHz with a FWHM of 1.0 mHz for all points of the chosen $400 \times 400$-pixel surface area. The region size exceeded the size of the target region, because points outside the latter were used at the next (azimuthal averaging) step.

To reconstruct the acoustic signal exiting or entering the target region, we performed a phase summation. Since the passage time of the mode between its sequential appearances on the surface depends on the angular distance from the target point, the signals at an angular distance $\Delta$ from the target point are azimuthally averaged to obtain the azimuthally averaged amplitude $\Psi(\Delta, t)$. The signal generated at the target point at time $t$ can be reconstructed by summing the azimuthally averaged amplitudes at various angular distances from the target point measured with the corresponding time delays based on the time–distance relation (Fig. 1). We used an aperture of 2–13 heliographic degrees, which corresponds to 30–62 min of the wave-packet passage between their sequential appearances on the visible photospheric surface. The signal reconstructed at the target point at time $t$ can be determined from the relation

$$\Psi_c(t) = \sum_{\tau=\tau_1}^{\tau_2} W\Psi(\Delta, t+\tau), \qquad (1)$$

where $\Psi(\Delta, t+\tau)$ is the azimuthally averaged signal at distance $\Delta$ from the target point at time $t+\tau$. The summation variable changes uniformly at 1-min intervals in the range $(\tau_1, \tau_2)$, which is (30 min, 62 min) in our case. The factor $W \propto (\sin\Delta/\tau^2)^{1/2}$ is the weighting function that allows for the wave-packet smearing with increasing distance. For a polytropic atmosphere, the relation $(\sin\Delta/\tau^2)^{1/2} \propto$

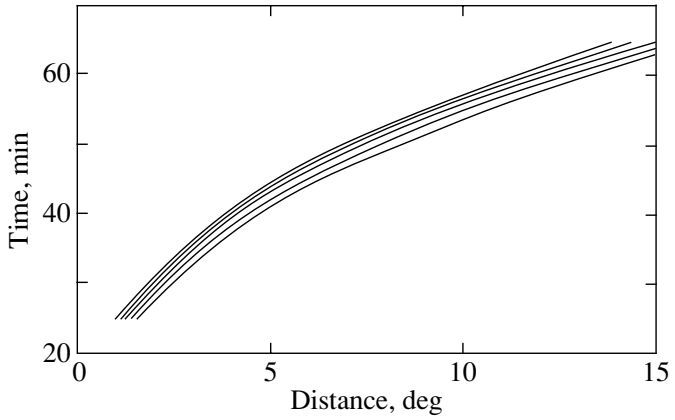


**Fig. 1.** Time–distance relations for the frequencies 3.0, 3.5, 4.0, 4.5, and 5.0 mHz (from top to bottom).

$(\sin\Delta/\Delta)^{1/2}$ holds (Chou *et al.* 1999). The time–distance relations for the incoming waves were derived by a mirror reflection of the relation for the outgowing waves relative to the spatial axis, i.e., by multiplying the time in the time–distance relation for the outgoing waves by $-1$. The range of mode degrees from 380 to 120 corresponds to this spatial aperture.

The azimuthal averaging and summation of the values obtained in the aperture range were repeated for all 1024 time steps of the observational series both to reconstruct the spatial–temporal series for the acoustic oscillations that go out of the target region and, consequently, that have interacted with the active region and quiet regions and for the acoustic signals that have not yet passed through the target region or come into it. To obtain the reconstructed power maps of acoustic oscillations, the amplitude determined at the previous step after the summation for each time step was squared and summed over the time.

The reconstructed time series that represent two $150 \times 125 \times 1024$-element arrays were used to perform a cross-correlation analysis on an element-by-element basis. The reconstructed and observed time series used in this analysis have the same duration, although a longer data series was taken for the summation procedures in accordance with the time delays derived from the time–distance relation. The normalized degree of cross-corelation was determined from the formula

$$C_n(t) = \frac{C(t)}{\sigma_{\rm in}\sigma_{\rm out}}, \qquad (2)$$

where the cross-correlation function $C(t)$ was calculated using the Wiener–Khintchin relations as an inverse Fourier transform of the spectral density function; the latter, in turn, can be calculated as the product of the Fourier transform of one series and the complex conjugate of the other series (Bendat and Piersol 1986):

$$C(t) = IFT[\Psi_{\rm in}(f)\Psi_{\rm out} \times (f)]. \qquad (3)$$

The quantities $\sigma_{\rm in}$ and $\sigma_{\rm out}$, in turn, represent the square roots of the variances of the series used in our analysis, in our case, for the reconstructed incoming and outgoing ones, respectively. These can be determined as follows:

$$\sigma = \sqrt{\frac{1}{N}\sum_{i=1}^{N}(\Psi_i - \overline{\Psi})^2}, \qquad (4)$$

where $\overline{\Psi}$ is the mean value of the series, and $N$ is the number of points in the series.

The degree of correlation is an important parameter indicating that the observed and reconstructed signals belong to the same wave packets. The degree of correlation depends on frequency; in particular, it is at a maximum for 3.0 mHz, $\sim$70%. As the frequency increases, the correlation decreases and becomes, on average, $\sim$40% for 5.0 mHz. The fairly high correlation between the reconstructed and observed signals, which occasionally reaches 80–85%, suggests a high degree of coherence between the reconstructed and observed series; this provides evidence that these series belong to the same wave packet.

The derived cross-correlation curves were fitted by the nonlinear least squares method using the Gabor function

$$G(t) = A\cos(2\pi\nu[t - \tau_{\rm ph}])e^{-[t-\tau_{\rm env}]/2\sigma^2}. \qquad (5)$$

As the sought-for parameters, we used the following: correlation amplitude $A$, oscillation frequency $\nu$, phase shift $\tau_{\rm ph}$, envelope-peak shift of wave groups or Gaussian peak $\tau_{\rm env}$, and Gaussian width $\sigma$. Such an analysis was performed for all spatial points of the reconstructed and observed time series. Figure 2 shows portions of the reconstructed time series

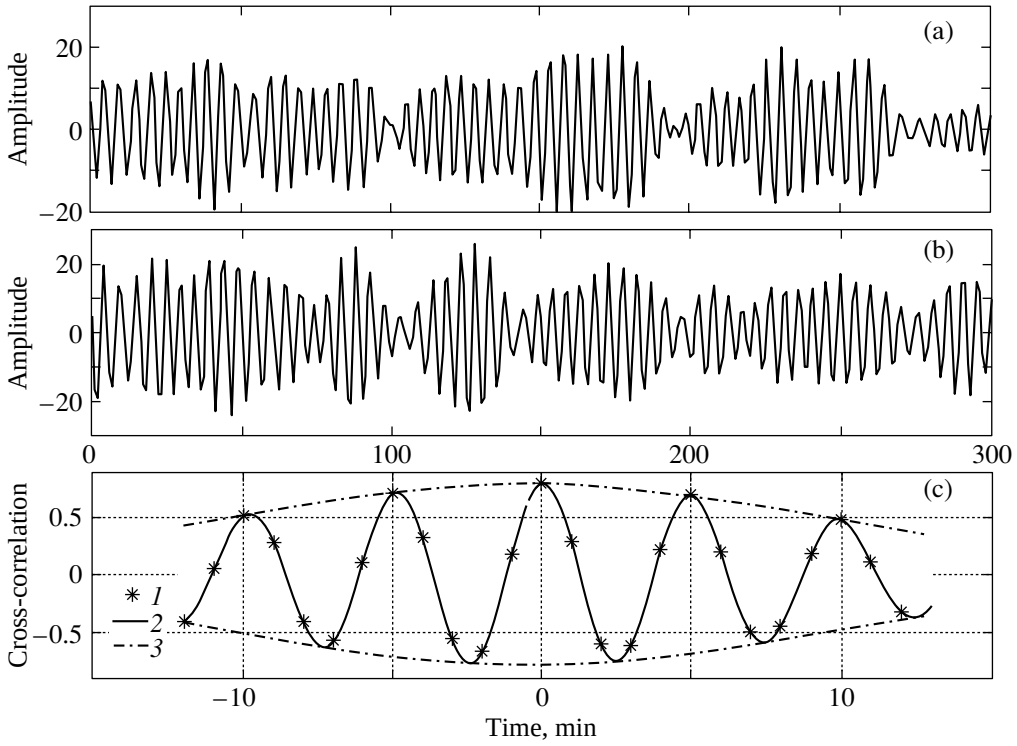


**Fig. 2.** Portions of the reconstructed time series for the (a) outgoing and (b) incoming signals at an arbitrarily chosen point in the target region. (*1*) Indicates the cross-correlation function (c) between these series. *2*—the fitting Gabor function (c); *3*—the Gaussian component of the Gabor function, whose maximum is interpreted as the center of the wave packet and its shift is $\tau_{\rm env}$.

for the outgoing and incoming signals at an arbitrarily chosen point in the target region of duration ~300 min (a, b); in panel (c), the asterisks indicate the cross-correlation function between these series. The degree of correlation between these complete 1024-min-long series is 76.5%.

As a result, we obtained the maps of $\tau_{\rm ph}$ and $\tau_{\rm env}$ between the reconstructed series of the incoming and outgoing signals for the frequencies 3.0, 3.5, 4.0, 4.5, and 5.0 mHz, as shown in Fig. 3. We also obtained two sets of maps for $\tau_{\rm ph}$ and $\tau_{\rm env}$ between the observed series and the reconstructed time series of the incoming and outgoing signals.

To make sure that the time–distance relations used here correspond to those of acoustic oscillations in our data and that they do not introduce any systematic shifts, we constructed the cross-correlation functions by time–distance analysis (Duvall *et al.* 1993). These bivariate cross-correlation functions were fitted by the Gabor function, and the relations between the derived time delays $\tau_{\rm env}$ and the distance were interpreted as the time–distance relations in acoustic imaging. Since the calculated and tabulated time–distance relations were similar, the tabulated data could be used for our data series. Figure 1 shows time–distance relations for the solar surface at various frequencies.

## RESULTS

The columns in Fig. 3 (from left to right) present the following: power maps of the observed acoustic oscillations, reconstructed power maps of the outgoing oscillations, and phase-shift and envelope-shift maps at various frequencies. We do not show power maps for the incoming waves, because these are only flat areas with the fluctuating values attributable to noise without any features on the surface, because these oscillations have not yet interacted with sunspots. Each power map in Fig. 3 was normalized to the intrinsic mean intensity of the quiet Sun, and the intensity scale is the same for each column. We see from the figure that the phase-shift maps correlate well with features on the observed power maps. The reconstructed power maps of the outgoing waves also exhibit major features of the active region, but these are slightly blurred against the fluctuating noise background. The worst correlation is observed for the envelope-shift maps of wave groups, because of the large variance of the results. The envelope shifts of wave groups in the active region for 5.0 mHz relative

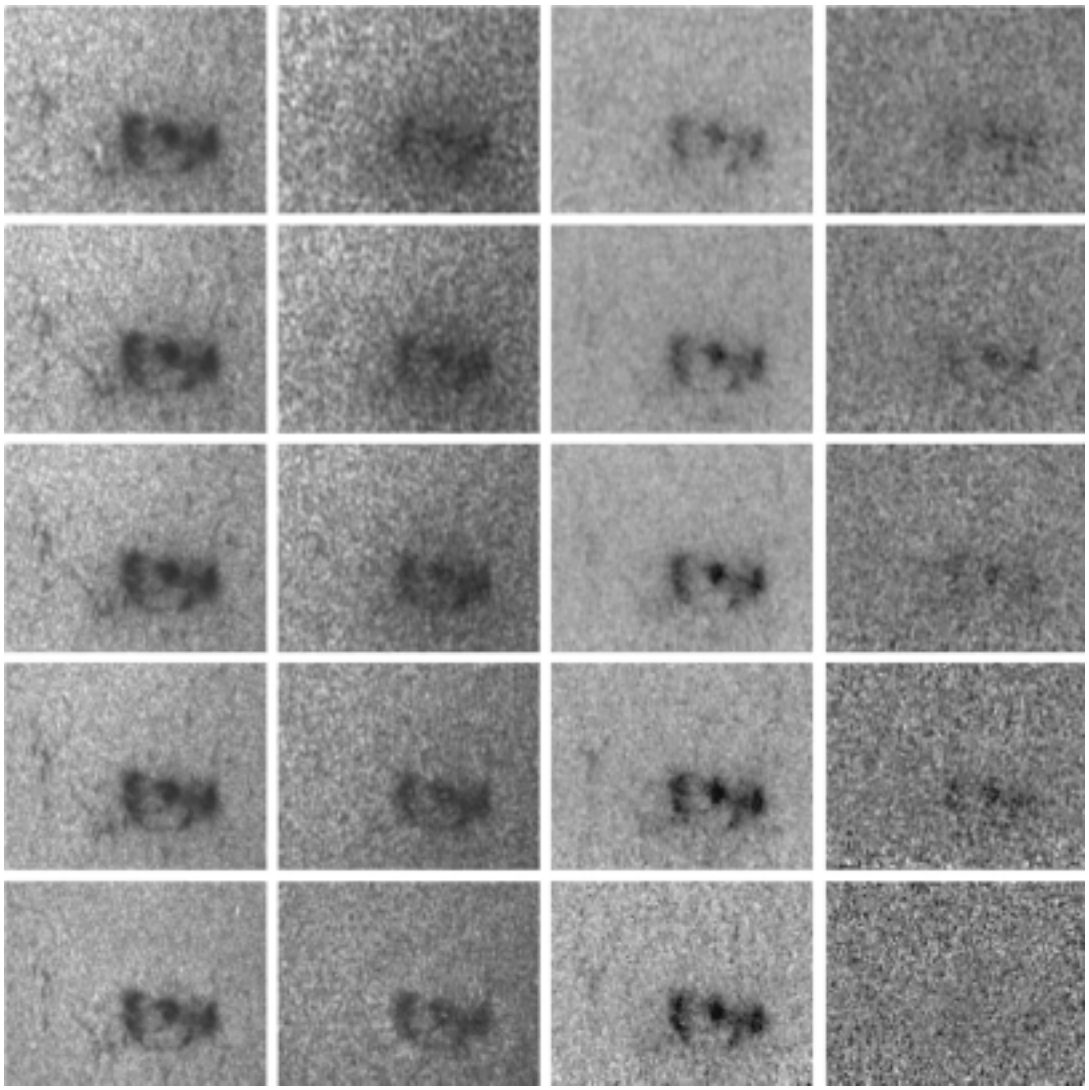

**Fig. 3.** Maps of the active region NOAA 7978 for various frequencies (from top to bottom): 3.0, 3.5, 4.0, 4.5, and 5.0 mHz. The columns from left to right are: acoustic power maps of direct observational data, reconstructed acoustic power for the outgoing oscillations, phase-shift maps, and envelope-shift maps of wave groups.

to the quiet Sun are virtually lost in the surrounding noise. On the phase-shift and envelope-shift maps, the dark areas at the sunspot locations correspond to negative shifts of the phase and envelope travel times; i.e., the speed of sound increases inside the active region. A different interpretation is also possible: the propagation path of the wave front decreases. This fact is widely known: the visible surface in the region of sunspots lies deeper than that of the quiet Sun (the so-called Wilson effect), but it cannot explain the behavior of $\tau_{\rm ph}$ and $\tau_{\rm env}$ in full measure (Chou *et al.* 2000). In Fig. 4, the phase and envelope shifts inside the active region, more specifically in the central region of a large sunspot, are plotted against frequency; the mean phase and envelope shifts in the region of the quiet Sun were first subtracted from the corresponding values inside the sunspot. It follows from the figure that $\tau_{\rm ph}$ are smaller than $\tau_{\rm env}$. The errors for each value in the plot are the standard deviations when calculating the mean. As we see, $\tau_{\rm ph}$ is determined with an accuracy that is an order of magnitude lower than that for $\tau_{\rm env}$. The difference between the phase and envelope shifts is approximately constant, being about 2.5–3.0 min. However, the envelope time for 5.0 mHz drops to a low value, thereby violating the derived relationship. This is because the result for this frequency is very noisy, which complicates the fitting of the cross-correlation function and may lead to an erroneous result. The acoustic signal is rather weak at the frequency 5.0 mHz, because this range lies near the acoustic cutoff frequency estimated at 5.3–5.5 mHz.

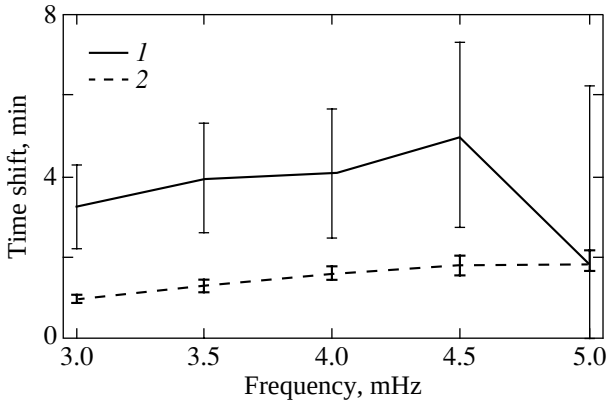


**Fig. 4.** Frequency dependence of the phase shifts between the reconstructed time series coming into and going out of the sunspot relative to the quiet Sun (*2*); (*1*) a similar dependence for the wave group envelope.

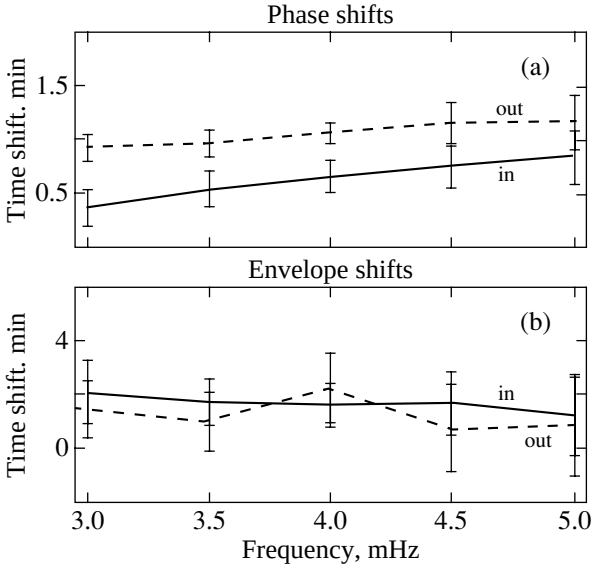


**Fig. 5.** (a) Phase shifts between the observed and reconstructed time series going out of the sunspot ("out") and between the reconstructed incoming and observed series ("in"); (b) the same shifts for the wave group envelope.

These results are in good agreement with previous studies (Chou *et al.* 2000), despite some differences both in the duration of our series and in the aperture.

In our analysis of the frequency dependence of the phase and envelope shifts, we estimated these shifts between the reconstructed incoming and outgoing time series. However, we can investigate this dependence of the same wave series by analyzing the cross-correlation functions between the reconstructed incoming and observed series and between the reconstructed outgoing and observed series. The derived shifts must add up to the value obtained by analyzing the incoming and outgoing time series. Figure 5 shows $\tau_{\rm ph}$ and $\tau_{\rm env}$ for the same region as that used previously but for the incoming and observed series and, separately, for the outgoing and observed series. We see that $\tau_{\rm ph}$ for the incoming waves are smaller than those for the outgoing waves. This result has already been obtained previously (Duvall *et al.* 1996; Braun 1997) using time–distance analysis. The existence of outflows from the sunspot region is mainly responsible for the asymmetry between the outgoing and incoming times series of acoustic signals, causing an increase in the phase velocity for the outgoing signal and its corresponding decrease for the incoming signal. If the phase time for the outgoing and incoming signals are written as $dph_{\rm out} = ph_{\rm qs} - ph_{\rm flow}$ and $dph_{\rm in} = ph_{\rm qs} + ph_{\rm flow}$, respectively, then subtracting one from the other yields

$$ph_{\rm flow} = (dph_{\rm in} - dph_{\rm out})/2, \qquad (6)$$

where $ph_{\rm flow}$ is the time phase shift caused by the factor with a radial direction (toward or away from the sunspot); in our case, we assume that this is a flow of matter moving away from the sunspot; $ph_{\rm qs}$ is the phase shift caused by the factors that do not depend on the signal propagation direction. These factors imply the following: the phase changes at the interfaces between the media with different parameters, as, for example, at the upper turning point or at the boundaries of magnetic flux tubes, and the accumulation of phase changes during the passage inside the Sun, where the sound-speed, density, and temperature distributions are radially stratified. Figure 6a shows the frequency dependence of the difference calculated from formula (6) and of the sum $ph_{\rm qs} = dph_{\rm in} + dph_{\rm out}$, which is compared with the values calculated between the incoming and outgoing series. We see from a comparison of these two plots that they are in good agreement, within the error limits, but there is a small ($\sim$0.1 min) systematic shift. This shift may stem from the fact that when analyzing the phase shifts between the incoming, observed, and outgoing time series, we calculated the phase shift at the upper turning point in the observed series twice, while in our study of the phase shifts between the incoming and outgoing series, this effect arises once. It is possible that in this way, we can directly calculate the phase shift produced by the reflection at the upper turning point.

The results on phase shifts are in good agreement with one of the previous studies (Chou *et al.* 2000) but slightly differ from the other, earlier study (Braun 1997), being nevertheless within the error limits. Figure 6 also shows the frequency dependence of the phase shifts calculated from formula (6). The outflow of matter from the sunspot may be responsible for such shifts. The frequency dependence indicates an almost linear decrease in the phase shifts at $\sim$1.5 min

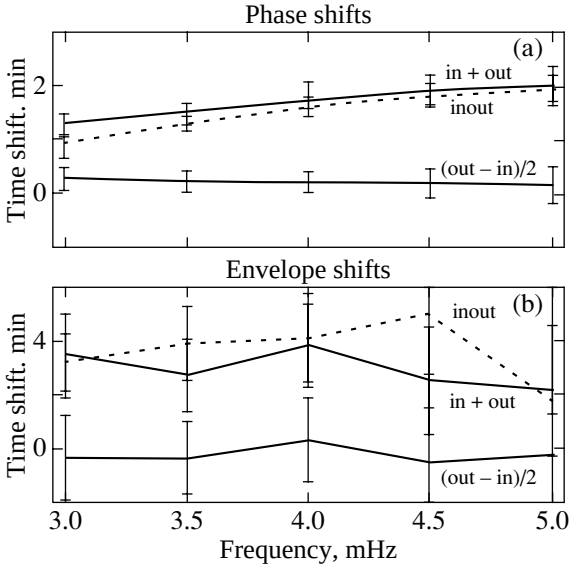


**Fig. 6.** (a) The sum of phase shifts "in + out" derived by analyzing them between the incoming and observed time series and between the observed and outgoing series; "inout"—between the incoming and outgoing series (dashed line), "(out − in)/2"—half the difference between the phase shifts between the outgoing and observed series ("out") and between the incoming and observed series ("in"); (b) the same for the envelope shifts of wave groups.

in the interval 1.5–3 min. This trend may stem from the fact that the time interval used in azimuthal averaging is constant for various frequencies, resulting in a displacement of the range of mode degrees used because of the difference between the time–distance relations. Thus, for high frequencies, we use lower-order modes, i.e., the modes that penetrate into deeper solar layers. Consequently, we may conclude that the flows from the sunspot are subsurface ones or at least decay with depth. The study by Duvall *et al.* (1996), who suggested the existence of flows with $\sim$2 km s$^{-1}$ in the upper zone 2000 km in depth, may serve as a confirmation of this result, while the inversion procedures (Kosovichev 1996) point to the existence of flows from the sunspot at depths up to 20 Mm.

As regards the study of the envelope shift, unfortunately, the accuracy in determining this parameter is too low to draw definitive conclusions. Nevertheless, from Fig. 6b, we can see variations of this parameter with frequency, both when analyzing the shifts between the incoming and outgoing series and when using direct observational data. The sum of the shifts between the reconstructed incoming and observed data and between the reconstructed outgoing and observed data is shown in Fig. 6. We see that although its behavior is fairly stable, it nevertheless corresponds, within the error limits, to its value calculated between the reconstructed incoming and outgoing time series. This result differs markedly from that (Braun 1997) for two active regions, where the total shift was $\sim$2 min, but close to the result obtained by the same author for the third active region NOAA 7912, $\sim$3.6 min. The difference between these two shifts calculated in the same way as that for the phase shifts (6) is also shown in Fig. 6. This parameter is seen to be unstable, fluctuating about its zero level.

## CONCLUSIONS

We have shown that high-degree acoustic oscillations provide information on their interaction with the solar interior matter along the path of their propagation. Several points that arise during the interaction of acoustic waves with the inhomogeneities of the medium attributable to the influence of strong sunspot magnetic fields may be noted.

(1) The phase shifts $\tau_{\rm ph}$ and the envelope shifts $\tau_{\rm env}$ of wave groups behave differently during the interaction with sunspots. In the sunspot matter, the speed of acoustic waves increases and, consequently, results in a negative time shift relative to the quiet Sun both for the phase and for the wave envelope. However, these shifts differ in magnitude. The phase shifts $\tau_{\rm ph}$ have values from $\sim$1 min for 3.0 mHz and linearly increase to 2 min for 5 mHz, while $\tau_{\rm env}$ ranges from 3.5 min for 3 mHz to 5 min for 4.5 mHz (Fig. 4).

(2) The difference between $\tau_{\rm ph}$ and $\tau_{\rm env}$ changes little with frequency, being $\sim$2.5–3.0 min, despite the large range of errors typical of the estimated position and time delay of the wave packet due to its smearing in space. Such a constancy suggests a low dispersiveness of the solar interior matter, including that inside sunspots (Fig. 4).

(3) The amplitude of the oscillations as they pass through sunspots decreases sharply. As a result, the oscillation power in the sunspot region for the reconstructed outgoing waves is $\sim$40–50% of the quiet-Sun level (Fig. 2).

(4) An analysis of the phase shifts between the reconstructed incoming and observed times series and between the observed and outgoing time series indicates that these shifts are not equivalent. Thus, whereas for the outging oscillations, the phase shift lies in the range 0.9–1.3 min, for the oscillations propagating toward the sunspot, this shift is 0.35–0.85 min, depending on frequency. This fact can be explained by the interaction of the flow propagating radially away from the sunspot. The effect of the flow on the phase shifts is estimated to be 0.3 min for 3 mHz, gradually decreasing to 0.15 min for 5 mHz (Figs. 5, 6).

(5) The envelope travel time is virtually unaffected by the presumed flow from the sunspot. This is quite strange, although it is confirmed by previous studies (Braun 1997) (Fig. 6).

(6) There is a systematic displacement between the calculated phase shift between the incoming wave series and the series exiting the sunspot and its value obtained by adding up the calculated phase shifts between the incoming and observed series and between the observed and outgoing series. This displacement is ~0.1 min. The following interpretation is possible: during the addition of the phases, the phase shift in the observed series is added twice, while the phase shift calculated without involving the direct observational series occurs once (Fig. 6).

## ACKNOWLEDGMENTS

This study was supported in part by the INTAS grant no. 97-31198. We wish to thank D.-Y. Chou for providing the data and for consultations and the GONG team for the GRASP software package. We are grateful to A. V. Serebryanskii for helpful discussions.

## REFERENCES

1. J. Bendat and A. Piersol, *Random Data. Analysis and Measurement Procedures* (Wiley, New York, 1986; Mir, Moscow, 1989).
2. D. C. Braun, Astrophys. J. **487**, 447 (1997).
3. D. C. Braun, C. Lindsey, Y. Fan, and M. Fagan, Astrophys. J. **502**, 968 (1998).
4. H.-K. Chang, D.-Y. Chou, B. LaBonte, and Team TON, Nature **389**, 825 (1997).
5. D.-Y. Chou, H.-K. Chang, M.-T. Sun, *et al.*, Astrophys. J. **514**, 979 (1999).
6. D.-Y. Chou, M.-T. Sun, and H.-K. Chang, Astrophys. J. **532**, 622 (2000).
7. T. L. Duvall, Jr., Nature **300**, 242 (1982).
8. T. L. Duvall, Jr., S. M. Jefferies, J. W. Harvey, and M. A. Pomerantz, Nature **362**, 430 (1993).
9. T. L. Duvall, Jr., S. D'Silva, S. M. Jefferies, *et al.*, Nature **379**, 235 (1996).
10. A. G. Kosovichev, Astrophys. J. Lett. **461**, L55 (1996).
11. P. H. Scherrer, R. S. Bogart, *et al.*, Sol. Phys. **162**, 129 (1995).
12. M. F. Woodard, Astrophys. J. **485**, 890 (1997).

*Translated by V. Astakhov*

*Astronomy Letters, Vol. 28, No. 3, 2002, pp. 195–198. Translated from Pis'ma v Astronomicheskiĭ Zhurnal, Vol. 28, No. 3, 2002, pp. 224–227.*


# The Formation of Radio Brightening Bands Near Cool Filaments on the Sun

**I. A. Bilenko[1,2] and V. A. Kovalev[2,*]**

[1] *Sternberg Astronomical Institute, Universitetskii pr. 13, Moscow, 119899 Russia*
[2] *Institute of Terrestrial Magnetism, Ionosphere and Radiowave Propagation, Russian Academy of Sciences, Troitsk, 142092 Russia*

Received August 17, 2001

**Abstract**—We analyze the spatial distribution of the intensity of radio emission from a cool filament in terms of the generalized Kippenhahn–Schluter model. Based on a numerical calculation of the centimeter radio emission and using the temperature transition layer model by Anzer and Heinzel (1999), we show that two symmetric brightening bands must be observed near the filament. The absence of any bands during observations with a sufficient angular resolution suggests that a different type of model is realized: a model with a narrow (unobservable) temperature transition layer across a magnetic field, in particular, a Kuperus–Raadu-type model. © *2002 MAIK "Nauka/Interperiodica"*.

Key words: *Sun, cool filaments, temperature transition layer, radio emission, brightening*

## INTRODUCTION

As yet, there is no certainty in the model of cool filaments (prominences) on the Sun. There are two types of magnetostatic models. In the model of Kippenhahn and Schluter (1957) (KS), the cool filament material is supported in the corona by the Lorentz force. In the model of Kuperus and Raadu (1974) (KR), the filament equilibrium is maintained by the repulsion of the currents flowing in the filament and in the photosphere. Is it possible to determine from observations what type of model is realized? We will attempt to positively answer this question by invoking radio-astronomical studies of filaments. The models under discussion significantly differ by the structure of the magnetic field and filament–corona temperature transition region. The KS model is characterized by open magnetic field lines, resulting in a spatially extended temperature transition layer because of the high electron heat conductivity along the field lines. The KR model has a cylindrical geometry with closed magnetic field lines. It is characterized by a reduced heat conductivity across the magnetic field and, accordingly, by a narrow temperature transition layer.

By analyzing the magnetostatic models of cool filaments with energy balance, we show that the models with open magnetic field lines are difficult to reconcile with observations of the radio frequency spectra for filaments. The observed spectra more likely suggest a reduced plasma heat conductivity in the filament–corona transition layer (Chiuderi and Chiuderi Drago 1991; Kovalev 1994). Filippov and Den (2000) drew attention to the difficulties in realizing the KS model, associated with its instability when limited in height.

Significant differences between the models can manifest themselves in the spatial distribution of microwave thermal emission, because it originates mainly in the region of transition temperatures, reaching a maximum at an optical depth of $\sim 1$. The KS model can lead to a radio brightening relative to the quiet Sun (Kovalev 1994).

The most consistent numerical calculations of the temperature transition region from a cool filament with $T = 8 \times 10^3$ K to the hot corona with $T = 10^6$ K at a constant gas pressure $P_0 = 0.02$ dyne cm$^{-2}$, $P_e = P_0/2.1$, in the generalized KS model with energy balance between the heat flux, radiative cooling, and heating were performed by Anzer and Heinzel (1999). The large width of the transition layer ($\sim 10^{10}$ cm) is attributable to the high electron heat conductivity (Fig. 1).

Here, we calculate the spatial radio-brightness distribution for the solar corona toward the disturbed

*E-mail: vkovalev@izmiran.troitsk.ru

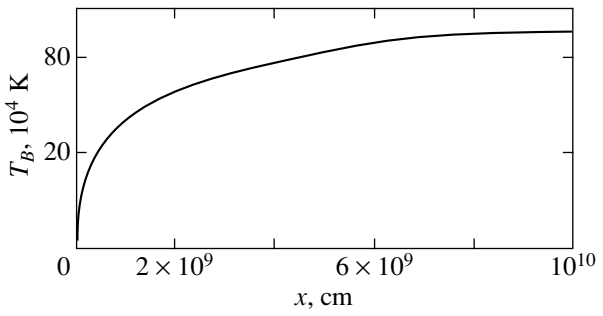


**Fig. 1.** The kinetic-temperature distribution in the cool filament–hot corona transition layer calculated by Anzer and Heinzel (1999) for the generalized KS model with energy balance.

region (across the transition-temperature layer adjacent to the filament) by using the results of Anzer and Heinzel (1999).

## CALCULATING THE RADIO EMISSION FROM A FILAMENT TRANSITION REGION

We assume the radio emission from the solar atmosphere in the presence of a filament to be produced by the corona, the disturbed region, and the chromosphere. The radio brightness temperature is defined as

$$T_B = T_B^{\rm cor} + T_B^{\rm dis}\exp(-\tau^{\rm cor}) + T_B^{\rm ch}\exp(-\tau^{\rm dis}-\tau^{\rm cor}), \quad (1)$$

$$T_B^{\rm dis} = \int T\exp(-\tau)d\tau, \quad (2)$$

$$\tau = \int \mu\, ds. \quad (3)$$

The first term in Eq. (1) describes the coronal emission above the disturbed region, $T_B^{\rm cor}$; the second terms describes the intrinsic emission from the disturbed region, $T_B^{\rm dis}$, attenuated by absorption in the corona at its optical depth $\tau^{\rm cor}$; and the third term describes the chromospheric emission, $T_B^{\rm ch}$ (below the disturbed region), attenuated at the total optical depth of the disturbed region and corona $\tau^{\rm dis}+\tau^{\rm cor}$. The integration in Eqs. (2) and (3) is carried out along the radio path within the disturbed region. The value of $T_B^{\rm ch}$ can be obtained from the radio spectrum of the quiet Sun, $T_B^{\rm q}$, using the relation

$$T_B^{\rm q} = T_B^{\rm cor} + T_B^{\rm ch}\exp(-\tau^{\rm cor}). \quad (4)$$

The corresponding spectrum, $T_B^{\rm q}$, was taken from centimeter observations (Zirin *et al.* 1991).

The absorption coefficient is determined by electron–ion Coulomb collisions in a thermal plasma (Zheleznyakov 1977):

$$\mu \simeq 3.3\times10^{-23}\lambda^2 n^2 T^{-1.5}\Lambda/N. \quad (5)$$

Here, $\lambda$ is the wavelength in cm, $N$ is the refractive index (for an isotropic plasma, it is $\simeq$1), $n$ is the electron density, and $\Lambda$ is the Coulomb logarithm. Following Promesh Rao and Kundu (1977), we may assume that in the microwave range of interest, the corona above the filament is transparent ($\tau^{\rm cor}<1$) with an optical depth

$$\tau^{\rm cor} = 7.5\times10^{-5}\lambda^2\exp(-z/4)\sec\theta \quad (6)$$

and brightness temperature

$$T_B^{\rm cor} = T^{\rm cor}\tau^{\rm cor} \simeq 122\lambda^2\exp(-z/4)\sec\theta. \quad (7)$$

Here, $T^{\rm cor}$ is the kinetic temperature of the corona, $\theta$ is the heliolongitude, and $z$ is the filament height (measured in $10^9$ cm). Thus, the contribution of $T_B^{\rm ch}$ is significant when the disturbed region is transparent. The contribution of $T_B^{\rm cor}$ increases with wavelength and becomes significant in the decimeter range.

Figure 2a shows the calculated spatial distribution (on one side of the filament in the transverse direction) of radio brightness temperature at various wavelengths in the range 1.66–5.2-cm, and Fig. 2b shows the relative contrast $\Delta = T_B/T_B^{\rm q}-1$. We assume the filament to be at the solar-disk center: $\theta=0$. The disturbed region spans the height range $(1–3)\times10^9$ cm.

As long as $\tau>1$, the brightness temperature in the transition layer also rises with $T$, reaching a maximum at $\tau\sim1$. As the temperature rises further, the disturbed region becomes transparent: $\tau<1$, $T_B\simeq T\tau$. However, since the gas pressure is constant in the transition layer ($nT\simeq$ const), according to Eq. (5), $\tau\propto T^{-7/2}$, and, as $T$ increases, the contribution of the disturbed region to the emission decreases and the brightening effect is reduced, disappearing as the coronal temperature is reached in the transition layer.

The contrast in brightening at 5.2 cm reaches a maximum of 2.7 at a distance of 100 km from the filament edge. The contrast of the brightening band decreases with distance; however, an excess of $\sim$0.1 ($\sim$1590 K) above the level of the quiet Sun still takes place at a distance of $\sim4\times10^3$ km. The contrast in brightening decreases with decreasing wavelength. Because of the symmetry, the brightening takes place on both sides of the filament.

## CONCLUSIONS

Thus, our calculations of the radio brightness distribution in the vicinity of a cool filament for the generalized KS model using the parameters of the temperature transition region calculated by Anzer and Heinzel (1999) have shown that a brightening must take place in this model. The presence of an extended

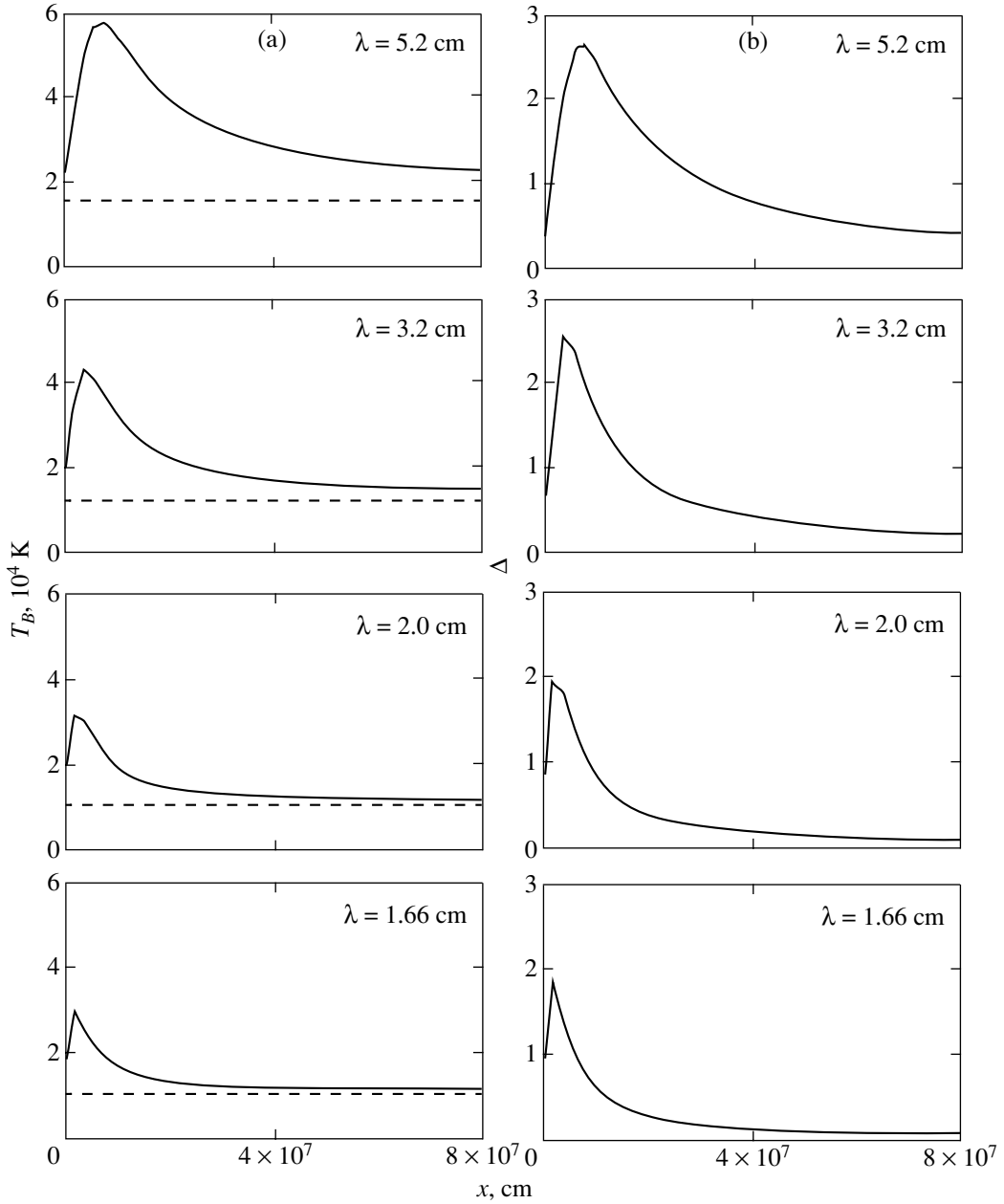


**Fig. 2.** (a) Radio brightness temperature (solid line) of the filament transition region at centimeter wavelengths (on one side of the filament in the transverse direction). The dashed line represents the temperature of the quiet corona $T_B^q$. (b) $\Delta = T_B/T_B^{\rm q} - 1$, which characterizes the brightening $\Delta > 0$ toward the filament–corona transition layer.

temperature transition region attributable to the high electron heat conductivity in this model results in a significant brightening relative to the microwave emission of the quiet corona. We showed that two symmetric brightening bands must be observed on both sides of the filament. This effect is observable with currently available instruments. It should be noted that we used the most stringent conditions on the parameters in our calculations: thus, the coronal plasma density ($\sim 10^8$ cm$^{-3}$) is one of the lowest in the existing models. An increase in the density of the disturbed region enhances the brightening effect. The presence of a rarefied cavity around the filament can move the band away from the filament. A preliminary analysis shows that allowance for the nonuniform plasma density distribution in height in the disturbed region allows a possible explanation of the occasion-

ally observed effect, the wavelength dependence of the ratio-filament width.

An observation of this effect would suggest that the KS model of the filament is realized. It is quite probable that the radio brightening bands observed by Zandanov *et al.* (2000) can be explained by the effect under discussion.

The absence of brightening in radio observations may suggest that other types of filament models (of KR type) with a narrow (virtually unobservable) temperature transition layer attributable to the reduced plasma heat conductivity across the magnetic field of the filament is realized.

Further progress in this work may be associated with an improvement of the model for the transition region. In particular, it is desirable to develop a model of greater dimensionality.

## ACKNOWLEDGMENTS

We are grateful to B.P. Filippov for the information on the literature and to U. Anzer, who provided data on the model of the filament transition region. One of the authors (V.A.K.) was supported by the Russian Foundation for Basic Research (project no. 99-02-16076).

## REFERENCES

1. U. Anzer and P. Heinzel, Astron. Astrophys. **349**, 974 (1999).
2. C. Chiuderi and F. Chiuderi Drago, Sol. Phys. **132**, 81 (1991).
3. B. P. Filippov and O. G. Den, Pis'ma Astron. Zh. **26**, 384 (2000) [Astron. Lett. **26**, 322 (2000)].
4. R. Kippenhahn and A. Schluter, Z. Astrophys. **43**, 36 (1957).
5. V. A. Kovalev, Pis'ma Astron. Zh. **20**, 603 (1994) [Astron. Lett. **20**, 512 (1994)].
6. M. Kuperus and M. A. Raadu, Astron. Astrophys. **31**, 189 (1974).
7. A. Promesh Rao and M. R. Kundu, Sol. Phys. **61**, 335 (1977).
8. V. G. Zandanov, S. V. Lesovoi, and A. M. Uralov, in *Proceedings of the International Conference on Solar Physics devoted Professor G. M. Nikol'skii "Structure and Dynamics of the Solar Corona," Troitsk, 1999* (2000), p. 236.
9. V. V. Zheleznyakov, *Electromagnetic Waves in Cosmic Plasma* (Nauka, Moscow, 1977), p. 268.
10. H. Zirin, B. M. Baumert, and G. J. Hurfort, Astrophys. J. **370**, 779 (1991).

*Translated by G. Rudnitskii*

*Astronomy Letters, Vol. 28, No. 3, 2002, pp. 199–205. Translated from Pis'ma v Astronomicheskiĭ Zhurnal, Vol. 28, No. 3, 2002, pp. 228–234.*


# Rotation Cycles of the Sector Structure of the Solar Magnetic Field and Its Activity

**V. V. Vasil'eva, V. I. Makarov*, and A. G. Tlatov**

*Pulkovo Astronomical Observatory, Russian Academy of Sciences, Pulkovskoe sh. 61, St. Petersburg, 196140 Russia*

Received August 14, 2001

**Abstract**—We study the rotation of the sector structure of the solar magnetic field by using Stanford magnetographic observations from 1975 until 2000 and magnetic synoptic H$\alpha$-maps obtained from 1904 until 2000. The two independent series of observations yielded the same rotation periods of the two-sector (26.86 days) and four-sector (13.64 days) structures. We introduce a new index of the solar rotation, $SSPM(t)$. The spectral power density of the sector structure of the magnetic field is shown to exhibit a 22-year cyclicity. The two- and four-sector structures of the magnetic field rotate faster at the maxima of even 11-year sunspot cycles. This phenomenon may be called the Gnevyshev–Ohl rule for the solar rotation. The 11-year sector-structure activity cycles are shown to lead the 11-year sunspot cycles (Wolf numbers) by 5.5 years. A 55-year component with the slowest rotation in the 18th cycle (1945–1955) was distinguished in the sector-structure rotation. © *2002 MAIK "Nauka/Interperiodica".*

Key words: *Sun, magnetic field, rotation*

## INTRODUCTION

Temporal variations in the solar and stellar rotation play an important role in the generation of magnetic fields and in the nature of solar–stellar cycles. The first attempts to identify variations in the solar rotation from sunspot tracers yielded contradictory results (Newton and Nunn 1951; Clark *et al.* 1979; Hanslmeier and Lüstig 1986). Nevertheless, a number of authors (Becker 1954; Camper 1957; Vitinskiĭ and Ikhsanov 1972) showed that the solar rotation rate changes from the maximum to the minimum of solar activity. Using several 11-year cycles as an example, Schröter and Wöll (1978), and Balthasar and Wöhl (1980) showed that the solar equator rotates slightly faster at the minimum of solar activity. The rotation rate in the preceding cycle was found to positively correlate with the maximum Wolf number of the succeeding cycle.

However, active regions are surface tracers, in contrast to the large-scale background magnetic fields that extend deep into the convection zone. The discovery of torsional oscillations (Howard and LaBonte 1980) and the sector structure of the interplanetary and photospheric magnetic fields (Wilcox and Svalgaard 1974; Wang and Sheeley 1994) stimulated further studies of the solar differential rotation. Coronal holes were found to rotate rigidly, and regions of fast and slow rotation drifting from high latitudes toward the equator were discovered.

After synoptic H$\alpha$-maps of the large-scale background solar magnetic field were made (Makarov 1983, 1984; Makarov and Sivaraman 1986, 1989; Obridko and Shelting 1999), it became possible to study the solar rotation and activity at all latitudes over a period of more than 100 years. Based on H$\alpha$-maps and polar solar activity, Makarov and Sivaraman (1983) analyzed the peculiarities of the sign reversal of the solar magnetic field, and Makarov and Makarova (1996) proved the existence of two types of activity on the Sun in the form of "butterflies" of polar faculae and spots separated in latitude by $\sim 40°$. A latitudinal drift of the regions of fast and slow rotation was investigated (Makarov and Tlatov 1997; Makarov *et al.* 1997, 1998), and a 55-year activity cycle was found in torsional oscillations (Makarov *et al.* 1997, 1998; Kitchatinov *et al.* 1999). The regions of slow rotation were shown to drift toward the equator along the butterflies of polar faculae and sunspots and, thus, link the high- and low-latitude solar activities (Makarov and Tlatov 1997; Makarov *et al.* 1997, 1998). Recently, H$\alpha$-maps have been used to analyze cyclic variations in the rotation of the two- and four-sector structures of the large-scale solar magnetic field (Obridko and Shelting 2000). It was shown that the rise in solar activity was accompanied by a decrease in the rotation rate and that the two-sector structure of the magnetic field prevailed.

*E-mail: makarov@gao.spb.ru

1063-7737/02/2803-0199$22.00 

Here, based on Hα-maps from 1904 until 2000, we continue to study the rotation of the two- and four-sector structures of the solar magnetic field in an effort to find quantitative relationships between the rotation rate of the magnetic field and its activity.

## OBSERVATIONAL DATA AND REDUCTION TECHNIQUES

The structure of the global solar magnetic field is known to be determined by the distribution of unipolar magnetic regions clearly seen on magnetograms. These unipolar regions are set off by the boundaries with a zero radial magnetic-field component (or neutral magnetic lines), which are traced by prominences and dark filaments seen at the center of the Hα line (Makarov 1983, 1984; Makarov and Sivaraman 1986, 1989; Obridko and Shelting 1999). The latitudinal–temporal distribution of neutral magnetic lines in one solar rotation produces a topological pattern of the polarity distribution of the global magnetic field, but these data carry no information on the magnetic-field strength. However, the latitudinal–temporal distribution of neutral magnetic lines shows the magnetic-field topology with a higher accuracy than can be obtained from magnetograms, particularly for a weak field and polar regions of the Sun (Duval *et al.* 1977).

It should be noted that the field topology is of greatest importance in studying the global activity in the large-scale (background) magnetic field (without the fields of active regions). Accordingly, when analyzing the field structure on Hα-maps, we may assign field strengths of +1 or −1 G to the regions of positive and negative magnetic-field polarity (e.g., with sizes $5^\circ \times 5^\circ$). As a result, we can produce series of magnetic-field strengths at all latitudes.

Here, we investigate the solar rotation at latitudes within ±20° of the equator. On each map, we calculated $\alpha = (S_+ - S_-)/(S_+ + S_-)$, where $S_+$ and $S_-$ are the respective areas of the regions of positive and negative magnetic-field polarity, in a rectangle 20° in latitude and 10° in longitude. The complete $\alpha(t)$ series for the period from 1904 until 2000 consists of 46 400 values. We performed a spectral analysis of the entire series by using a fast Fourier transform, in which we calculated the coefficients $a_n$ and $b_n$ in the series expansion $\alpha(t) = \sum a_n \cos(wnt) + b_n \sin(wnt)$. The power of the identified period was determined by the sum $(a^*a + b^*b)$. We analyzed the rotation of the sector structure using 1024- and 2048-wide windows, in units of 10° in longitude. For example, for the four-sector structure, the longitude range 10° corresponds to the time interval $dt = 0.757647$ days, and the 2048-wide window corresponds to 1552 days, or 4.25 years. Under these conditions, in the interval from 13 to 14 days, there are 136 periods calculated as $T = dt \times 32768/l$, where $l$ is an integer in the range 1773 to 1909. For this window, we can calculate the total power of all peaks or their envelopes in the spectrum for the chosen range of periods, $SSPM = \sum(a^*a + b^*b)$. The procedure can be repeated after shifting the window to the next step. We obtained $SSPM$ for various window positions from 1906 until 1998. The behavior of $SSPM$ is cyclic, and it can be compared with the behavior of the Wolf numbers. This reduction technique is justified by the use of other (autoregression and covariance) methods of spectral analysis and by checking the results for other sampling windows.

## RESULTS

### *Rotation of the Two- and Four-Sector Structures of the Solar Magnetic Field during 1975–2000*

To compare and correlate the data obtained from magnetic Hα-maps with magnetographic observations, we reduced the Stanford magnetic-field observations and the magnetic-field observations based on Hα-maps for the period from 1975 until 2000. Figure 1 shows the power spectra for the rotation periods of the two- and four-sector structures of the solar magnetic field as constructed from (a) the Stanford observational data and (b) from the Hα-maps at latitudes within ±20° of the equator. The identity of the spectra and their fine structure are seen. The two independent 25-year-long series of observations give a discrepancy within ±0.005 days, or ∼7 min, which is within the measurement accuracy. We see that from 1975 until 2000, the large-scale solar magnetic field was dominated by the two-sector structure (Obridko and Shelting 2000). The fundamental synodic rotation periods over the last 25 years were 13.64 and 26.86 days for the four- and two-sector structures, respectively. Based on these data, we may assume that the four-sector structure of the solar magnetic field is not a harmonic of the two-sector structure, as was already noted by Obridko and Shelting (2000). In addition, a comparison of the two independent series shows that the series of magnetic Hα-maps can be used to study the solar rotation over a longer period.

### *Peculiarities of the Solar Rotation from 1904 until 2000*

A sufficiently long series of synoptic magnetic Hα-maps allows the long-term variations in solar rotation to be analyzed at various epochs of solar cyclicity. Here, we performed a spectral analysis of the series of Hα maps with an ∼1 month-long window. Figure 2 shows the power spectra for the rotation periods of the sector structure of the solar

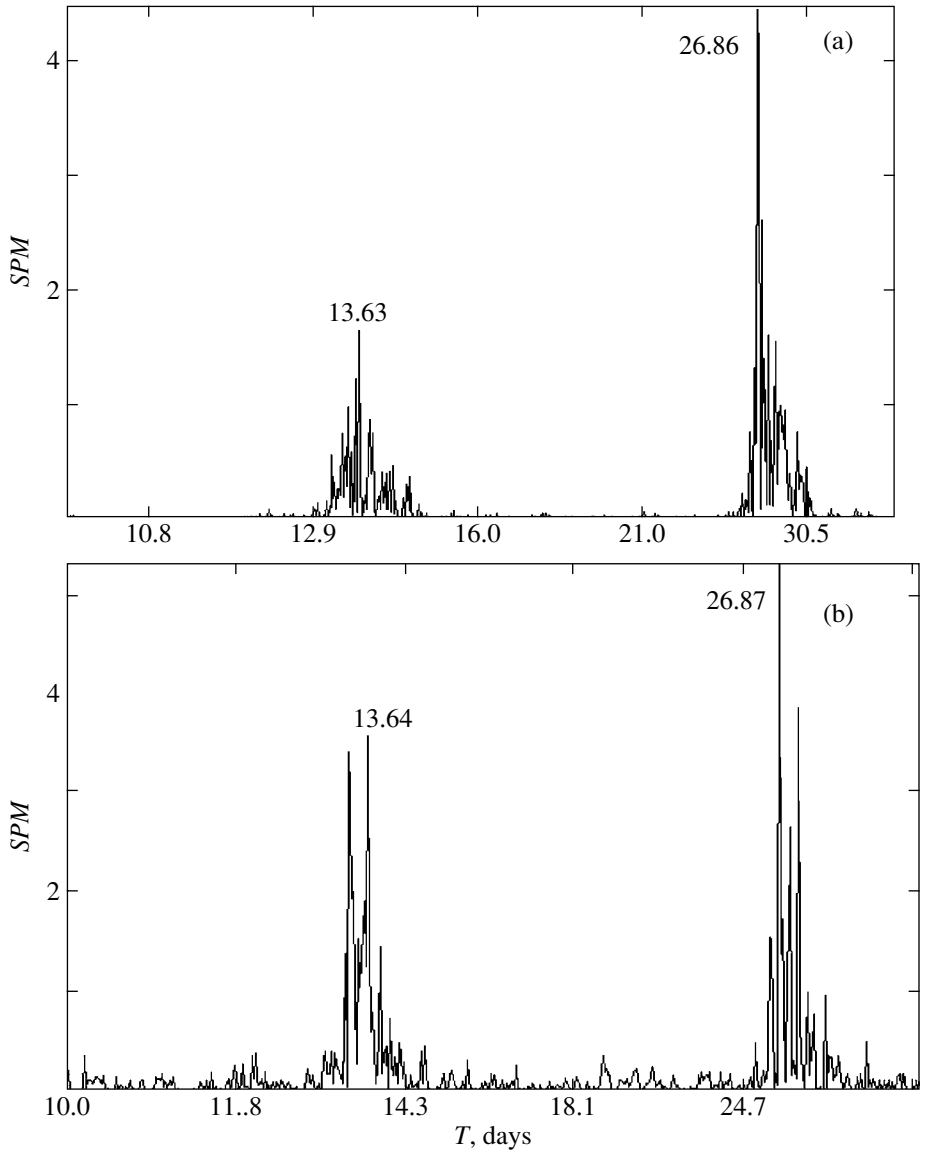


**Fig. 1.** Power spectra for the rotation of the solar magnetic field at latitudes ±20° in the range of periods from 10 to 40 days. Two- and four-sector structures of the solar magnetic field can be distinguished (a) from the Stanford observations and (b) from the magnetic Hα-maps for the period from 1975 until 2000.

magnetic field from 1904 until 2000. Apart from the two-sector (27.01 days) and four-sector (13.55 days) structures, a six-sector structure with a rotation period of ~9.0 days can be identified, particularly at the maximum of the 11-year cycle. However, it is not yet clear whether this structure of the solar magnetic field is an independent formation or a harmonic of the two-sector structure.

Figure 3 shows temporal variations in the rotation periods of the (a) four- and (b) two-sector structures of the solar magnetic field from 1904 until 2000. We see that the rotation period of the four-sector structure contains a 22-year magnetic cycle of solar activity. The rotation rate of the sector structure varies with cycle phase, reaching 3% of its mean value. The fastest rotation of the four-sector structure (with a period of ~13.45 days) was observed at the maxima of even (22, 20, 18, 16, and 14) 11-year cycles, according to the Zurich classification. The slowest rotation (with a period of ~13.7 days) was observed at the maxima of mostly odd cycles. The slowed rotation is particularly clear in cycle 18 (from 1945 until 1955), which is probably attributable to the high activity of the solar magnetic field during this period. It should be noted that the acceleration in solar rotation at the minimum of solar activity has been repeatedly pointed out by many authors, and this may be considered to be a well-established fact (Makarov and Tlatov 1997,

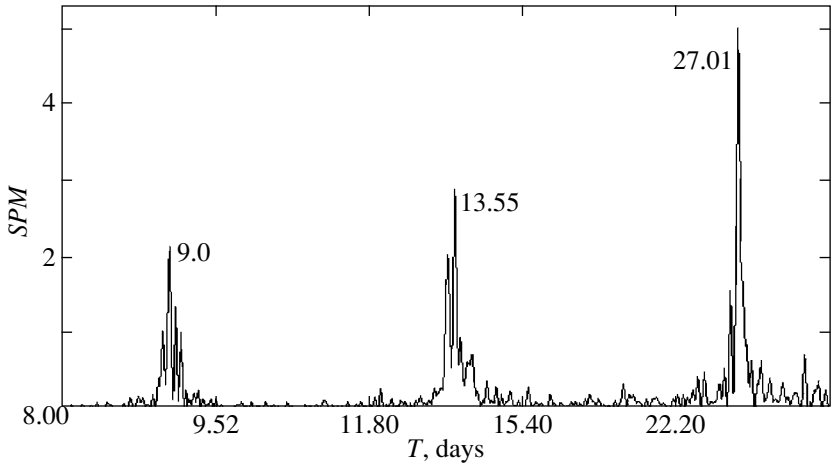


**Fig. 2.** Rotation periods of the sector structure of the solar magnetic field at latitudes ±20° from 1904 until 2000.

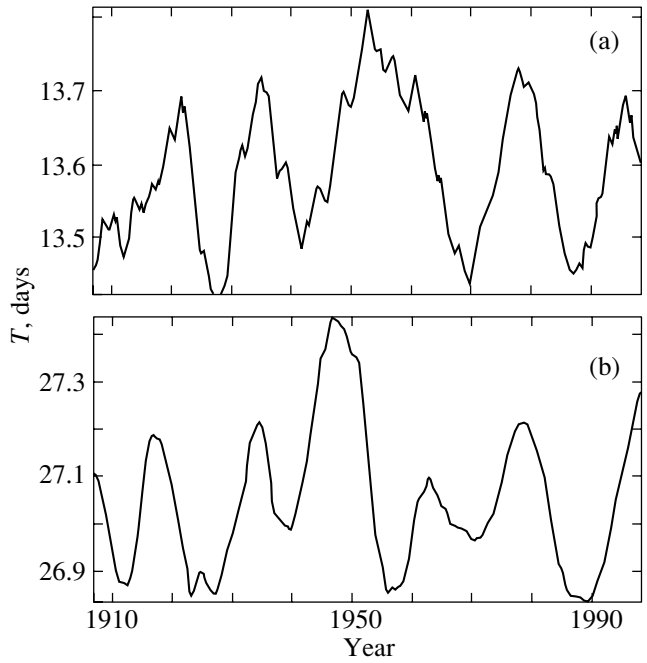


**Fig. 3.** Activity cycles in the rotation of the (a) four- and (b) two-sector structures of the solar magnetic field at latitudes within ±20° of the equator from 1904 until 2000.

Makarov *et al.* 1997, 1998; Kitchaninov *et al.* 1999). The discovery of a 22-year period in the rotation of the four-sector structure indicates a close relationship between the solar rotation rate and activity.

The variations in the rotation of the two-sector structure, ~1%, are not so significant as those for the four-sector structure (Fig. 3b). However, its rotation also exhibits a 22-year cyclicity. Periods of fast rotation of the two-sector structure (~26.9 days) were observed mainly at the maxima of even 11-year cycles. The slowest rotation (with a period of ~27.4 days) was also recorded in cycle 18 from 1945 until 1952 during the period of maximum activity. In recent years, as we see from Fig. 3, the fastest rotation of the sector structure of the solar magnetic field (26.85 and 14.45 days) was observed at the maximum of cycle 22 (about 1990). At minimum activity before the current cycle 23, the rotation periods of the two- and four-sector structures increased, being ~27.3 and 13.7 days, respectively. As we see from Fig. 3, a ~55-year period can be identified in the rotation of the two- and four-sector structures. This effect was previously detected in torsional oscillations of the Sun

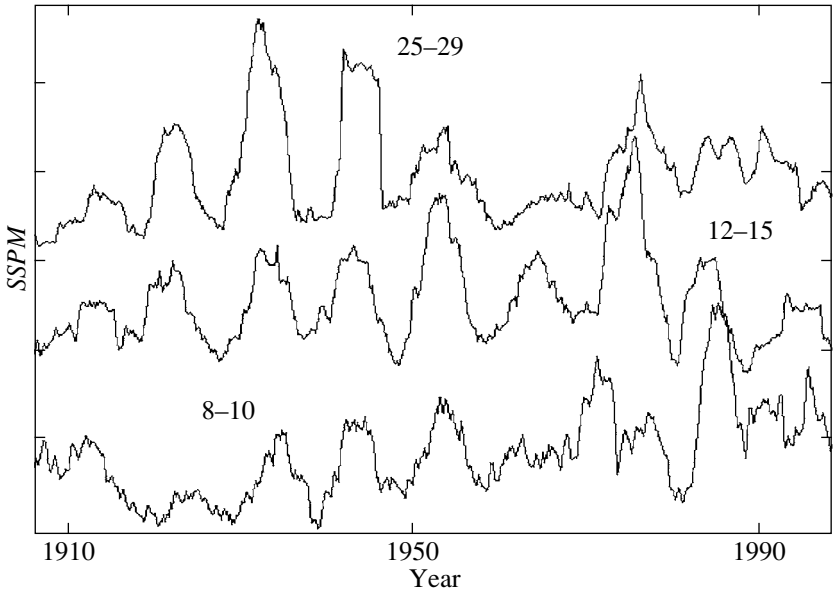


**Fig. 4.** Variation in $SSPM(t)$ or in the sum of the spectral power densities for the rotation of the two- (25–27 days), four- (12–15 days), and six-sector (8–10 days) structures of the solar magnetic field at latitudes within $\pm 20^\circ$ of the equator from 1904 until 2000.

(Makarov and Tlatov 1997; Makarov *et al.* 1997, 1998; Kitchatinov *et al.* 1999).

It should be noted that the rotation periods of the two- and four-sector structures of the solar magnetic field (Fig. 3) vary almost synchronously with the 22-year cycle of magnetic activity. This means that the two- and four-sector structures are actively involved in the generation of the solar magnetic field. Thus, the discovery of a 22-year magnetic cycle in the rotation of the sector structure and its relationship to the activity allows the problem of solar–stellar cyclicity to be addressed afresh.

### *The Spectral Power of the Rotation of the Solar Magnetic Field in the Period Ranges 25–29, 12–15, and 8–10 Days.*

Using a procedure of searching for the fundamental periods, we calculated the variations in the spectral power density of the sector-structure rotation ($SSPM$) in the ranges 25–29, 12–15, and 8–10 days (Fig. 4). The range 27–28 days is known to characterize the solar rotation at midlatitudes. As we see from Fig. 4, the sector structure of the rotation is also associated with the 11-year activity cycles; the sector rotation shows up more clearly at minimum solar activity (Makarov and Makarova 1996; Makarov and Tlatov 1997; Makarov *et al.* 1997; Obridko and Shelting 2000). A similar pattern is also observed in the range 12–15 days, which characterizes the rotation of the four-sector structure. The temporal variations in solar rotation in this range are similar to its variations in the range 25–29 days. Clearly, this is attributable to the variations in the spectral power density of the rotation within the 22-year magnetic cycle. The rotation variations in the range 8–10 days generally follow the behavior of the spectral density in the ranges 25–29 and 12–15 days, although they are less distinct.

### *Rotation Cycles of the Sector Structure of the Solar Magnetic Field and Its Activity*

As was noted above, the distribution of the solar magnetic field on H$\alpha$-maps from 1904 until 2000 was analyzed by using a fast Fourier transform. We introduced a new index of solar rotation, $SSPM(t)$, which is determined by the sum of the spectral power densities of the sector structures. The solar rotation index $SSPM = \sum(a^*a + b^*b)$ is the total power of all peaks or their envelopes in the spectrum for the chosen range of periods. The parameter $SSPM(t)$ apparently reflects the presence or absence of various types of magnetic-field sector structure. Figure 5 shows cyclic variations in this parameter. To compare $SSPM(t)$ with the solar-activity index, we give the curve of Wolf numbers $W(t)$ from 1904 until 2000. The 11-year activity cycles of the sector structure of the magnetic field $SSPM(t)$ are seen to be shifted by 5.5 years and lead the 11-year cycles of solar activity (Wolf numbers) both in amplitude and in phase. A similar relationship between the maximum Wolf number and the rotation rate of the two-sector structure of the interplanetary magnetic

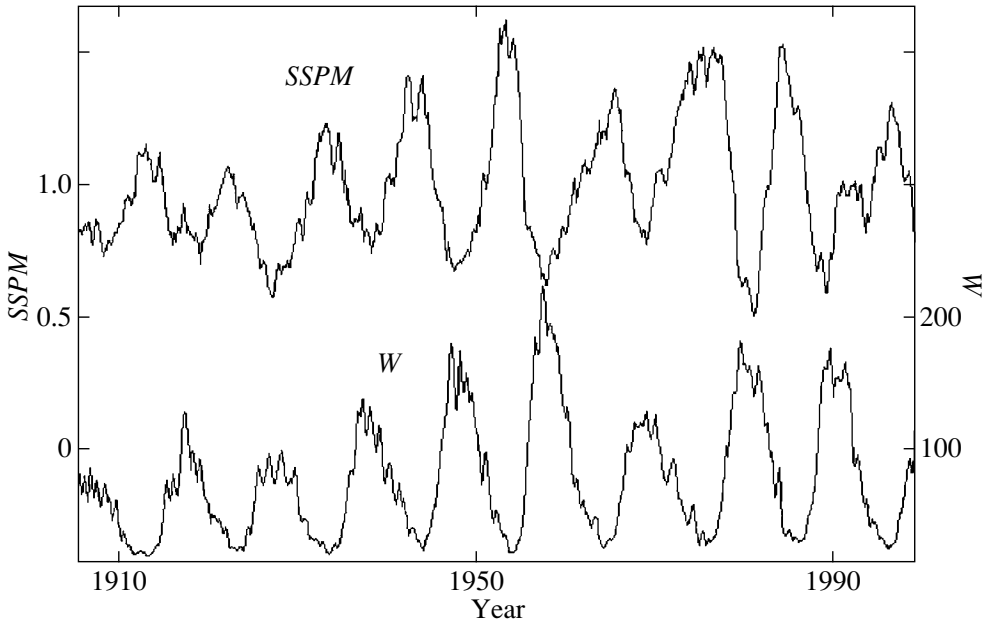


**Fig. 5.** Cyclic variations in the solar rotation index $SSPM(t)$ or in the sum of the spectral power density of the sector-structure rotation and the solar-activity index expressed in terms of the Wolf numbers $W(t)$.

field was previously derived by Makarov *et al.* (1990). Consequently, the sector structure of the solar magnetic field is actively involved in the magnetic-field generation and, thus, it is one of the main types of motion.

It should be noted that the new index of solar rotation $SSPM(t)$ is the third index of solar magnetic activity that was obtained from magnetic H$\alpha$-maps. Previously, we introduced two new indices [$A^*(t)$ and $L(t)$)] of solar magnetic activity (Makarov and Tlatov 1999, 2001; Makarov *et al.* 2001). The index $A^*(t)$ was defined as the sum of the intensities of the dipole and octupole magnetic-field components. The index $L(t)$ reflected the variations in the total length of neutral magnetic lines on the entire Sun (Makarov and Tlatov 1999, 2001; Makarov *et al.* 2001). The 11-cycles of $A^*(t)$ and $L(t)$ were shown to be also shifted by 5.5 years and to lead the 11-year cycles of Wolf numbers (Makarov and Sivaraman 1989; Makarov *et al.* 2001). Whereas the activity indices $A^*(t)$ and $L(t)$ describe the topology of the global solar magnetic field in the corona, the new solar-rotation index $SSPM(t)$ reflects some type of motions inside the Sun and, thus, differs fundamentally from the indices $A^*(t)$ and $L(t)$. However, since the cycle of $SSPM(t)$ also leads the cycle of Wolf numbers by 5.5 years, it is probably of the same nature as $A^*(t)$ and $L(t)$.

## ACKNOWLEDGMENTS

We are grateful to V.N. Obridko for the useful remarks made during a discussion of the results. This work was supported by the Russian Foundation for Basic Research (project nos. 99-02-16200 and 00-02-16355), NRA-98-OSS-08, and the Program "Astronomy" (project no. 1.5.4.2).

## REFERENCES

1. H. Balthasar and H. Wöhl, Astron. Astrophys. **92**, 111 (1980).
2. U. Becker, Z. Astrophys. **34**, 229 (1954).
3. W. Camper, Ann. Österr. Akad. Wiss. Naturwiss. KL. **94**, 188 (1957).
4. D. H. Clark, B. D. Yallop, S. Richard, *et al.*, Nature **280**, 299 (1979).
5. T. L. Duvall, J. M. Wilcox, L. Svalgaard, *et al.*, Solar Phys. **55**, 63 (1977).
6. A. Hanslmeier and G. Lüstig, Astron. Astrophys. **154**, 227 (1986).
7. R. Howard and B. J. LaBonte, Astrophys. J. Lett. **239**, L33 (1980).
8. L. L. Kitchatinov, V. V. Pipin, V. I. Makarov, and A. G. Tlatov, Sol. Phys. **189**, 227 (1999).
9. V. I. Makarov, Soln. Dannye **10**, 93 (1983).
10. V. I. Makarov, Soln. Dannye **6**, 59 (1984).
11. V. I. Makarov and V. V. Makarova, Sol. Phys. **163**, 267 (1996).
12. V. I. Makarov and K. R. Sivaraman, Sol. Phys. **85**, 227 (1983).
13. V. I. Makarov and K. R. Sivaraman, Kodaikanal Obs. Bull. **7**, 2 (1986).

14. V. I. Makarov and K. R. Sivaraman, Sol. Phys. **119**, 35 (1989).
15. V. I. Makarov and A. G. Tlatov, Astron. Zh. **74**, 474 (1997).
16. V. I. Makarov and A. G. Tlatov, in *Proceedings of the 9th European Meeting on Solar Physics, Florence, 1999,* Ed. by A. Wilson, ESA SP-448, p. 125.
17. V. I. Makarov and A. G. Tlatov, in *Proceedings of the SOHO 10/GONG 2000 Workshop "Helio- and Asteroseismology at the Dawn of the Millennium," Tenerife, Spain, 2001,* ESA-464, p. 111.
18. V. I. Makarov, K. S. Tavastsherna, and N. S. Petrova, in *Proceedings of the Workshop "Solar Terrestrial Prediction," 1990,* Ed. by R. J. Thompson *et al.* (National Oceanic and Atmospheric Administration, Boulder, 1990), Vol. 1, p. 518.
19. V. I. Makarov, A. G. Tlatov, and D. K. Callebaut, Sol. Phys. **170**, 373 (1997).
20. V. I. Makarov, A. G. Tlatov, and D. K. Callebaut, Astron. Soc. Pac. Conf. Ser. **140**, 65 (1998).
21. V. I. Makarov, A. G. Tlatov, D. K. Callebaut, *et al.*, Sol. Phys. **198**, 409 (2001).
22. H. W. Newton and M. L. Nunn, Mon. Not. R. Astron. Soc. **111**, 413 (1951).
23. V. N. Obridko and B. D. Shelting, Sol. Phys. **184**, 187 (1999).
24. V. N. Obridko and B. D. Shel'ting, Astron. Zh. **77**, 303 (2000) [Astron. Rep. **44**, 262 (2000)].
25. E. H. Schröter and H. Wöll, Publ. Obs. Astron. Catania **162**, 35 (1978).
26. Yu. I. Vitinskiĭ and R. N. Ikhsanov, Soln. Dannye **6**, 99 (1972).
27. Y.-M. Wang and N. R. Sheeley, Jr., J. Geophys. Res. **99**, 6597 (1994).
28. J. M. Wilcox and L. Svalgaard, Sol. Phys. **34**, 461 (1974).

*Translated by A. Dambis*